ICE WEDGE ACTIVITY IN THE EUREKA SOUND LOWLANDS, CANADIAN HIGH ARCTIC

Kethra Campbell-Heaton

CryoLab for Arctic, Antarctic and Planetary Studies (CLAAPS)

A thesis submitted to the University of Ottawa
in partial fulfillment of the requirements for the
Master of Science in Geography

Department of Geography, Environment and Geomatics
Faculty of Arts
University of Ottawa

Abstract

Polygonal terrain underlain by ice wedges (IWs) are a widespread feature in continuous permafrost and make up 20-35%$_{vol}$ of the ground ice in the upper few meters of permafrost. Despite the numerous contemporary studies examining factors that control ice wedge cracking, development and degradation, relatively few have explored ice wedge activity in relation with past climate and vegetation conditions. In the Eureka Sound region, ice wedge polygons dominate the permafrost terrain. Their degradation has started to occur, leading to growth of thaw slumps. The objective of this study is twofold, the principal objective is to investigate the timing of ice wedge activity in the Eureka Sound region using the $^{14}C_{DOC}$ dates. The second objective is to evaluate the use of ice wedges as paleotemperature proxies. In July 2018, four ice wedges were sampled at 3-4 depths with each core sample being ~1m in length. In the following summer, eight ice wedges were sampled from the surface, 3-5 core samples were extracted per wedge. Active layer and snow samples were also recovered. Laboratory analyses on the ice wedge samples includes dissolved organic carbon content (DOC) and $\delta^{13}C_{DOC}$, radiocarbon dating of DOC, geochemical concentration, and stable water isotopes. The DOC and geochemical results show that snowmelt is the main moisture source for ice wedges in the Eureka Sound region with a minor contribution of leached surface organics. The age ($^{14}C_{DOC}$) and size of the studied ice wedges were compared against a cracking occurrence model developed by Mackay (1974), these ice wedges align well with this model and suggest that ice wedge growth is non-linear. Ice wedges in the Eureka Sound region were active during the early to late Holocene (9-2.5 ka). The majority of the activity occurred in the later stage of the early Holocene following regional deglaciation and marine regression. $^{14}C_{DOC}$, high resolution $\delta^{18}O$ and D-excess suggests the occurrence of peripheral cracking in both large and small ice wedges. Rayleigh-type isotopic fractionation was found to occur with depth. As well, post depositional isotopic modification of snow and snowmelt accounts for up to a 4‰ difference of $\delta^{18}O$ in surface ice wedge samples. $\delta^{13}C_{DOC}$ of surface ice wedge samples suggest a habitat transition during the late Holocene from dry meadows to polygonal terrain and the geochemical composition of ice wedges closely reflects that of glacial ice core records.

Acknowledgements

First and foremost, I would like to thank my supervisor, Dr. Denis Lacelle. Without his support and guidance, this project would not have come to fruition. Denis, thank you for this opportunity, you are an awesome human-being and great mentor.

Thank you to Dr. Konrad Gajewski and Dr. André Viau for your support and constructive criticism on this thesis. Konrad, thank you for supporting my interest in permafrost even though it may all disappear by the time I am 50. And André, thank you for encouraging me to look beyond permafrost and to consider the bigger picture.

Thank you to Jean Bjornson for his support and friendship. Thank you for the long chats and the lab safety training. I would also like it to have it known that I did not break the LOI machine that one time everyone thought I did. Thank you to Chantale and Nathalie, your smiles (and endless help) made paperwork easier to endure. Thank you to the staff at the Geochemistry/ICP Laboratory, Ján Veizer Stable Isotope Laboratory and A.E. Lalonde AMS Laboratory for their patience and expertise with the different analyses.

I want to recognize Fanny Amyot, Benoit Faucher, Cameron Roy and Dr. Wayne Pollard for their help in the field. Fanny, my fieldwork buddy, thank you for all the laughs and silliness in the field. To Ben and Cam, thank you for drilling into the permafrost and getting covered in mud with me. I would not have been able to sample those ice wedges without you two. And Wayne, thank you for organizing and preparing our stay in Eureka. Thank you for the wonderful meals and all the stories. I can't thank you enough.

I would also like to thank my peers of the Geography, Environment and Geomatics Department. Graduate studies can be frustrating and sometimes you feel like you are a sinking ship, but with these people I always had a life raft. Thank you, Jean, Ben, Yifeng, Roxanne, Braden, Paige, Zuzia and others for your comradery.

Thank you to my parents, Mark and Abby, for their unwavering support even when it meant spending another two years away. I want to thank my best friend Mariah for spending countless hours editing my grammar, you rock! And, a huge thank you to my partner Jacob, for being there for me from the very beginning and encouraging me to be the best I can be.

Finally, I want to thank the Northern Scientific Training Program (NSTP), the Polar Continental Shelf Program (PCSP) and the Natural Science and Engineering Research Council (NSERC; awarded to Dr. Lacelle) for their monetary and logistical support. Without your aid, this project would not have been as successful as it was. Many thanks to you.

Table of Contents

List of Figures

List of Tables

List of Abbreviations

a.s.l.	Above Sea Level
BP	Before Present
BT	Blacktop Slump
CAA	Canadian Arctic Archipelago
CRREL	Cold Regions Research and Engineering Laboratory
d	D-excess (‰)
DOC	Dissolved Organic Carbon
DS	Dump Slump
EU	Eureka
ESL	Eureka Sound Lowlands
FP	Fosheim Peninsula
GMWL	Global Meteoric Water Line
GIS	Greenland Ice Sheet
IW(s)	Ice Wedge(s)
IIS	Innuitian Ice Sheet
LGM	Last Glacial Maximum
LIS	Laurentide Ice Sheet
LMWL	Local Meteoric Water Line
MV	Mackenzie Valley
MAAT	Mean Annual Air Temperature
MF	Mokka Fjord Slump
Nu	Nunavut Slump
POC	Particulate Organic Carbon
‰	Parts per million
ka	Thousand years
YD	Younger Dryas

Chapter 1: Introduction

Ice wedges (IWs) and associated tundra polygonal terrain are a ubiquitous feature of permafrost terrain (Mackay, 1984, 1990; Veillette et al., 2015). Tundra polygons are found across the continuous permafrost zone with ice wedges occupying 20-35%$_{vol}$ of ground ice in the upper five meters (Hugh M. French, 2018). The density, size and overall activity of an ice wedge varies as a function of climate, vegetation, soil conditions and polygon morphometry (Mackay, 1974; Mackay, 1992; Mackay, 1993; Fortier & Allard, 2005; Abolt et al., 2018). Early research on ice wedges focused on their growth and the mechanics of cracking in relation to winter conditions (Leffingwell, 1915; Lachenbruch, 1962). Ice wedges will tend to grow when winter ground surface temperatures are <-12°C and when the tensile strength is exceeded following rapid cooling of the ground (Fortier & Allard, 2005; Mackay, 1993). The thermal expansion coefficient of ice is greater than for icy soils, therefore ice will crack first when tension exceeds ~0.4-6 MPa (~1.5-2MPa for icy soils; Williams & Smith, 1989). Most ice wedges crack between mid-January to late-March near the centre of the wedge with cracks typically being in the 2-4 cm range (Mackay, 1974). The frequency of ice wedge cracking is variable and can range from annual to decadal depending primarily on winter air and ground temperatures, the latter being dependent on snow depth, vegetation cover and polygon morphology (Mackay, 1974; Liljedahl et al., 2016). Mackay (1974) observed that narrow (<1m) and large (>2m) ice wedges have lower cracking probabilities due to competing cracking and a reduction of thermal stress caused by the insolating effect of a greater snow cover in wider trough, respectively. Mackay (1974) also observed that the probability of cracking follows a normal distribution and suggested that the probability can be estimated from the average and standard deviation of the width of the ice wedges (or troughs). Once a crack is formed, it can be infilled by a variety of moisture sources, the most common moisture source is snowmelt, but vapour condensation (hoar frost) and snow have been observed as well (French & Guglielmin, 2000; Lauriol et al., 1995; St-Jean et al., 2011; Tormirdiaro, 1996). However, snow meltwater infilling the top of the crack sometimes immediately freezes and produces an ice plug that restricts further infiltration. In such cases, the lower portion of the crack may remain empty, but the crack will still close due to thermal expansion of the ice in the summer. Moreover, the annual growth increment of an ice wedge can vary from <1 mm to a few mm, much smaller than the width of a winter crack (Mackay, 1974; Lewkowicz, 1994).

Recent research has focused on ice wedge degradation in relation to climate change (Fortier et al., 2007; Zhang et al., 2008; Hobbie et al., 2017; MacDonald et al., 2018). Degradation of tundra polygons occurs primarily by thermal erosion of the ice wedge network. This leads to the development of open gullies whereby the rapid drainage of surface runoff flowing into open cracks enhances the melting of ice wedges and causes the collapse of the ground surface (Fortier et al., 2007). This degradation impacts the local hydrology and increases the amount of organic carbon in the soil available for microbial decomposition (Koch et al., 2018; Nitzbon et al., 2019). As a result, efforts have been made to map the regional distribution of tundra polygon networks and ice wedge volume allows to assess the vulnerability of permafrost landscapes to thaw-induced disturbances and related ecological effects (i.e., Bernard-Grand'Maison & Pollard, 2018; Zhang et al., 2018; Steedman et al., 2017). For example, in Western Canada, the

Mackenzie Valley air photo project (NWT Centre for Geomatics, 2008) has enabled mapping of the distribution of tundra polygons in the Tuktoyaktuk Coastlands (NWT, Canada) which were found to occupy 12.5% of landscape (Steedman et al., 2017).

With recent advances in radiocarbon dating of dissolved organic carbon ($^{14}C_{DOC}$), studies are starting to establish the timing of ice wedge growth over the late Quaternary (i.e., Grinter et al., 2019). These $^{14}C_{DOC}$ chronology provide insights into periods when winter conditions were favorable to ice wedge growth. Grinter et al. (2019) obtained a $^{14}C_{DOC}$ record of ice wedge activity on the Blackstone Plateau in central Yukon. The results indicate that ice wedges truncated c. 3 m below surface were developing between 32-27 and 22-12 cal kyr BP, a period when temperatures were cold and with sufficient snow to allow their growth. A new group of ice wedges initiated in the overlying colluvial deposits around 6300 cal yr BP, with a peak between 3990 and 870 cal yr BP, a period during which climate was cool and moist (Grinter et al., 2019). Given the absence of $^{14}C_{DOC}$ ages during the early Holocene, it was suggested that this period was too warm to sustain ice wedge growth. Ice wedges $\delta^{18}O$ are also inferred to reflect winter air temperatures based on the empirical relationship that exists between local temperature and $\delta^{18}O$ data from modern ice wedges or modern precipitation (i.e., Vasil'chuk, 1992). Porter and Opel (2020) summarized $\delta^{18}O$ measurements of ice wedges from Northern Russia, Svalbard, Alaska and the Yukon. Ice wedges dated between 57-11.7 cal kyr BP were depleted in $\delta^{18}O$ compared to Holocene-age ice wedges, suggesting colder winter temperatures during the late Pleistocene. In addition, modern ice wedges showed an increase in winter temperatures in comparison to Holocene-dated ice wedges (Porter & Opel, 2020). However, these studies lack proper chronology as it is based on ^{14}C dating of particulate organic carbon (POC) from above the wedge or enclosed in the wedge ice itself, which is an unreliable method to accurately date ice wedges (Lachniet et al. (2012).

In high Arctic Canada, tundra polygons occupy c. 50% of the Fosheim Peninsula on Ellesmere Island (NU, Canada) with 3.8% of the top 5.9 m of permafrost hosting ice wedges (Couture & Pollard, 1998; Bernard-Grand'Maison & Pollard, 2018). The goal of this thesis is to investigate the timing of ice wedge activity in the Eureka Sound Lowlands (ESL) region on Fosheim Peninsula and their isotope geochemistry in relation to permafrost aggradation and changing Holocene climate and vegetation conditions. The ESL was deglaciated around 9000 years ago (J England et al., 2006) and field sites were selected along an elevation gradient from the Holocene marine limit (~143 m a.s.l.) to modern sea level (Slidre Fiord). The thesis provides the first reconstruction of Holocene ice wedge activity in the Canadian high Arctic and considering winter air temperature remained favorable to ice wedge growth throughout the Holocene, the ice wedge activity likely reflects changes in regional snow conditions.

1.1 Research Objectives:

The principal objective of this study is to investigate the timing of ice wedge activity in the Eureka Sound Lowlands (ESL) based on the $^{14}C_{DOC}$ measurements within the wedge in order to understand regional climate for the Holocene. The second objective is to determine if ice wedges can be used as winter paleotemperature proxies by analyzing the $\delta^{18}O$ from horizontal cores at different depths within individual ice wedges.

The primary objective will be accomplished by:

1. Comparing the DOC, $\delta^{13}C_{DOC}$ and geochemical measurements in ice wedges to those in snowpack and active layer in order to determine the ice wedge's moisture source.
2. Testing the validity of $^{14}C_{DOC}$ in ice wedges in the ESL by comparing the measurements to the Mackay (1974) model of ice wedge cracking probability and estimated age of ice wedges.
3. Reconstructing the Holocene ice wedge activity in the ESL through $^{14}C_{DOC}$ measurements.
4. Understanding the influence of regional climate on ice wedges by comparing the timing of ice wedge activity between the ESL and western Arctic (data from Grinter et al., 2019; Holland et al., 2020).

The secondary objective will be accomplished by:

1. Determining effect of sampling depth within ice wedges on their $\delta^{18}O$ composition.
2. Comparing $\delta^{18}O$ of ice wedges with the nearby Agassiz ice core record (data from Lecavalier et al., 2017).
3. Assessing past vegetation change and ionic load in the ESL using $\delta^{13}C_{DOC}$, ion concentrations and $^{14}C_{DOC}$ ages from sampled ice wedges.

Chapter 2: Literature Review

The purpose of this section is to provide a background on relevant topics pertaining to this thesis. Topics to be covered are as follows: permafrost and its features; ice wedge formation, cracking, dating and use as paleoclimate proxies.

2.1. Permafrost

Permafrost is defined as ground (soil, bedrock) that remains below 0°C for more than two consecutive years (French, 2007). Permafrost covers 24% of Earth's terrestrial land mass and nearly 50% of Canada's landmass is underlain by permafrost (Stott & Huddart, 2010). The distribution of permafrost has been divided into four classifications based on coverage: (1) continuous (90-100%); (2) discontinuous (50-90%); (3) sporadic (10-50%) and, (4) isolated (0-10%). The boundaries of these permafrost zones largely reflect mean annual air temperature (MAAT) isotherms. The southern extent of continuous permafrost coincides with the -6 to -8°C isotherm (Smith & Riseborough, 2002). Discontinuous permafrost extends as far as the -1°C isotherm, and permafrost that exists south of the -1°C isotherm typically is restricted to peatlands, north-facing slopes and shady riverbanks (French, 2007). However, isotherms are not the only factor controlling permafrost formation. At a local scale, the type of soil can impact permafrost formation based on its conductivity. The amount of snow in the winter can insulate an area and prevent the formation of permafrost (French, 2018). Vegetation also has the ability to inhibit or promote the formation and subsequent presence of permafrost; and even the local topography and drainage can affect permafrost distribution. At depth, an active layer exists above permafrost. This layer of soil, bedrock or organic matter seasonally freezes and thaws (French, 2018). Fig. 2.1 illustrates the active layer-permafrost model where the active layer is the top-most layer that interacts with the atmosphere. The transient layer, which thaws on a decadal scale depending on the summer climate conditions, borders the active layer and permafrost (Shur et al., 2005). Of course, it is important to note that the depth of the active layer and transient layer is not consistent throughout the world but will vary due to the aforementioned factors that influence permafrost distribution.

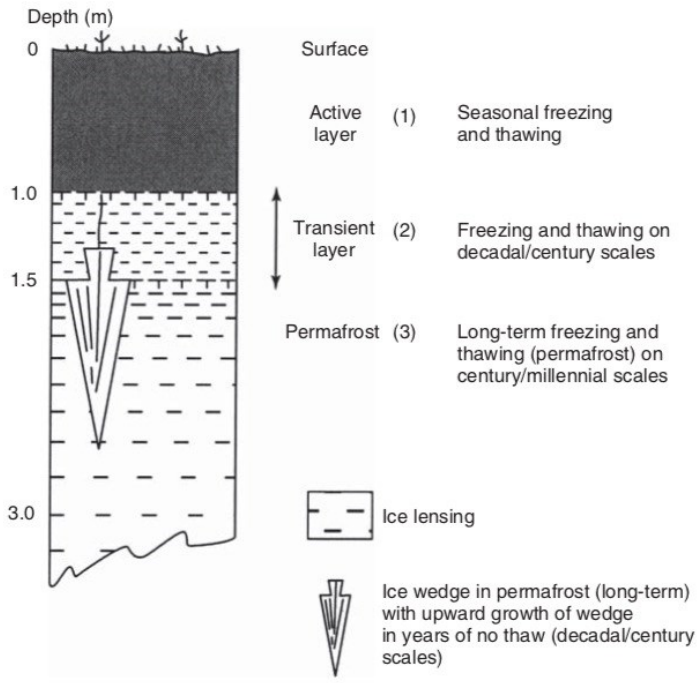

Figure 2.1. Diagram of the three-layer active layer-permafrost interaction model. Adapted from French, 2018.

2.1.1. Thawing Permafrost

Presently, permafrost in the circumpolar Arctic is warming at varying rates. Northern Russian and Siberian permafrost has been warming since the late 1980s, with rates varying between 0.1-0.4°C decade^{-1} depending on site conditions (ex. Montane region, presence of vegetation, and sediment characteristics; Drozdov et al., 2015). The permafrost in Nordic regions has been warming slowly for the last six to eight decades but has increased since early 2000 to a rate of 0.4-0.7°C decade^{-1} (Christiansen et al., 2010; Farbrot et al., 2013). Nordic permafrost is considered warm (above -3°C), and isolated to tundra and bog environments (Farbrot et al., 2013). In Canada, portions of the Mackenzie Valley (MV) are underlain by warm permafrost which has been warming since the 1980s (Smith et al., 2016). In the early 2000s, permafrost warming rates in the MV slowed as a result of nearing 0°C. This is because latent heat is redirected from the permafrost to the ground ice which slows the permafrost warming rate (Romanovsky et al., 2018). Permafrost at high latitudes are also subject to warming. In Alert (Ellesmere Is.), the recorded permafrost temperatures at the location of zero annual amplitude (area of no annual temperature change; 24 m) increased 1-1.4°C between 1978 and 2014 (Smith et al., 2015). The active layer is also thawing to greater depths in the summer because of warmer climate conditions. In 2016, active layer depths in Siberia and Greenland were 0.15 m deeper than previous years (Smith et al., 2015). In addition, the active layer in Nordic regions has also been increasing since the late 1990s (Christiansen et al., 2010). In Canada, the active layer above discontinuous and warm permafrost has increased in depth since the late 1990s (Smith et al., 2010; 2016). As a result, Hobbie et al. (2017) found an increase in lake alkalinity due to an increase in active layer depth. Moreover, degrading permafrost and greater active layer thaw is

impacting surface hydrology (MacDonald et al., 2018), increasing plant diversity (Liljedahl et al., 2016; Hobbie et al., 2017), and increasing CO_2-CH_4 carbon emissions (Schuur et al., 2015).

Based on six scenarios of climate change for Canada, Zhang et al., (2008) estimated that by 2090, the permafrost in will be reduced by 16.0-19.7%. Between 1990-2100, the active layer is expected to increase in thickness by 0.3-0.7m (Zhang et al., 2008). Continued permafrost degradation is expected to impact surface hydrology (M. K. MacDonald et al., 2018), increase plant diversity (Liljedahl et al., 2016; Hobbie et al., 2017), and increase CO_2-CH_4 carbon emissions (Schuur et al., 2015). Permafrost thaw is also expected to have an impact on the global mercury cycle. For example, Schuster et al. (2018) estimate that the Northern Hemisphere contains 1656 ± 962 Gg Hg of mercury, and 793 ± 461 Gg Hg is stored within the permafrost. Permafrost thaw will subsequently release the stored mercury and result in "unknown consequences to the environment" (Schuster et al., 2018). In addition, future permafrost thaw is expected to cause socioeconomic issues. Degrading permafrost in Eastern Siberia, for example, has altered indigenous land-use. Residents of Viliui Sakha communities have noticed an increase in precipitation, flooding, temperature and decrease in animal diversity (Crate et al., 2017). These residents are largely impacted by an increase in surface water which impacts their crop yield as well as access to natural resources and infrastructure damage (Crate et al., 2017). Many inhabitants have had to abandon their underground cold storage (buluus) because of the increase in meltwater from the melting ground ice within the permafrost (Crate et al., 2017). With ongoing climate change, the effects of permafrost degradation will become more severe.

2.2. Permafrost features

The purpose of this section is to provide more detail regarding specific permafrost features. It is important to note that many permafrost features are left out of this section because they are not relevant to this research topic.

2.2.1. Ground Ice

Ground ice exists in any permafrost that contains moisture, regardless of quantity. There are many different types of ground ice which varies depending on a number of factors (water availably, temperature, sediment type, etc.). Mackay (1972) established a ground ice classification based on two criteria. The first is based on the source of water immediately prior to freezing (atmospheric, surface, and ground). The second criterion is based on the principal transfer processes which move water to the freezing plane (ex. thermal; Mackay, 1972). There are four main ground ice classifications: pore, segregated, intrusive, and vein. Pore ice occupies the voids between sediment particles; this type of ice is considered ubiquitous to areas with moisture and is typically located in the near–surface permafrost and active layer (H M French, 2007). Segregated ice forms in a variety of materials but is typically housed in those that are water-saturated and fine grained. There are three types of segregated ice: ice lenses, aggregated ice and reticulated vein ice. Ice lenses are typically visible to the naked eye and can vary in thickness (from a few centimeters to several meters; Mackay, 1972). Aggregated ice is formed via upward freezing such as accumulation of organic matter or a rising permafrost table. Reticulate vein ice develops in fine-grained soils, the horizontal and vertical ice veins form in

three-dimensions. They form in shrinkage cracks and derive water from the surrounding material in a semi-closed system (Mackay, 1974; French, 2007). The third ice classification, intrusive ice, is formed by water intrusion into seasonally or perennially frozen ground. There are two types of intrusive ice: sill and pingo ice. Sill ice forms when water is intruded into a confining material (like permafrost), the water then freezes into a tabular mass and causes ground uplift (Mackay, 1972). Pingo ice is formed by the expulsion of pore-water in a closed system. Typically, they occur when a talik (body of unfrozen ground) located below a drained lake begins to refreeze (French, 2007). Finally, vein ice is formed within open thermal contraction cracks in icy permafrost soils (Mackay, 1974). There are two types of vein ice: single vein ice and ice wedges. Single vein ice develops in thermal contraction cracks typically 0.2 cm thick and less than 70 cm deep (Mackay, 1972; French, 2007). Ice wedges are considered repeated ice-veins that form in thermal contraction cracks that open at the same place every year for a number of years (Mackay, 1972; French, 2007).

2.2.2. Ice wedges

Ice wedges (IWs) are bodies of ice that frequently form within the top 5m of permafrost (Pollard & French, 1980). These bodies of ice form within thermal contraction cracks and can vary in size from a few centimeters to a few meters directly below the active layer. Ice wedges are near-ubiquitous to permafrost regions, but the most favourable condition appears to be poorly drained tundra lowlands over continuous permafrost (French, 2007). Under optimal conditions, ice wedges can continue to grow for hundreds to thousands of years (Liljedahl et al., 2016). Over a large area, ice wedges form an interconnected network of polygons (polygon terrain) that are easily recognizable from ground and aerial surveys and high-resolution satellite imagery. Mackay (1972) estimates that ice wedges underlay 2.6 million km^2 of tundra and boreal forest in North America. Ice wedges on the Fosheim Peninsula are estimated to occur on 50% of the peninsula and occupy 3.81% of the upper 5.9m of permafrost in the area (Bernard-Grand'Maison & Pollard, 2018).

2.2.2.1. Types of Ice Wedges

There are three types of ice wedges: epigenetic, syngenetic and anti-syngenetic. Epigenetic ice wedges grow in pre-existing permafrost and are usually much younger than the enclosing sediment; and the age of the enclosing sediment is consistent (Mackay, 1990). These ice wedges are typically V-shaped and grow progressively wider but not deeper. Syngenetic ice wedges develop following the accumulation of sediment on the surface which raises the permafrost table and encourages ice growth upwards. The age of the ice is typically synchronous with the host sediment. The shape of the wedge is dependent on the horizontal and vertical growth rates (Mackay, 1990; French, 2007). In opposition, anti-syngenetic ice wedges grow on receding slopes where the surficial sediment is eroded, and the permafrost table is forced downwards. If thermal contraction cracking and ice vein growth is synchronous with surface removal, the veinlets grow progressively deeper (Mackay, 1990).

2.2.2.2. Growth of Ice Wedges

Ice wedges tend to grow when winter ground temperatures are <-10°C and when the soil tensile strength is exceeded, forcing the ground to crack (Ballantyne, Williams, & Smith, 1990). Considering that the thermal expansion coefficient of ice is greater than for icy soils, the ice will crack when tension exceeds ~0.4-6 MPa (Ballantyne et al., 1990). Studies have related climate conditions under which ground cracking occurs. Mackay (1993) suggests a four-day period of intensive cooling (1.8°C day^{-1}) is associated with ice wedge (IW) cracking in the Mackenzie Delta. Fortier & Allard (2005) noted that a drop of 2°C over an 18-hour period induced cracking of ice wedges on Bylot Island. The ground will not necessarily crack when these conditions are encountered because the distribution and thickness of snow cover plays a key role in buffering the change in temperature at the ground surface.

Most ice wedges will crack between mid-January to late-March (Mackay, 1974). Once an ice wedge is established in permafrost, winter thermal contraction cracking has been found to originate from the top of the ice wedge, not the ground surface (Lachenbruch, 1962; Mackay, 1974; 1984; Mackay & Burn, 2002), which is why the crack occurs frequently in the same location as the year before. Mackay (1992) developed a classification for ice wedges based on their cracking frequency. Active ice wedges crack once every two years on average; moderately active ice wedges crack on average once every ten years; rarely active ice wedges crack at least once every fifty years; and inactive ice wedges are those that crack less than once every fifty years. The frequency of ice wedge cracking depends on a variety of factors (listed below in Table 1). Mackay (1974) reports that the width of an ice wedge directly controls the probability of cracking events. Where the width of an ice wedge and the recorded cracking events lie reasonably well along a normal distribution curve.

$$\text{Probability of cracking (P)} = \frac{1}{\sigma\sqrt{2\pi}} e^{\frac{-(x-\bar{x})^2}{2\sigma^2}} \qquad (1)$$

Where x is the width of an ice wedge (m), $\bar{x}$ is the average IW width (1.1 m for Mackay (1974)), σ is the standard deviation (0.7 m for Mackay (1974)), the curve is truncated at x=0 and becomes asymptotic to the x-axis around 3m. When an ice wedge does crack, the depth and width of the crack in the winter averages 1 cm ± 0.5 cm , however, come spring, this crack will partially close due to ice thermal expansion before becoming infilled with snow, hoarfrost or snow melt. Occasionally, infilling from the top of the crack in the active layer creates an ice-plug which prevents the rest of the crack from infilling with snowmelt (Mackay, 1974). Annual ice wedge growth varies between 1-5mm. Mackay (1974) presents a model predicting the age of a given ice wedge based on its width and an average growth increment (2 mm). Using the probability curve (Eq. 1), he uses the growth increment (ΔX) to predict the number of years (T_{ij}) required for the wedge to increase from X_i to X_j with the mean crack probability for the interval (P_{ij}).

$$\text{Years between } i \text{ and } j\ (T_{ji}) = \frac{(X_j - X_i)}{\Delta X P_{ij}} \qquad (2)$$

With T_{ij}, the age of the ice wedge (A_j), the width (X_j) is given by:

$$\text{Age of ice wedge } (A_j) = \Sigma T_{ji} \text{ for the period of 1 to j} \qquad (3)$$

Given this model, one can predict the age of an ice wedge given the growth increment and width of the ice wedge (Mackay, 1974).

Once a crack is formed, it can be infilled by a variety of moisture sources. The most common moisture source is snowmelt, but vapour condensation and snow have been observed as well (Lauriol et al., 1995; St-Jean et al., 2011; Tormirdiaro, 1996; French & Guglielmin, 2000). St-Jean et al (2011) use ice crystallography, bubble distribution, stable isotope and occluded gas analyses to determine the moisture source for ice wedges in Alaska and the Yukon. They suggest that the climate and site-specific environmental conditions effect the moisture source. Dry and cold climates favour hoarfrost and snow infiltration, cool and wet environments favour snow melt infiltration (St-Jean et al., 2011).

Table 2.1. Environmental and climate factors which directly and indirectly influence ice wedge cracking.

Cracking Controls	Effect to Ice Wedge	Influence (-/+)	Study
Air Temperature	2-4 day cooling (or warming) period linked to IW cracking.[1]	+	Fortier & Allard, (2005); Mackay, (1993)
Ground Temperature	Specific ground temperature conditions required for cracking occurrence; conditions vary by region.	+	Lachenbruch (1962); Allard & Kasper, (1998); Mackay, (1975, 1993); Fortier & Allard, (2005); Matsuoka et al., (2018)
Snow Depth	Insulating effect, prevents cracking.	-	Goodrich (1982); Mackay (1993); Sarrazin & Allard, (2011)
Wind direction	E, SE and S winds of varying strength encourage cracking*.	+	Fortier & Allard (2005)
Surface water	Acts to cool the IW in warm winters. *	+	Mackay (1992); Matsuoka et al. (2018)
Vegetation	Presence acts to inhibit growth, sudden absence (ex. deforestation) linked to IW inception. [2]	-/+	Mackay (1993); Payette et al. (1986)
Polygon Geomorphology	Well defined polygon rims cool the IW and induce cracking.	+	Mackay (1992); Abolt et al., (2018)
Size	Very small (>50 cm) and very large (<2m) IW are less likely to crack than IW of intermediate width.	-/+	Mackay (1974; 1992; 1993)

*Not well known, area of future study.

[1] Recent studies illustrate a weak relationship between this control and IW cracking.

[2] Indirect influence on IW cracking.

2.2.2.3. Ice Wedge Degradation

The Arctic is warming twice as fast as areas at lower latitudes (termed Arctic Amplification; Screen & Francis, 2016). With this warming, the stability of ice-rich permafrost in highly populated regions is becoming of increasing concern (Hjort et al., 2018). Ice wedges make up approximately 20-35% of ground ice in the upper 5-10 meters of permafrost (French, 2007). Liljedhal et al. (2016) describe the first sign of ice wedge polygon degradation as a shift in plant species occupying the ice wedge troughs (from lichen and moss to sedges and grasses). As the ice wedges continue to degrade, ponding water develops within the ice wedge troughs, which will in turn speed up the degradation process. As the wedge thaws, the surface layer above it subsidizes and the trough deepens, in most cases this allows the ponding water to drain. Liljedahl et al. (2016) suggest that the timeline for this process varies from several decades to as few as 8 years. On Bylot Island, ~900 km away from Eureka, Fortier et al. (2007) identified underground thermal erosion tunnels that follow ice wedge polygon networks. These tunnels are a result of thermal and mechanical weathering of thermal contraction cracks from spring meltwater and often erodes into the ice wedge below (Fortier et al., 2007). Effected wedge ice was found to melt at a rate of 1-5m/day in 1°C water with consistently high discharge rates (0.15-0.45m3/s; Fortier et al., 2007). Similarly, Pollard et al. (2015) found that ice wedges in the Eureka Sound Lowlands are subject to degradation, where they observed a 4 cm subsidence of the active layer with a 5 cm loss of the top of the ice wedge. Ice wedge degradation is currently a popular topic in the literature; studies predominantly focus on the biological and hydrological implications of ice wedge thaw (ex. Koch et al., 2018; Nitzbon et al., 2019).

2.2.2.4. Growth and Activity of Ice Wedges

Multiple methods have been used to obtain information on the timing of the development of ice wedges. Indirect dating methods rely on the ages from the surrounding or overlying sediments to inform on the formation of ice wedges in an area (Opel et al., 2018). Radiocarbon, thermos-luminescence, and fission-track dating of tephra have all been used to date the host sediment and infer the age of the ice wedge (Opel et al., 2018). However, this technique is only reliable when dating syngenetic ice wedges as they form with the accumulation of new sediment (Blinov et al., 2009). This method will only provide a rough age estimate and so, it is not useful to provide a chronological control of ice wedge growth, despite its use in high-resolution paleoclimate reconstructions (Opel et al., 2018).

A variety of direct dating techniques also exist, including tritium. Technique selection depends on the estimated age of the ice wedge. Tritium (^{3}H) has a very short half-life (12.43 years) and decays by beta release (Clark & Fritz, 1997b). Therefore, tritium analysis can be used to date active or moderately active ice wedges. For example, Lewkowicz (1994) used tritium in multi-stage ice wedges to provide evidence of the recent growth of secondary and tertiary ice wedges on the Fosheim Peninsula. Similarly, Dereviagin et al., (2000) use tritium to date and track the growth of modern ice wedges in the Laptev Sea region. Ice wedges with low tritium concentrations (<15 TU) were found to be inactive since the 1950s. Additionally, Kokelj et al. (2007) used tritium dating to confirm the inactivity of ice wedges beneath spruce forests.

Radiocarbon analyses are used to obtain ages from ice wedges younger than 40,000 years. Radiocarbon dating focuses on measuring the loss of the parent radionuclide; ^{14}C has a half-life of 5730 years (Clark & Fritz, 1997a). Particulate organic carbon (POC) trapped within the ice wedge has been used to determine the formation of the ice wedge (ex. Vasil'chuk et al., 2000, 2004, 2006; Vasil'chuk & Vasil'chuk, 2017). The POC is picked up by snowmelt runoff and deposited in the open ice wedge crack. However, POC can be stored for thousands of years in the active layer and can potentially provide older ages than the age of deposition. Based on a comparison of ^{14}C ages from POC, trapped CO_2 bubbles and DOC, Lachniet et al. (2012) found that POC and dissolved organic carbon (DOC) yielded a difference in ages up to 11,170 years and suggested that DOC trapped within the ice yielded the most reliable ages to determine ice wedge growth.

Grinter et al. (2019) used $^{14}C_{DOC}$ ages taken from the centre and edges of ice wedges in the central Yukon. Based on the results, they found that ice wedges were actively forming mainly during cool and moist climate intervals. The $^{14}C_{DOC}$ measurements also suggest that cracking and infilling by snow meltwater does not consistently occur near the center of the wedge. In the wider wedges, Grinter et al. (2019) found asymmetrical dates on either side of a specific wedge (31,500 yr cal BP on left side, 13,685 yr cal BP on right side). Additionally, one ice wedge was older in the centre (6360 yr cal BP) than it was on the right side (2450 yr cal BP).

Finally, for ice wedges that formed in the mid to late Pleistocene, ^{36}Cl and U/Th have been used to date ice wedges in Siberia (Blinov et al., 2009). ^{36}Cl has a half-life of 301,000 years; decay of the isotope occurs via beta emission or electron transfer (Clark & Fritz, 1997a). In addition, uranium isotopes have also been used to date ice wedges and other ground ice with high uncertainty with the estimated ages (~100 ka; Ewing et al., 2015). The decay of uranium isotopes tracks the parent-daughter nucleotide activity, and the half-life of the daughter isotopes vary but this process can be used to date water hundreds to thousands years old (Clark & Fritz, 1997a).

2.2.2.5. δD-$\delta^{18}O$ of Ice Wedges as a Winter Paleo-Temperature Proxy

Stable water isotopes in ice cores are frequently used to determine past temperature conditions of an area (Porter & Opel, 2020). This is because stable water isotope analyses rely on the fractionation of water molecules in the natural environment, and the results are presented as a ratio between oxygen-18/oxygen-16 ($\delta^{18}O$) and deuterium/hydrogen (δD; Dansgaard, 1964; Meyer et al., 2002; Opel et al., 2011).

The majority of ice wedge paleoclimate studies originate from Northern Russia (Opel et al., 2018; Streletskaya et al., 2011; Vasil'chuk & Vasil'chuk, 2018; Vasil'chuk et al., 2015; Vasil'chuk & Vasil'chuk, 2017). Multiple studies use stable isotope data to infer past climate conditions from modern to ~200 ka. Ice wedges are used as a winter paleoclimate proxy because they are active in the winter and are primarily infilled by winter precipitate. Porter and Opel (2020) compiled the stable water isotope data from 82 ice wedge and/or pore ice studies from all over the Arctic. Data was sorted into four time periods: modern (last several decades), Holocene (11.7 cal kyr BP onward), MIS 2 (29-11.7 cal kyr BP) and MIS 3 (57-29 cal kyr BP). Two patterns were identified throughout the four periods.

First, coastal ice wedges were found to be more enriched than continental ice wedges; this is attributed to their distance from the moisture source. Second, Russian ice wedges appear to become less enriched in $\delta^{18}O$ and δD from west to east. This is attributed to a dominance of westernly moisture transport from the North Atlantic and Rayleigh distillation along the west-east temperature gradient (Porter and Opel, 2020). Climate changes are also evident (Fig. 2.2); the coldest temperatures are recorded to occur before the Holocene (MIS 2 and MIS 3). Vasil'chuk and Vasil'chuk (2018) used ice wedges to identify a winter cooling trend between 45-15 ka on Ayon Island. The lowest temperatures occurring in 29-28 cal kyr BP and 21-18 cal kyr BP which corresponds to two global cooling periods (Vasil'chuk & Vasil'chuk, 2018). Opel et al. (2017) also identify a very cold to moderate climate between 60-30 ka and extremely cold winter temperatures during the last glacial maximum (LGM) via stable water isotope data collected from ice wedges. In addition, ice wedges have been used to identify areas of N. Russia that were not glaciated during the LGM (Streletskaya et al, 2011). Ice wedges from this area show winter warming since MIS 2 ($\delta^{18}O$ = -26‰) and becomes more enriched during the Holocene ($\delta^{18}O$ = -20.5‰) and increasingly in the modern winter ($\delta^{18}O$ = -16.5‰; Streletskaya et al., 2011). Ice wedges have been used to identify a late Holocene winter warming trend (Opel et al., 2011; Vasil'chuk et al., 2018). Vasil'chuk et al. (2015) compared ice wedge $\delta^{18}O$ data from Siberia and Svalbard, where both series showed an increasing trend from 2.5 ka onwards with a strong change occurring in Siberia. This change has been attributed to an increase in winter solar insolation and Arctic amplification caused by an increase in greenhouse gasses (Opel et al., 2017). This winter warming trend is illustrated in Fig. 2.2 between the modern and Holocene stable water isotopes (Porter & Opel, 2020). Vasil'chuk (2013) has used stable isotope values from ice wedges to identify Dansgaard-Oeschger (DO) events. However, the coarse dating and subsequent uncertainties make it difficult to pinpoint a specific event (Porter & Opel, 2020).

In North America, there are significantly fewer paleoclimate studies of ice wedges. With all the studies situated in Alaska or the Yukon and primarily reconstructing the climate history for the Pleistocene. For example, Porter et al. (2016) used stable isotopes from wedge ice to infer that the MIS 2/3 transition was ~14±5°C cooler than modern spring-winter temperatures. This was based on the δD differences between a modern ice wedge (0-500 cal BP) and a wedge dated to 30 cal kyr BP. Ice wedge samples collected near Fairbanks, Alaska show a 5.4‰ decrease in $\delta^{18}O$ around the LGM indicating a significantly colder climate (Lachniet et al., 2016). Mean annual and winter temperatures for this study was reconstructed using a linear regression equation. Currently, in Fairbanks, the MAAT and winter temperatures are -2.8°C and -21.1°C, respectively. At LGM, MAAT and winter temperatures were significantly lower at ~ -12°C and -38°C, respectively (Lachniet et al., 2016). Similarly, Late Wisconsin ice wedges (16.2 cal kyr BP) from the Yukon coast contain heavily depleted $\delta^{18}O$ (-29.1‰) and low D-excess values which indicates colder than modern winter temperatures and reduced snow depths (Fritz et al., 2012). Moreover, the Barrow Ice Wedge System demonstrates the existence of a Younger Dryas (YD) cold event in the area, and this was evident in the D-excess trends of the sampled ice wedges (Meyer et al., 2010). This interval is consistent with the Greenland NGRIP ice core record. The collected stable isotope information from these ice wedges show a gradual change of the atmospheric moisture conditions during the YD, estimated to be associated with the opening of the Bering Strait (Meyer et al., 2010). This extreme winter cooling is identified from a ~6‰ decrease in $\delta^{18}O$ for the Younger Dryas

(Lachniet et al., 2012; Meyer et al., 2010). To further understand the climate conditions for the YD, Iizuka et al. (2019) used the concentration of methanesulfonate ions (MS^-) in ice wedges (Barrow Ice Wedge System) to reconstruct sea ice fluctuation in the Beaufort Sea. The high concentrations of MS^- during the YD (12.9-12.7 cal kyr BP) indicates that the area may not have been completely filled by permeant sea ice (Iizuka et al., 2019). This study illustrates a novel application of ice wedges as paleoclimate proxies for sea ice reconstructions (Porter & Opel, 2020).

Ice Wedge Sampling Techniques for Paleoclimate Research:

A number of ice wedge sampling techniques exist for paleoclimate reconstructions. The first is ice block samples; which are large samples of ice extracted from different sections of an ice wedge with an oil-free chain saw. Samples are thawed in the field and brought back to a lab for further analysis, which will provide a dataset with a coarse resolution (ex. Grinter et al., 2018; Opel et al., 2017; Vasil'chuk et al., 2015). The second method has a higher sampling resolution, where large sections of ice are extracted from the wedge horizontally using an oil-free chain saw. These large sections are shipped frozen, brought to a cold room and subsampled into ~2-10 cm sections (ex. Opel et al., 2017; Vasil'chuk et al., 2015; Iizuka et al., 2019). Moreover, a 15mm-diameter ice screw is an effective tool to extract ice wedge samples. For example, Vasil'chuk et al. (2018) used an ice screw to sample an ice wedge horizontally and vertically at a 5-15 cm resolution. The type of ice wedge (epigenetic, syngenetic or anti-syngenetic) will determine the sampling technique and direction employed. Epigenetic ice wedges are typically sampled horizontally (Iizuka et al., 2019; Lachniet et al., 2012; Meyer et al., 2010), whereas syngenetic ice wedges are sampled in both directions (ex. Vasil'chuk et al., 2018; Vasil'chuk & Vasil'chuk, 2018; Vasil'chuk et al., 2015; Opel et al., 2017).

Limitations:

A number of limitations exist in ice wedge paleoclimate studies, with the majority occurring in regard to the mechanics behind ice wedge cracking and infilling. Ice wedges are widely assumed to crack consistently in the centre of the wedge; however, multiple studies have found irregularities in ice wedge 14C chronologies as a result of an inconsistent cracking location (Opel et al., 2017; Grinter et al., 2019; Holland et al., 2020). No such studies exist which accommodate for this phenomenon in an ice wedge temperature reconstruction. Moreover, the dating of specific ice veins is very difficult because of the average width of a vein (1-10 mm; Mackay, 1972) and the large quantity of water needed for dating analysis. Thus, even the most reliable dating technique ($^{14}C_{DOC}$; Lachniet et al., 2012) may not provide the precise date of the ice vein. Finally, an ice wedges' moisture source has been isolated to snow, hoar frost or snow melt (M. St-Jean et al., 2011). However, the evolution of snow and snowmelt before entering an ice wedge is not well studied. Meyer et al. (2008) determined that some of their studied ice wedges have a limited climatic relevance due to their low D-excess (>2‰). These values suggest that secondary fractionation is occurring and may be caused by evaporation/sublimation of the snowpack or the participation of reprecipitated water (Meyer et al., 2008).

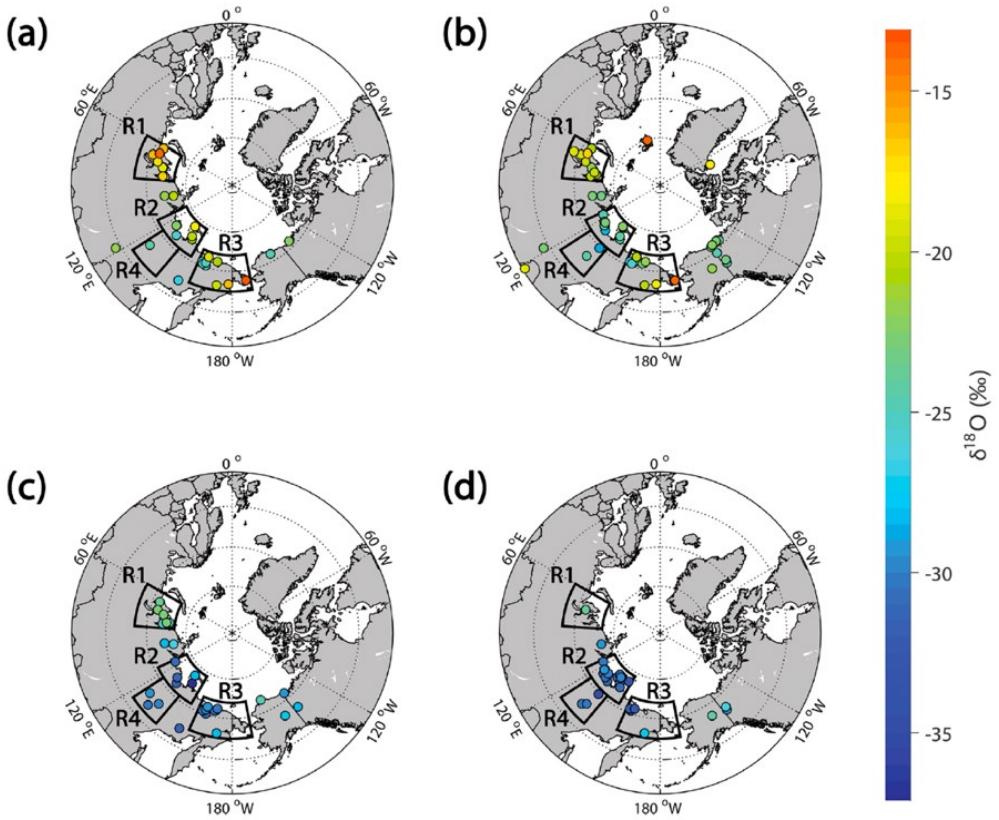

Figure 2.2. Average ice wedge $\delta^{18}O$ dating from (a) Modern; (b) Holocene; (c) MIS 2 -29-11.7 cal kyr BP and; (d) MIS 3 – 57-29 cal kyr BP. Areas outlined in black indicate: R1 – West Siberia, R2 – Laptev Sea region, R3 – Kolyma and Chukotka and, R4 – Central Yakutia (Porter and Opel, 2020).

Chapter 3: Study Area

The Eureka Sound Lowlands (ESL) is situated in the Canadian Arctic Archipelago (CAA) and covers c. 750 km^2 of Axel Heiberg and Ellesmere Islands with the Fosheim Peninsula (FP; Ellesmere Is.) comprising most of the area. The FP is surrounded by Eureka Sound, Greely Fjord, and Cañon Fjord to the west, and is separated from the rest of Ellesmere Island by the Sawtooth mountain range to the east which reaches a maximum of 1095 m in elevation (Fig. 3.1). The FP is underlain by the Sverdrup Basin, a folded and faulted Carboniferous to Paleogene sedimentary bedrock comprised of sandstone, siltstone and shale strata (Bell, 1996; Miall, 1986; Embry & Beauchamp, 2008; Hodgson & Nixon, 1998). The area is dissected by gullies and shallow, snowmelt-fed rivers that flow for three months of the year (Young & Woo, 2000).

3.1. Glaciation and Surficial Sediments

The Late Quaternary glacial history of the Queen Elizabeth Islands has long been studied with contrasting views. Early reconstructions suggested that the region remained largely ice free during the last glacial period due to the absence of glacial activity (J. England, Sharp, Lemmen, & Bednarski, 1991; Hodgson, 1985). However, the most recent reconstruction suggests that the Innuitian Ice Sheet (IIS) covered most of the Queen Elizabeth Islands during the last glaciation and reached its maximum extent at about 15.8 kyr BP with maximum thickness of 1.6 km (Blake Jr., 1970; A S Dyke et al., 2002; J England et al., 2006; Hodgson, 1985; Huges, Denton, & Grosswald, 1977; Simon, James, & Dyke, 2015). On the Fosheim Peninsula, the ice originated from the confluence of ice buildup on the western side of the Ellesmere Ice Divide and ice flowing from Axel Heiberg. Deglaciation in the ESL started between 10.3 - 8.7 kyr BP and continued to retreat inland on Ellesmere and Axel Heiberg islands to current extents (England et al., 2006). Remnants of the IIS are found at the nearby Agassiz Ice Cap and Prince of Wales Ice Field to the east, and Mueller Ice Cap to the west. Marine transgression in the ESL occurred until 8.8 – 7.8 kyr BP and inundated approximately one-third of the peninsula. Holocene marine limit varies between 139 and 150 m a.s.l. across the FP (Bell, 1996): it is found at 143 m a.s.l. at Eureka Sound (England et al., 2006); but, near the Eureka Weather Station, the marine limit reaches 146 m a.s.l. (Bell, 1996). The post-glacial isostatic rebound around Eureka was high between 10 - 8 kyr BP, and nearly complete by 2.5 kyr BP (Simon et al., 2015).

Weathered bedrock is the most common surficial sediments unit on the FP with advanced surface weathering present on many bedrock outcrops as well as the presence of glacial erratics (T. Bell & Hodgson, 2000). Till deposits are divided into two units: blanket and veneer. Blanket till is thick (>2m) and completely covers the underlying bedrock structure in comparison, and the surface of veneer till mimics the underlying bedrock structure (Bell & Hodgson, 2000). In addition, glaciofluvial sediments deposited in meltwater channels are found above marine limit with extensive gravel deposits located on the northeastern section of the FP (Bell & Hodgson, 2000). Holocene marine deposits accumulated along coastal lowlands below marine-limit and the 5-10 m thick deposits vary in size from clays to sands (Hodgson & Nixon, 1998; Bell & Hodgson, 2000). Fluvial deposits composed of gravel and sand are a minor surficial unit on the peninsula (Bell & Hodgson, 2000). Other minor surficial material includes: eolian sediments,

organic deposits (peat) and colluvium. Eolian sediments such as wind-blown sand and coarse silt lie adjacent to poorly vegetated fluvial sediments (Bell & Hodgson, 2000). Organic deposits composed of mosses and vascular plants accumulate in abandoned stream valleys and surface depressions. Finally, colluvium deposits are formed primarily from solifluction and rill washing along hillslopes, and slope failures are locally significant on fine-grained material (Bell & Hodgson, 2000). Figure 3.2 shows the Holocene surficial materials for the FP, while eolian, organic and colluvium deposits are not shown due to their low occurrence.

3.3. Modern and Holocene Climate

The ESL is considered a polar desert, with cold winter and cool summer temperatures and very little precipitation. It is subject to the 'coastal effect' where coastal locations have cooler summer air temperatures relative to inland locations (Atkintson, 2000). Local weather has been recorded since 1947 at Eureka by an automated weather station, the closest station to the study sites (Government of Canada, 2020; Rae, 1951). Between 1980-2016, the mean annual air temperature (MAAT) for Eureka was -18.5±1.4°C; mean winter air temperature (DJF) is -38.5±1.7°C; mean summer air temperature (JJA) is 4.3±1.3°C but it can reach +15°C (Fig. 3.3 B; Government of Canada, 2020; Atkinson et al., 2000). The MAAT at Eureka shows strong inter-annual variations and experienced a general decrease from the 1950s to the mid-1970s. This cooling was followed by a statistically significant increase in MAAT at a rate of 1.07°C decade^{-1} over the period 1970-2010, with most warming occurring in the fall and winter (Fig. 3.3 A).

Total precipitation for Eureka is relatively low (1980-2016: 77.6 ± 25.8 mm y^{-1}, with 80% falling as snow; Fig. 3.3 A & B) compared to other High Arctic locations; ex. Alert, Nu situated ~550 km away receives 144.3 ± 41.3 mm y^{-1} (Government of Canada, 2020). The average snow depth in Eureka was 14.9± 6.3 cm over the period 1980 to 2016 (Government of Canada, 2020). Maximum snow depths are reached in April and decrease rapidly with spring snowmelt (Alt et al., 2000). Rainfall events are typically low (<0.03mm) but can reach >10mm. Total precipitation increased at a rate of 16.7% decade^{-1} over the period 1950 to 2010. The low precipitation around Eureka is attributed to the surrounding topography which blocks cold ocean air masses and creates a rain-shadow (Edlund & Alt, 1989; Bell, 1996; Alt & Maxwell, 2000).

Holocene air temperatures were reconstructed from $\delta^{18}O$ measurements from the Agassiz Ice Cap (Lecavalier et al., 2017). The 25-year resolution temperature time-series shows a rapid early Holocene warming with a peak of 6.1 °C at 10 ka followed by a gradual cooling to 1700 CE (Fig. 3.4 A). Air temperatures in this region are rapidly warming and are now at their warmest in the past 6800–7800 years. The recent rate of temperature change is unprecedented over the entire Holocene (Lecavalier et al. 2017). High peat accumulation rates during the early- to mid-Holocene suggests warmer and wetter climate conditions in the FP (Garneau, 2000). Holocene precipitation records from lake sediment cores retrieved from Victoria Island (~1400 km away) show an increase in precipitation of ~25 mm between 10 ka to 9.7 ka and remained high until c. 5 ka (Fig. 3.4 D). Precipitation declined near the start of the late Holocene by ~10 mm and remained low until 1 ka when they increased again by ~10 mm (Peros & Gajewski, 2008).

3.4. Modern and Holocene Vegetation

The FP is located within the Eriched Prostrate Shrub Zone, where it is characterized as having the greatest diversity and density of vascular plant species of the Queen Elizabeth Islands (Fig. 3.5; Edlund et al., 2000; Edlund and Alt, 1989). Woody plants (i.e. *Salix arctica* and *Dryas integrifolia*) dominate the moderate to well-drained soils below 300-500 m a.s.l. (Edlund et al., 2000). *Salix arctica* dominates the majority of slopes, rooting in shallow troughs, major cracks between hummocks and in shallow depressions. Whereas *Dryas integrifolia* is more common in sandier soils and in more microhabitats (Edlund et al., 2000). Other less common species include: *Cassiope tetragona, Vaccinium uliginosum* as well as the rare occurrence of *Pyrola graniflora* (Edlund et al., 2000). Vegetation in low-centred polygons are characterized by *Alopecurus alpinus, Poa alpigena, Salix arctica* and *Stellaria longipes*. Species of *Puccinella* (i.e. *P. augustate, P. langeana* and *P. poacea*) and *Poa* (*P. hartzii* and *P. glauca*) dominate silty knolls and slopes where the surface has salt accumulations (Eldund et al., 2000). Wetlands are common to lowland areas and are located in poorly drained troughs and trough junctions or near a headwater lake or pond. These wetlands are dominated by sedge-meadow vegetation with thick bryophytic mats (Eldund et al., 2000).

Vegetation colonized the CAA following the post-glacial marine emergence (Garneau, 2000; Gajewski, 2015). The majority of local flora would have migrated during the postglacial, however, there is a possibility that some of the species remained during the full glacial in dynamic refugia (Gajewski, 2015). Maximum development of vegetation in the area occurred shortly after deglaciation. Subsequent changes throughout the Holocene consist of increases in plant density and changes to the relative proportion of taxa (Gajewski, 2015). Plant species remained present in the CAA throughout the Holocene, and no evidence in the pollen fossil record suggests the arrival or disappearance of new taxon during the mid- and late-Holocene (Gajewski, 2015). Peat studies reveal the area was dominated by sedges and grasses, establishing a 'pioneer meadow'. Alternating layers dominated by herbs or mosses reflect permafrost aggradation as polygon troughs and ridges were colonized (Garneau, 2000). The pollen fossil record for the CAA closely resembles the modern pollen record, indicating a lack of significant biodiversity change in the CAA throughout the Holocene (Gajewski, 2015).

3.5. Permafrost and Ground Ice

The ESL is located within the continuous permafrost zone, with permafrost being >500m thick (Pollard et al., 2015). The active layer depth varies between 10 and 100 cm , with an average around 60 cm (Hodgson & Nixon, 1998). The mean annual ground temperature (measured at depth of zero annual amplitude) remains <-10ºC all year (Hjort et al., 2018). Borehole temperature records from Alert, Nunavut, show a +0.2°C decade^{-1} to +0.6°C decade^{-1} increase in mean annual ground temperature between 1979 and 2008 (Smith et al., 2010). This increase is attributed to the thin snow cover, which acts as a poor buffer to fall and winter air temperature changes (Smith et al., 2010). Riseborough and Smith (1998) showed that the value of the freezing N-factor (ratio of winter temperature at the ground surface to that in the air) is a function of snow thickness and MAAT. At Eureka, the MAAT is -18.5 ± 1.4°C and the snow on the ground in late winter averages 14.9 ± 6.3 cm (1980-2016), giving a freezing N-factor near 0.85.

Based on the estimated freezing N-factor, the winter ground surface temperatures (c. -32.7°C) are slightly warmer than that in the air (-38.5±1.7°C).

Tundra polygon is the main periglacial landform, covering approximately 50% of the Fosheim Peninsula, most of which is found within marine limit (Couture & Pollard, 1998; Bernard-Grand'Maison & Pollard, 2018). Thaw slumps and active layer detachment slides are the other main permafrost landforms found in the area. Ground ice in the Fosheim region is estimated to occupy 30% $_{vol}$ of the uppermost 6 m of permafrost (Couture & Pollard, 1998). Of that, 3.5% $_{vol}$ is estimated to be wedge ice and the remaining occurs mostly as tabular bodies of massive ice (Couture & Pollard, 1998). The ice wedges are mostly epigenetic in nature (Pollard, 1991), but syngenetic ice wedges are found in places of recent colluviation and permafrost aggradation (Lewkowicz, 1994). Cryostratigraphic observations and tritium analyses of ice wedges with multiple growth stages showed the development of secondary and tertiary wedges in modern times (post 1957) due to active colluviation along hillslopes. Rates of modern ice wedge growth were estimated at 1.9-4.8 mm yr^{-1} (Lewkowicz, 1994).

The increasing MAAT over the past 40 years has implications on the stability of permafrost in the ESL (ex. Pollard et al., 2015). In recent years, tundra polygons and ice wedges were found to be degrading at a rate synchronous with the active layer thickening; the number of active thaw slumps have also been increasing (Pollard et al., 2015). The troughs of tundra polygons in the ESL experienced a significant amount of degradation for a cold polar desert (Ward-Jones et al., 2020). However, troughs with a greater vegetation cover experienced less degradation than troughs with little to no vegetation due to the insulating property of vegetation during the summer which in turn reduced active layer thaw depth (Becker, Davies, & Pollard, 2016; Ward Jones et al., 2020). Degradation of the troughs that lack vegetation likely results from a combination of higher soil moisture content that delays freezing in the winter and increases thaw depth in the summer, and from an increase in snow thickness within the troughs that leads to warmer winter ground temperatures (Ward-Jones et al., 2020).

3.6. Human Occupancy

Prehistoric human occupation of the FP took place during two periods, one 2500-1000 BC and the other between 700 and 1700 AD (Sutherland, 2000). Independence I, Late Dorset and Thule Inuit once occupied the coastal areas of the FP (Sutherland, 2000). Current human occupation of the peninsula consists of Canadian research and military bases. Environment Canada has had a weather monitoring station on the FP since 1947. Between 1947 and 1951, the old airstrip was built and then quickly decommissioned due to ice wedge degradation from poor construction and the removal of surface vegetation (Hodgson & Nixon, 1998). The current airstrip was constructed in 1951 and later built up with coarser materials to maintain the airstrip's stability (Hodgson & Nixon, 1998). The Canadian military base is located beside the new Eureka Airstrip. The PEARL weather monitoring station is operated by CANDAC, located 15 km north of the Eureka Weather Station, and has been in operation since 2005.

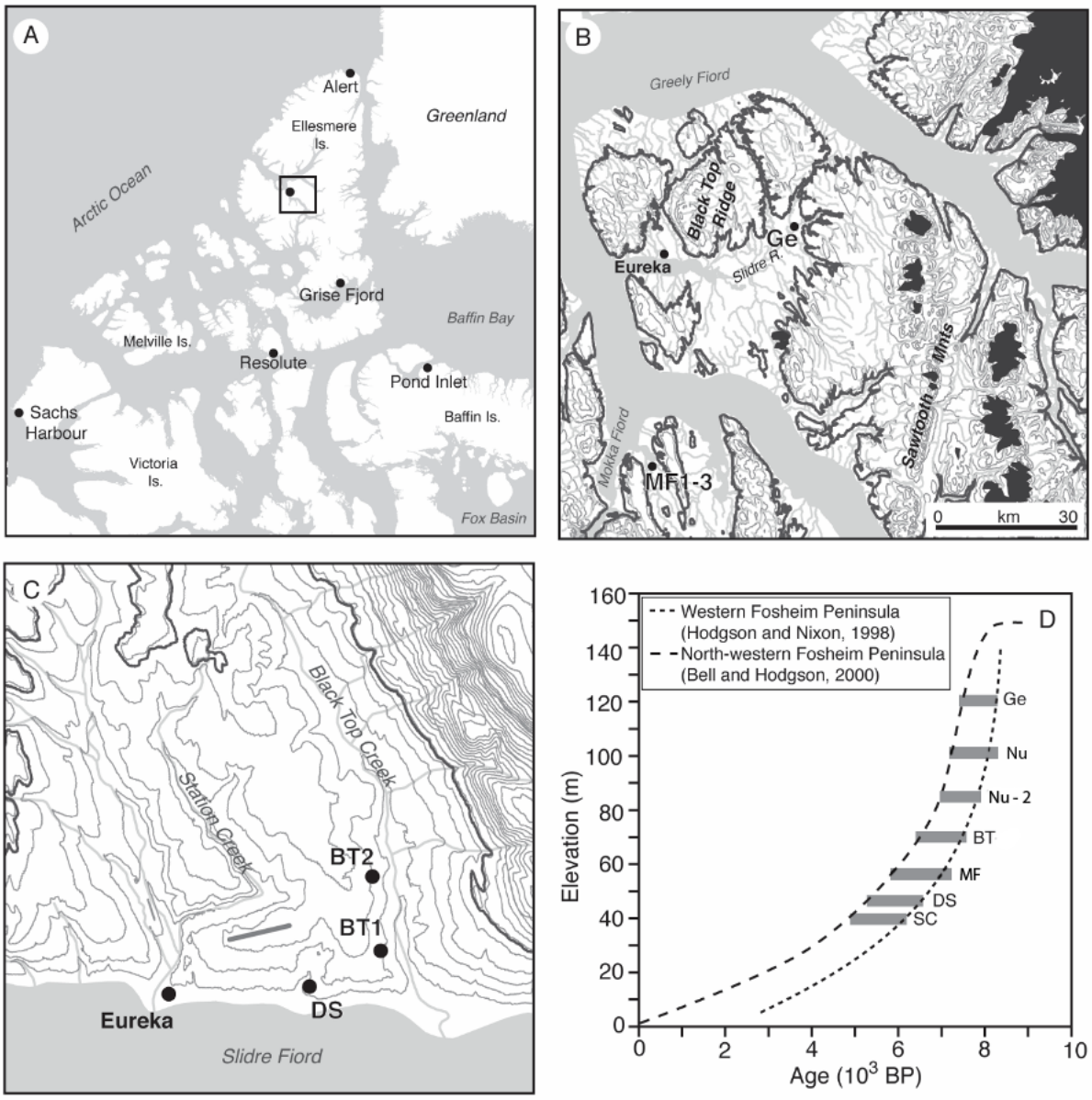

Figure 3.1. Location map of (A) Canadian Arctic Archipelago, (B) Fosheim Peninsula, and (C) Eureka with sampled thaw slumps mapped (SC- Station Creek (Roy, 2018), DS – Dump Slump, BT - Blacktop Slump, MF- Mokka Fjord Slump, Nu – Nunavut Slump (2 elevations) and Ge – Gemini Slump). (D) Ice wedge ages and respective elevation are compared against the marine emergence curves for the Eureka Sound Lowlands developed by Hodgson & Nixon (1998) and Bell & Hodgson (2000).

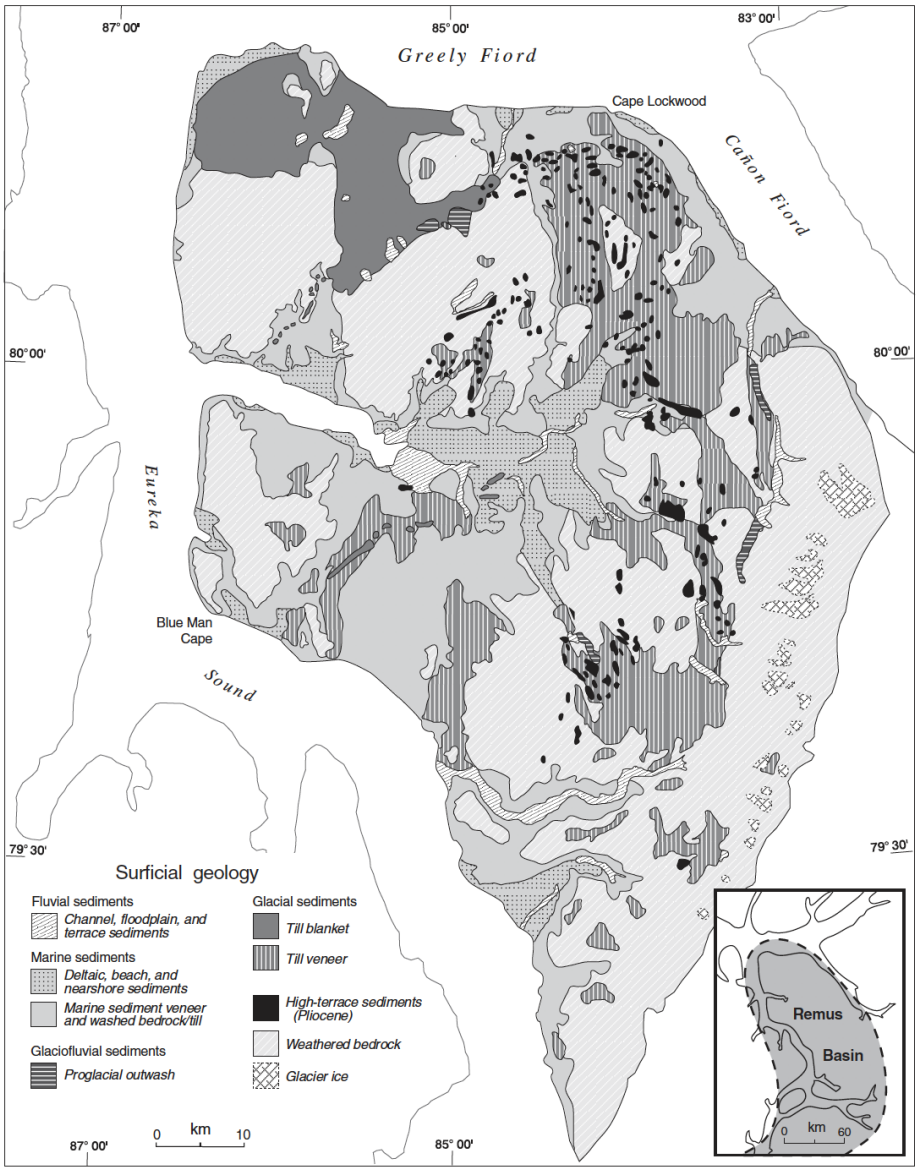

Figure 3.2. Surficial geology map of northwestern Fosheim Peninsula (Bell & Hodgson, 2000).

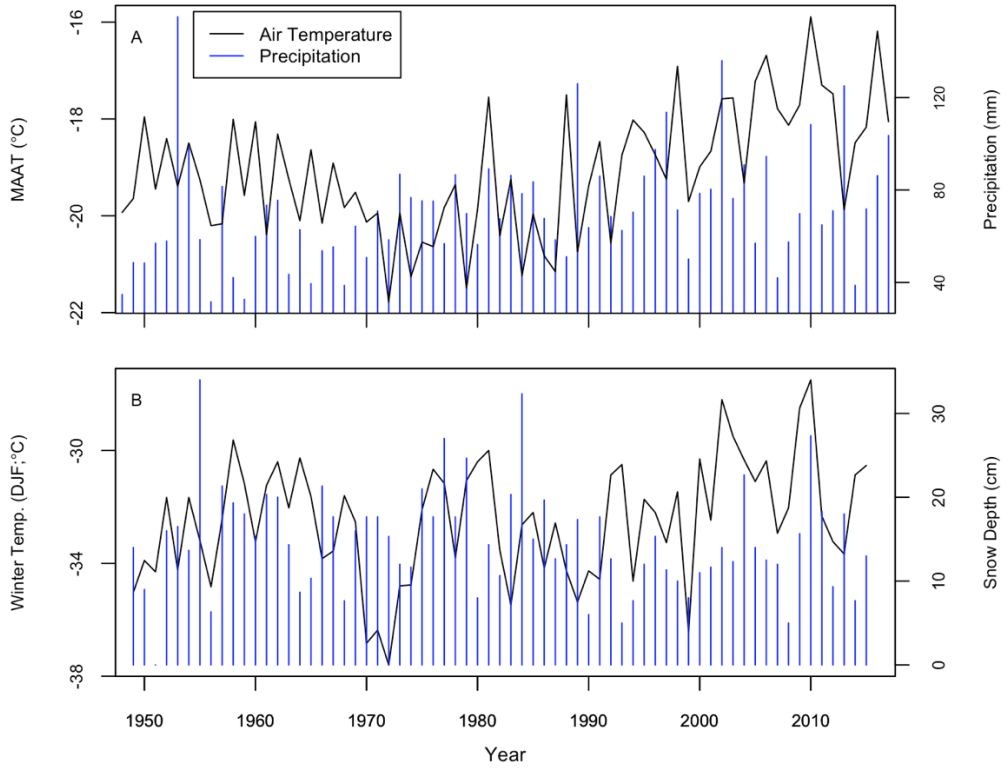

Figure 3.3. Climate records. (A) Eureka, Nunavut, current mean annual temperature (MAAT, °C) and total yearly precipitation (mm) for 1947-2015 (Government of Canada, 2020). (B) Eureka Winter (DJF) mean temperature (°C) and mean winter (DJF) snow on ground (cm).

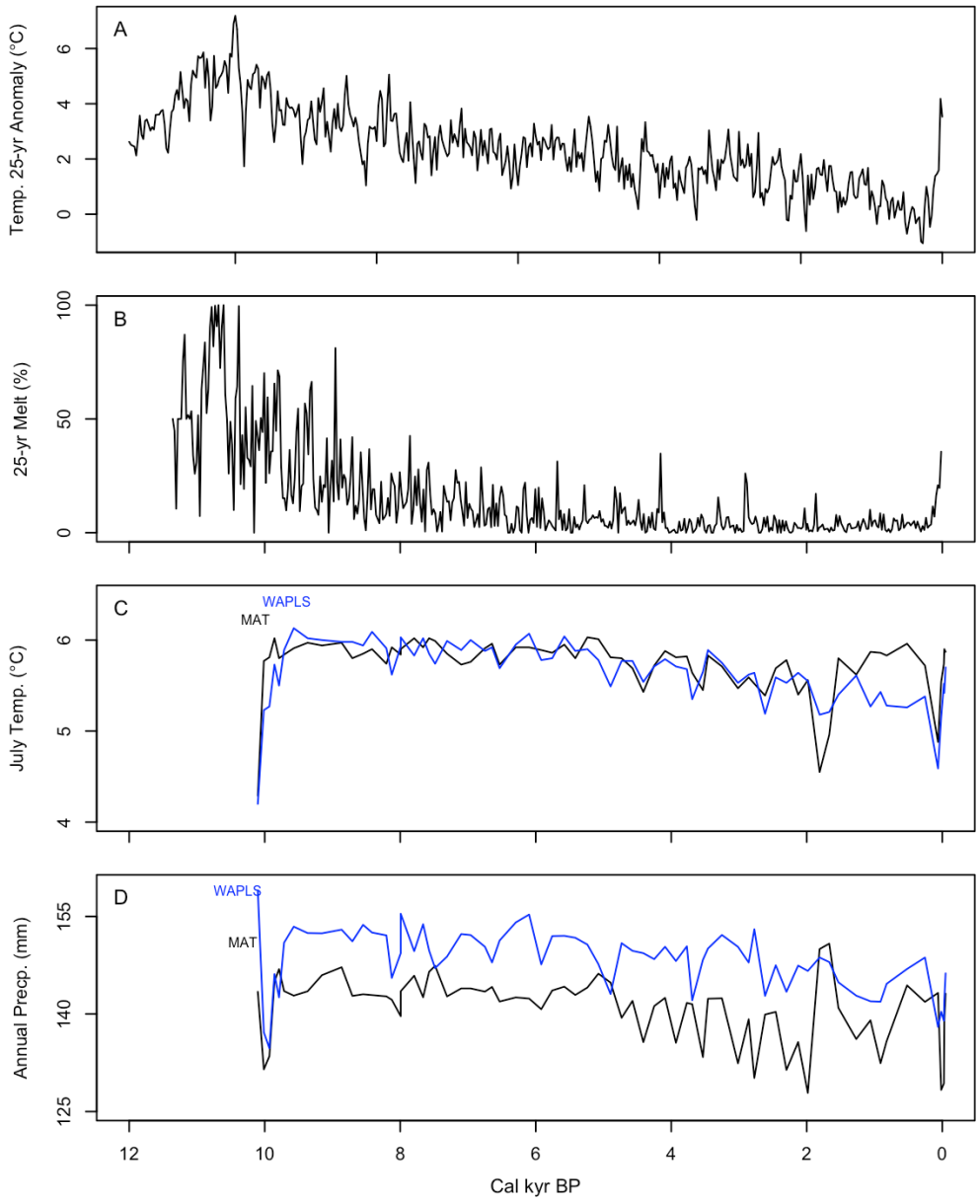

Figure 3.4. Holocene climate reconstruction. (A) Agassiz Ice Cap 25-year (annual) temperature anomaly reconstruction (Lecavalier et al., 2017). (B) Agassiz Ice Cap 25-year summer melt reconstruction (Fisher et al., 2002). (C) July temperature reconstruction from Lake KR02, Victoria Island, NWT/Nu (Peros & Gajewski, 2008). (D) Annual precipitation reconstruction from Lake KR02, Victoria Island, NWT/Nu (Peros & Gajewski, 2008). For C and D, the modern analogue technique (MAT) is featured in black, the weighted averaging partial least squares (WAPLS) is featured in blue.

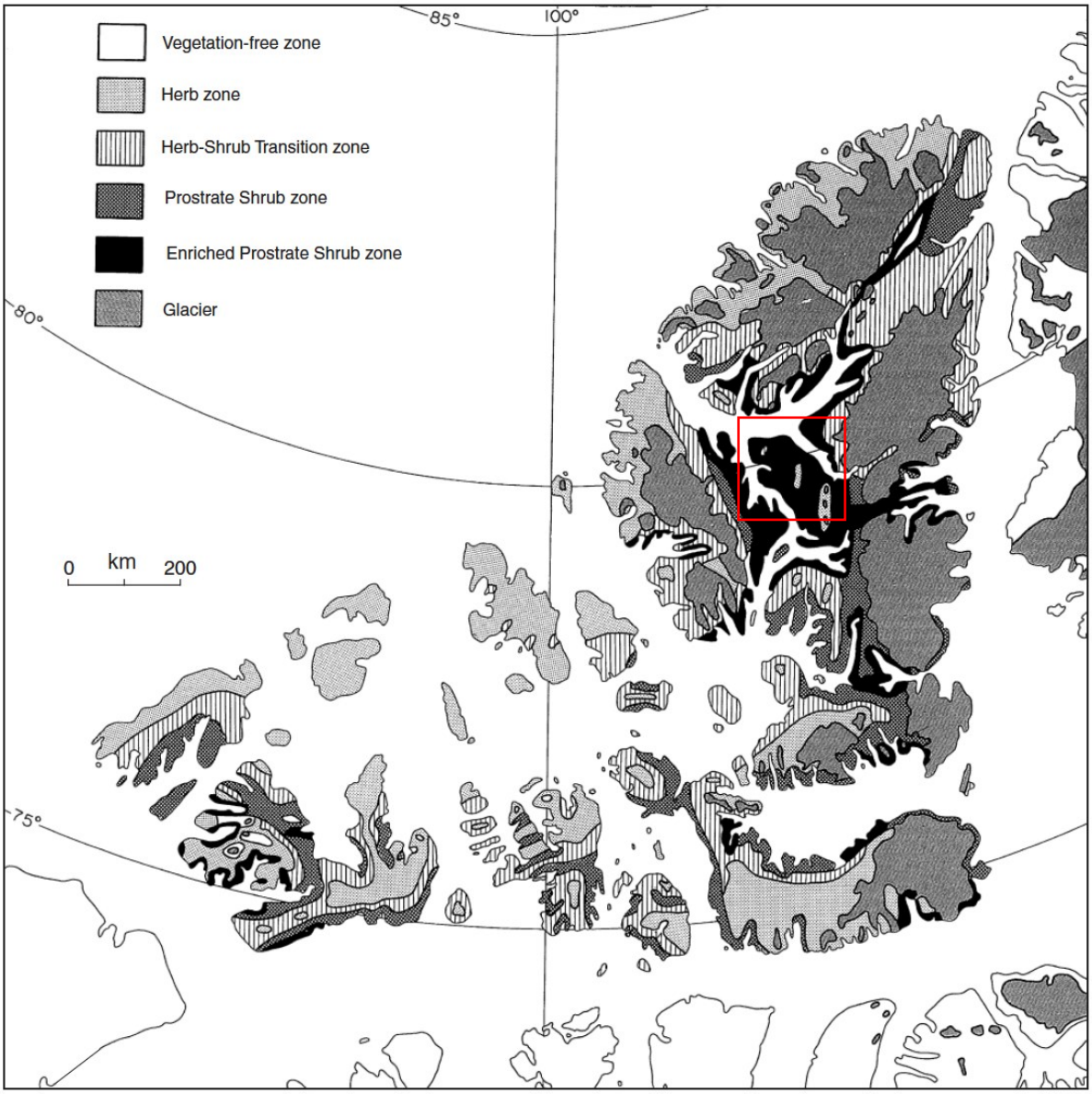

Figure 3.5. Vegetation zones for the Queen Elizabeth Islands based on the growth forms of the dominant vascular-plant species decribed in Edlund and Garneau (2000). Zones are summarires of patterns seen on 1:250 000 scale vegetation maps, with the red square highlighting the Fosheim Peninsula. Map adapted from Edlund et al. (2000).

Chapter 4: Methods

4.1. Field Sample Collection

Ice wedges were sampled from the headwall of thaw slumps but had to meet a few conditions before sampling. First, the ice wedge (IW) had to be growing perpendicular or near perpendicular to the slump headwall, and second, the ice wedge had to be accessible for safe sampling. Four slumps in proximity to Eureka were selected: Dump Slump, Black Top Slump, Nunavut Slump and Mokka Fjord Slump (Table 4.1). In total, nine ice wedges were sampled with two to five cores taken from each (Fig. 4.1). The active layer above each ice wedge was also sampled.

4.1.1. Ice Wedge Sample Collection

Ice wedge samples were collected in July 2018 and July 2019 (Table 4.1). In the first summer, the ice wedges were sampled horizontally at various depths. To sample the ice wedges horizontally, a stable drilling platform was created on the slump floor adjacent to the wedge, and an ice axe was used to chip into the icy permafrost adjacent to the ice wedge. A CRREL coring kit was used to drill horizontally across the entire ice wedge and three to four cores were collected from the same wedge at 30 cm depth intervals (Fig. 4.2 A & B). In July 2019, eight ice wedges were sampled vertically from the top downwards at three to five locations across the exposed surface of each wedge. The active layer soil was first removed, exposing the full width of the ice wedge, and the ice wedge was cored at its centre and edges with a mini-CRREL coring kit from its surface to 30 cm depth. The horizontal cores were analyzed for high-resolution δD-$\delta^{18}O$ analyses (1.5 cm resolution), whereas the vertical cores were analyzed as a bulk sample for major ions, δD-$\delta^{18}O$, DOC, $\delta^{13}C_{DOC}$ and $^{14}C_{DOC}$. All ice wedge cores were wrapped in aluminum foil, kept frozen in a chest freezer in Eureka, and then shipped frozen to the CryoLab for Arctic, AntArctic and Planetary Studies (CLAAPS) laboratory at the University of Ottawa.

Table 4.1 Ice wedges sampled from Eureka (EU) and Mokka Fjord (MF). All IWs were sampled in July 2018 and July 2019.

Location	Year Sampled	Wedge Number	Slump name	Latitude, Longitude	Elevation (m a.s.l.)	Number of cores	Total Width (m)
EU	2018	1[a]	Black Top	N 79.98554, W 085.70804	66	3	1.6
EU	2018	2[b]	Dump	N 79.98291, W 085.78497	36	3	0.71
EU	2018	3	Black Top	N 79.98545, W 085.70732	65	4	0.36
EU	2018	4[c]	Nunavut	N 79.99950, W 085.68517	73	4	0.36
EU	2019	1[b]	Dump	N 79.982996, W 085.784482	33.5	5*	3.49
EU	2019	2[a]	Black Top	N 79.985492, W 085.708244	60	3*	1.14
EU	2019	3[c]	Nunavut	N 79.999555, W 085.686158	99	3*	0.91
EU	2019	4	Nunavut	N 79.999605, W 085.686454	100	3*	4.5
EU	2019	5	Nunavut	N 80047, W 085.687444	78	3*	0.40
MF	2019	1	Mokka Fjord 1	N 79.522892, W 086.806889	57.6	3*	3.3
MF	2019	2	Mokka Fjord 1	N 79.523235, W 086.806779	54.8	3*	3.3
MF	2019	3	Mokka Fjord 1	N 79.52277, W 086.806578	56.8	3*	4.53

* Vertical ice cores extracted from the wedge

[a, b, c] indicates the same ice wedge, sampled in two different years

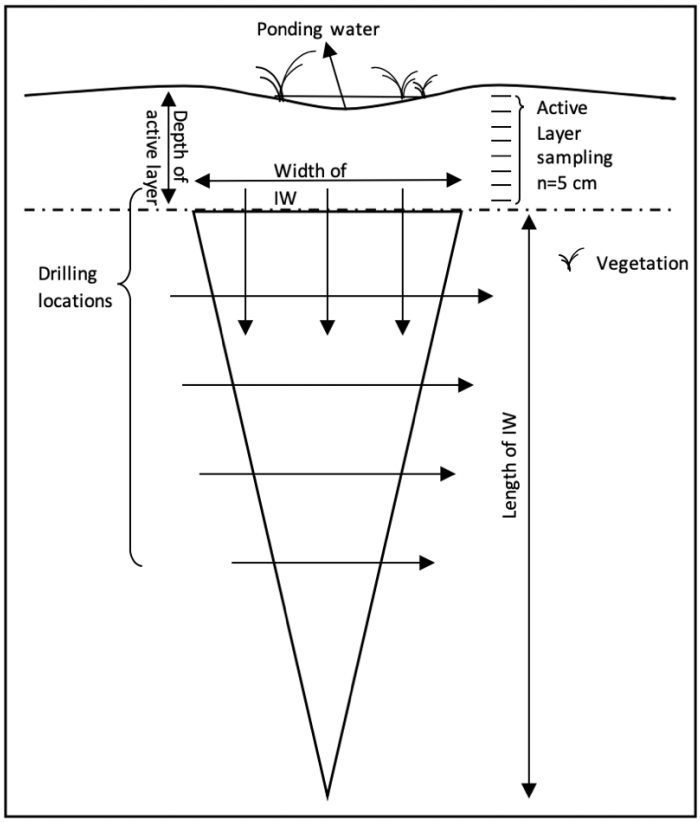

Figure 4.1. Diagram of active layer, ice wedge and ponding water sampling methods. The horizontal cores were analyzed for high-resolution δD- $\delta^{18}O$ analyses whereas the vertical cores were analyzed for major ions, δD-$\delta^{18}O$, DOC, $\delta^{13}C_{DOC}$ and $^{14}C_{DOC}$.

Figure 4.2. Images of ice wedge sampling. (A-B) horizontal drilling of ice wedge at Dump slump (EU18-W2), (C) vertical samplings of ice wedge at Mokka Fjord (MF-W3).

4.1.2. Active Layer Sample Collection

Samples of active layer soils were collected above each of the sampled ice wedge and analyzed to determine the major soluble ions and dissolved organic carbon (DOC) content. The active layer was sampled at 5 cm interval using a trowel and ~300 g was collected in medium Ziploc Freezer bags (Table 4.2). Samples were shipped back to the University of Ottawa for analyses.

Table 4.2. Active layer (AL) sample collection location, slump, recorded depth, number of samples taken and related ice wedges.

Location	Slump	Depth (cm)	No. of samples	Related ice wedges
EU	Dump	70	15	EU18-W2, EU19-W1
EU	Blacktop	60	12	EU18-W1, EU18-W3, EU19-W2
EU	Nunavut	60	13	EU18-W4, EU19-W3, EU19-W4, EU19-W5
MF	Mokka Fjord	50	10	MF-W1, MF-W2, MF-W3

4.1.3. Surface Water Sample Collection

Samples from snow, ponds, streams and the Eureka Fjord were collected to determine their DOC content, geochemical and δD-δ^{18}O composition and compared to that of the ice wedges. The pH, temperature (°C) and conductivity (µm/ cm) was measured using a VWR instrument (SympHany Multisensory Probe 89231-650 and Handheld Meter H30PCO). The water samples were filtered with 0.45 µm cellulose nitrate membrane filters and stored at 4°C until analyses. Samples for geochemistry and δD-δ^{18}O analyses were collected in well-sealed two 20ml HDPE bottles.

Table 4.3.Collected water samples from Eureka Sound Lowlands.

Water Body	Year	Elevation (m)
Snowbank	2017	-
Pond	2018	69
Pond	2018	66
Pond	2018	98
Creek	2018	0
Creek	2018	-9
Fjord	2018	-10
Snowbank	2018	-
Fjord	2019	-

4.2. Laboratory Analyses

4.2.1. Ice Wedge Preparation

The ice wedge core samples were processed in the CLAAPS at the University of Ottawa. The horizontal ice cores were first cut in half and then sub-sampled at 1.5 cm interval along the growth axis using a Ryobi Tile Saw with a 0.8 mm diameter blade. An individual ice vein typically is <1 mm to a few mm wide (Mackay, 1972; Mackay 1974; Lewkowicz, 1994), therefore each sample represents an average of multiple veins. The remaining half of the core was rewrapped and archived in the -18℃ freezer. The samples were transferred into sealed Freezer Ziploc bags and left to thaw at room temperature (25℃). Once thawed, the subsamples were transferred into well-sealed 15ml plastic vials and left to settle. The vertical ice cores were first thawed in 500mL glass beakers covered with plastic wrap and sealed with electrical tape to ensure there was no evaporation. The samples were left to thaw and settle for three days at room temperature. All samples were then filtered in pre-rinsed 0.45 mm nitrate cellulose filters. These samples were stored in well-sealed 20mL plastic vials for δD-δ^{18}O and major ions analysis. Select samples for DOC and $^{13}C_{DOC}$ were transferred in 40ml amber glass vials and samples for $^{14}C_{DOC}$ were transferred in pre-baked 1L glass amber bottles.

4.2.2. Active Layer Samples

The active layer soil samples were analyzed for gravimetric water content, organic matter and carbonate contents, leached soluble ions and DOC. First the soil samples were weighed (to the 0.1g) and transferred to 9" aluminum pie plates and dried in the oven (VWR Scientific Products 1370 FM) at 105ºC for 24 hours. The dried weight of each sample was recorded and used to determine the gravimetric water content using the following equation:

$$\text{Gravimetric water content (\%)} = (\text{wet weight-dry weight})/\text{dry weight} * 100 \quad (4)$$

where wet weight is the weight of the wet sample (g) and the dry weight is the weight of the sample after drying at 105ºC.

A Loss-on-Ignition (LOI) analysis was conducted on the soil samples to determine organic matter and carbonate contents. Samples were analyzed using the LECO TGA 701 Thermogravimetric Analyzer. The percent mass was calculated using the following equations (Heiri, Lotter, & Lemeke, 2001).

$$\text{Organic matter (\%)} = ((DW_{105}-DW_{550})/DW_{105})*100 \quad (5)$$

$$\text{Carbonate (\%)} = [((DW_{550}-DW_{950})/DW_{105})*100]*1.36 \quad (6)$$

where DW_{105} is the dry weight of the sample at 105°C; DW_{550} is the dry weight of the sample at 550°C after combustion; DW_{950} is the dry weight of the sample after combustion at 950°C. The LOI_{950} mass percent must be multiplied by 1.36 to account for the difference in molecular weight between carbon dioxide and carbonate. The mass at each temperature step (105, 550, 950°C) was recorded by the analyzer once its variation reached < 0.1%. An internal standard (calcium oxalate) and 5% duplicates were also analyzed, and the analytical reproducibility was ± 0.1%. Results are expressed as percentages (%).

The total water-soluble ions (major ions and DOC) in the active layer samples were determined in the laboratory of dried soils using a 1:10 soil-water ratio (e.g., Conklin Jr, 2005). A sub sample (5g) of the dried active layer sample (< 2mm) was disaggregated with a porcelain mortar and pestle and 5g of the disaggregated material was transferred into 250ml conical tubes and mixed with 50g of deionized water. These subsamples were then shaken (Wrist Action Shaker, model 75, at highest setting) for an hour then left to sit at room temperature for 24 hours. Next, the samples were centrifuged (Thermo Scientific Sorvall ST40 Centrifuge) for 14 minutes at 2700 rpm. The supernatant water from each sample was extracted and filtered first with 5 µm then 0.45 µm pre-rinsed cellulose nitrate membrane filters. These filters were pre-rinsed with DI water to ensure no DOC was leaching into the sample from the filters. These samples were stored at 4°C until analyses.

4.2.3. Geochemical Analysis

Major cation and anion from melted ice wedges, leached active layer, and the different types of surface waters were analyzed in the Geochemical Laboratories at the University of Ottawa. The samples for cation analysis were acidified with 0.1ml of 1% ultra-pure nitric acid (HNO_3). The cations (K^+, Na^+, Fe_{tot}, Ca^{2+}, Sr^{2+} and, Mg^{2+}) were analyzed with an Agilent 4100 Microwave Plasma Emission Spectrometer (MP-ES). The anions (Cl^-, SO_4^{2-} and, NO_3^-) were analyzed unacidified by a DIONEX Ion Chromatograph (IC). Analytical precision is ± 5% for cations and anions. To facilitate a comparison between melted ice wedge samples and leached active layer samples, the results were then converted to molar ratios with respect to Cl, a conservative tracer.

4.2.4. Stable Water Isotopes Analysis

The $^{18}O/^{16}O$ and D/H ratios of the surface waters and wedge ice were determined using a Los Gatos Research liquid water analyzer coupled with a CTC LC-PAL auto sampler and verified for spectral interference contamination. The results are presented using the δ-notation ($\delta^{18}O$ and δD), where δ represents the parts per thousand differences for $^{18}O/^{16}O$ or D/H in a sample with respect to Vienna Standard Mean Ocean Water (VSMOW). Duplicates (5%) were also analysed, analytical reproducibility for $\delta^{18}O$ and δD was ±0.3‰ and ±1‰, respectively. Deuterium-excess (*d*) was then calculated using the following equation ($d = \delta D - 8\ \delta^{18}O$; Dansgaard, 1969).

4.2.5. DOC and $\delta^{13}C_{DOC}$ Analysis

The DOC and its stable isotope ratio ($\delta^{13}C_{DOC}$) of wedge ice, surface water and leached active layer water samples were analyzed in the Ján Veizer Stable Isotope Laboratory at the University of Ottawa. The DOC concentration and $\delta^{13}C_{DOC}$ were measured by a wet TOC analyzer interfaced with a Thermo DeltaPlus XP isotope-ratio mass spectrometer using methods described by St-Jean (2003). The isotope ratios are presented as permil (‰) deviation relative to VPDB and expressed using the delta-notation. The 2σ analytical precision is ± 0.5 ppm for DOC concentration and ± 0.2‰ for $\delta^{13}C_{TOC}$.

4.2.6. Radiocarbon Analysis of Dissolved Organic Carbon (DOC)

Radiocarbon analysis of the DOC of vertical ice wedge samples was performed at the A.E. Lalonde Accelerator Mass Spectrometry Laboratory, University of Ottawa. Sample preparation including the extraction of DOC from waters and graphitization for ^{14}C analysis is described by Murseli et al. (2019). Graphitized samples were analyzed on a 3MV tandem mass spectrometer (Kieser et al., 2015). The $^{14}C/^{12}C$ ratios are expressed as fraction of Modern Carbon ($F^{14}C$) and corrected for spectrometer and preparation fractionation using the AMS measured $^{13}C/^{12}C$ ratio (Crann et al., 2017). Radiocarbon ages are calculated as $-8033\ln(F^{14}C)$ and reported in ^{14}C yr BP (BP=AD1950) as described by (Stuiver & Polach, 1977). The 2σ errors are reported in Appendix F and are below 0.013 $F^{14}C$ (or <190 years). The measurements were then converted to calendar years (cal yr BP) using OxCal v4.2.4 and the IntCal13 calibration curve expressed by Bronk Ramsey (2009) and Reimer et al. (2013).

4.3. Data Analysis

Datasets were imported into R Studio for statistical analysis. The Shapiro-Wilk test for normality was performed on the data of the ice wedges, active layer and snow samples and it was determined that the data should be natural $\log_e$ transformed to meet the assumption of normality. An ANOVA and Tukey's HSD tests were conducted on each of the horizontally sampled ice wedges to assess whether the log-transformed mean of $\delta^{18}O$ and D-excess between depths within a wedge were statistically different from each other (see Appendix A for ANOVA and Tukey's HSD code). An ANOVA test provided the F-value and p-value which indicated whether or not to reject the null hypothesis (null: no significant difference observed within the ice wedge). If the null was rejected ($p \leq 0.05$) then a Tukey's HSD test was performed to identify where the difference was located (i.e. between which depths). Two-tailed t-tests of different variances were conducted on the left and right sides of the horizontal IW $\delta^{18}O$ and δD to determine if the mean values of either side were significantly different. Another two-tailed t-test was conducted on the mean molar ratio for each vertical ice wedge sample and the corresponding active layer to determine if the ice wedge samples were significantly different.

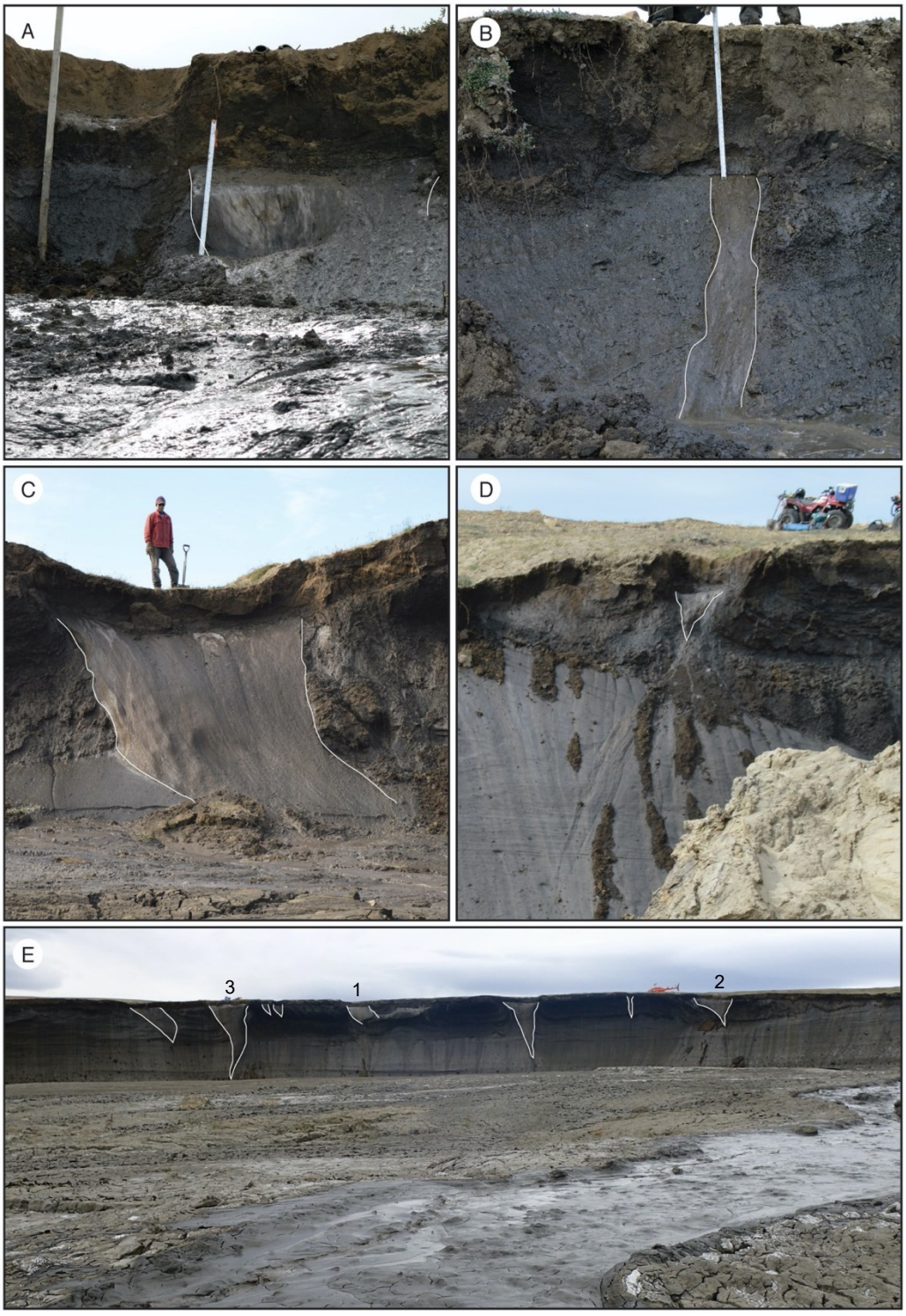

Figure 4.3. Images of sampled ice wedges from Eureka Sound Lowland and Mokka Fjord. (A) Blacktop slump, EU18-W1, (B) Blacktop slump, EU18-W2, (C) Nunavut slump, EU19-W4, (D) Nunavut slump EU19-W5, (E) Mokka Fjord, MF-W1 to W3.

Chapter 5: Results

In the Eureka Sound Lowlands (ESL), ice wedges (IWs) were sampled from the headwall of thaw slumps at four sites along an elevation gradient between Holocene marine limit (143 m) and modern sea-level. These sites are called: Nunavut slump (73-100m), Black Top slump (60-66m), Mokka Fjord slump (55-58m) and Dump slump (34-36m). At Nunavut, Blacktop and Mokka Fjord, the ice wedges developed in Holocene-age marine sediments (ice silty-clay loam; Roy, 2018); whereas at Dump slump, the ice wedges developed in massive ice. At each site, two to four ice wedges were sampled, with three to five 30 cm deep cores collected from the surface of each ice wedge (IW) and analyzed for major ions, DOC, $\delta^{13}C_{DOC}$, $^{14}C_{DOC}$ and δD-$\delta^{18}O$, and two to four cores collected horizontally at different depths across the entire wedge and analyzed for δD-$\delta^{18}O$ at high-resolution.

5.1. Nunavut Slump (73-100 m)

At Nunavut slump, three IWs were sampled (EU19-W3, EU19-W4, and EU19-W5) from the surface to 30 cm depth at their center and edges, and all three wedges had similar geochemical composition (Fig. 5.1). The concentration of major cations averaged 11.9±6.4 mgL^{-1}, 4.7±3.2 mgL^{-1}, 21.9±14.7 mgL^{-1} for Ca, Mg, Na, respectively; major anions averaged 20.9±14.7 mgL^{-1}, 34.4±21.1 mgL^{-1} for Cl and SO_4, respectively. The DOC averaged 3.6±1.5 mgL^{-1} with the $\delta^{13}C_{DOC}$ averaging –25.1±0.5‰. Comparison with ionic composition of snow and active layer samples were made from the Cl normalized data (Fig. 5.2). The IWs have similar Ca/Cl (0.58±0.29), Mg/Cl (0.34±0.08), Na/Cl (1.68±0.37), SO_4/Cl (0.64±0.21) and DOC/Cl (0.72±0.60) values to that of snow; and with the exception of SO_4/Cl in EU19-W3 and EU19-W4, all molar ratios in the active layer were significantly higher. The $^{14}C_{DOC}$ of the three ice wedges ranged from 8.5 to 6.9 cal kyr BP (Table 5.1). The three IWs were sampled in the center and edges and, with the exception of EU19-W5, a younger age was obtained in the center relative to the edges (Fig. 5.3).

Horizontal cores were obtained at depths: 17, 33, 52, and 76 cm in IW EU18-W4 for high-resolution analysis of δD-$\delta^{18}O$ (Fig. 5.4). The $\delta^{18}O$ values in the four cores ranged from –32.3 to –28.4‰ and all, except the 33 cm depth, showed symmetry around the center of the wedge (Table 5.2). The average $\delta^{18}O$ in the four cores decreased with depth (Fig. 5.4) and an ANOVA test indicated a statistically significant difference; post-hoc Tukey test showed that only the 17 and 33 cm cores and 52 and 76 cm cores had similar average $\delta^{18}O$ values (Table 5.3). The value of the regression slope between δD-$\delta^{18}O$ was 7.0, 5.8, 7.7 and 6.4 for the depths: 17, 33, 52, and 76 cm depths respectively. These are lower than the Eureka local meteoric water line (LMWL: $\delta D = 7.4\ \delta^{18}O - 9.1$; $r^2 = 0.96$; GNIP, 2005; Fig. 5.5). The D-excess values ranged from –2.7‰ to 5.4‰ and all depths were similar around the center of the wedge (Fig. 5.4). The average D-excess with the ice wedge were statistically similar between the four depths (Table 5.3).

5.2. Blacktop Slump (60-66 m)

At Blacktop, one IW was sampled (EU19-W2) from the surface to 30 cm depth at its center and edges. The concentration of major cations averaged 26.6±6.4 mgL^{-1}, 9.4±1.1 mgL^{-1}, 123.5±159.9 mgL^{-1} for Ca, Mg, Na, respectively; major anions averaged 190.8±206.5 mgL^{-1}, 49.9±19.8 mgL^{-1} for Cl and SO_4, respectively (Fig. 5.1). The DOC averaged 5.5±2.9 mgL^{-1} with the $\delta^{13}C_{DOC}$ averaging –24.5±0.1‰ (Fig. 5.1). Comparison with ionic composition of snow and active layer samples were made from the Cl normalized data (Fig. 5.2). The IW has similar Ca/Cl (0.25±0.18), Mg/Cl (0.15±0.13), Na/Cl (0.80±0.28), SO_4/Cl (0.17±0.10) and DOC/Cl (0.14±0.08) values to that of snow; the DOC/Cl, Ca/Cl, Mg/Cl and Na/Cl ratios in the active layer are significantly higher than in the IW. The $^{14}C_{DOC}$ of the IW ranged from 13.7 to 7.2 cal kyr BP (Table 5.1) and the ice was younger in the center relative to the edges (Fig. 5.3).

Two ice wedges were sampled for high-resolution δD-$\delta^{18}O$ analysis (EU18-W1, and EU18-W3). In EU18-W1, the $\delta^{18}O$ values in the three cores (29, 59, 108 cm depths) ranged from –32.7‰ to –27.7‰ and showed little to no symmetry around the center of the wedge (Fig. 5.4; Table 5.2). The average $\delta^{18}O$ in the three cores decreased with depth and an ANOVA and post-hoc Tukey test indicated a statistically significant difference; only the 59 and 108 cm depths were similar (Table 5.3). The value of the regression slope between δD-$\delta^{18}O$ was 6.2, 6.2 and 6.8 for 29, 59 and 108 cm depths, respectively, which are lower than the LMWL (Fig. 5.5). The D-excess values ranged from –5.9‰ to 11.9‰ and showed little to no symmetry around the center of the wedge. An ANOVA and post-hoc Tukey test indicated a statistically significant difference in average D-excess between the three cores; only the 59 and 108 cm depths were similar (Table 5.3).

In EU18-W3, the $\delta^{18}O$ values in the four cores (17, 36, 60, and 83 cm depths) ranged from –29.5 ‰ to –23.5‰ and all showed symmetry around the center of the wedge (Fig. 5.3). The average $\delta^{18}O$ in the four cores remained similar with depth; but an ANOVA and post-hoc Tukey test indicated a statistically significant difference between 36 and 60 cm depths. The value of the regression slope between δD-$\delta^{18}O$ was 7.1, 6.9, 7.6 and 6.5 for the depths 17, 36, 60 and 83 cm , respectively, which are lower than the LMWL. The D-excess values ranged from 0.0‰ to 7.7‰ and showed symmetry around the center of the wedge (Table 5.2; Fig. 5.3). ANOVA test indicated a statistical difference in average D-excess between the four cores with post-hoc Tukey showing that depths 17 and 36 cm , and 36 and 60 cm were statistically different (Table 5.3).

5.3. Mokka Fjord Slump (55-58 m)

At Mokka Fjord slump, three IWs were sampled (MF-W1, MF-W2, and MF-W3) from the surface to 30 cm depth at their center and edges and all three wedges had similar geochemical composition. The concentration of major cations averaged 18.3±16.8 mgL^{-1}, 9.2±12.0 mgL^{-1}, 32.5±35.3 mgL^{-1} for Ca, Mg, Na, respectively; major anions averaged 55.6±79.6 mgL^{-1}, 50.4±68.7 mgL^{-1} for Cl and SO_4, respectively. The DOC averaged 8.4±15.1 mgL^{-1} and with $\delta^{13}C_{DOC}$ averaging –25.9±0.5‰. Comparison with ionic composition of snow and active layer samples were

made from the Cl normalized data. The IWs have similar Ca/Cl (0.43±0.30), Mg/Cl (0.24±0.06), Na/Cl (1.07±0.31), SO_4/Cl (0.50±0.31) and DOC/Cl (0.46±0.19) values to that of snow. With the exception of Na/Cl and SO_4/Cl in all three IWs and Ca/Cl in MF1-W1, all other molar ratios in the active layer were significantly greater than all the IWs. Three IWs were analyzed for $^{14}C_{DOC}$, the ages ranged from 7.9 to 2.5 cal kyr BP and the $^{14}C_{DOC}$ age was younger in the center relative to the edges.

The IWs from Mokka Fjord were not sampled for high-resolution δD-$\delta^{18}O$ analysis due to the height of slump headwall.

5.4. Dump Slump (33-36 m)

At Dump slump, one IW was sampled (EU19-W1) from the surface to 30 cm depth at its center and edges. The concentration of major cations averaged 17.5±3.4 mgL^{-1}, 7.7±2.3 mgL^{-1}, 55.2±19.8 mgL^{-1} for Ca, Mg, Na, respectively; major anions averaged 44.6±22.2 mgL^{-1}, 77.6±31.6 mgL^{-1} for Cl and SO_4, respectively. The DOC averaged 1.0±0.8 mgL^{-1} and with $\delta^{13}C_{DOC}$ averaging –25.7±1.2‰. Comparison with ionic composition of snow and active layer samples were made from the Cl normalized data. The IW has similar Ca/Cl (0.52±0.47), Mg/Cl (0.38±0.40), Na/Cl (2.21±0.94), SO_4/Cl (0.93±0.77) and DOC/Cl (0.11±0.05) values to that of snow; with the exception of SO_4/Cl, the molar ratios in the active layer were slightly higher than the IW. The $^{14}C_{DOC}$ range from 28.9 to 12.1 cal kyr BP and the age in the centre was older relative to the edges.

Horizontal cores were obtained at 29 and 59 cm depths within IW EU18-W2 for high-resolution analysis of δD-$\delta^{18}O$. The $\delta^{18}O$ values in the two cores ranged from –31.8 to –30.8‰ and only 29 cm depth showed symmetry around the center of the wedge. The average $\delta^{18}O$ in the two cores remained constant with depth and an ANOVA test indicated no statistical difference. The slope between δD-$\delta^{18}O$ is 3.7 and 4.5 for depths 29 and 59 cm , respectively, which is lower than the LMWL. The D-excess values range from 0.6‰ to 5.8‰ and both depths showed symmetry around the center of the wedge. The average D-excess in the two cores was statistically similar with depth.

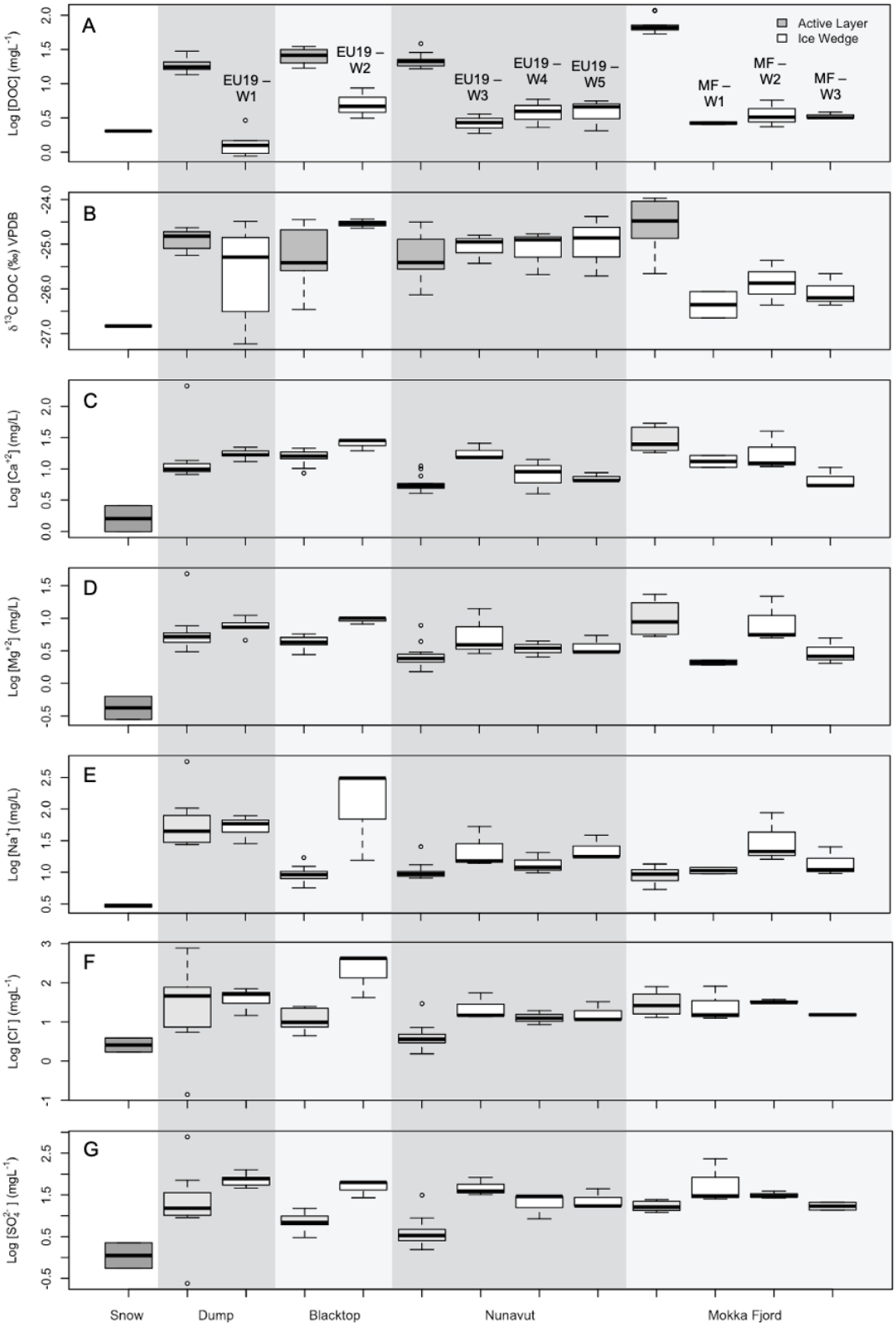

Figure 5.1. Box and whisker plots for snow (dark grey; left), active layer (light grey) and vertical ice core samples (white). Individual slumps (vertical shading) are organized by elevation. Plots are labelled as follows: (A) log transformed dissolved organic carbon (DOC; mgL^{-1}); (B) $\delta^{13}C$ (‰ VPDB); (C) log transformed Ca^{2+} (mgL^{-1}); (D) log transformed Mg^{2+} (mgL^{-1}); (E) log transformed Na^{+} (mgL^{-1}); (F) log transformed Cl^{-} (mgL^{-1}) and; (G) log transformed SO_4^{2-} (mgL^{-1}).

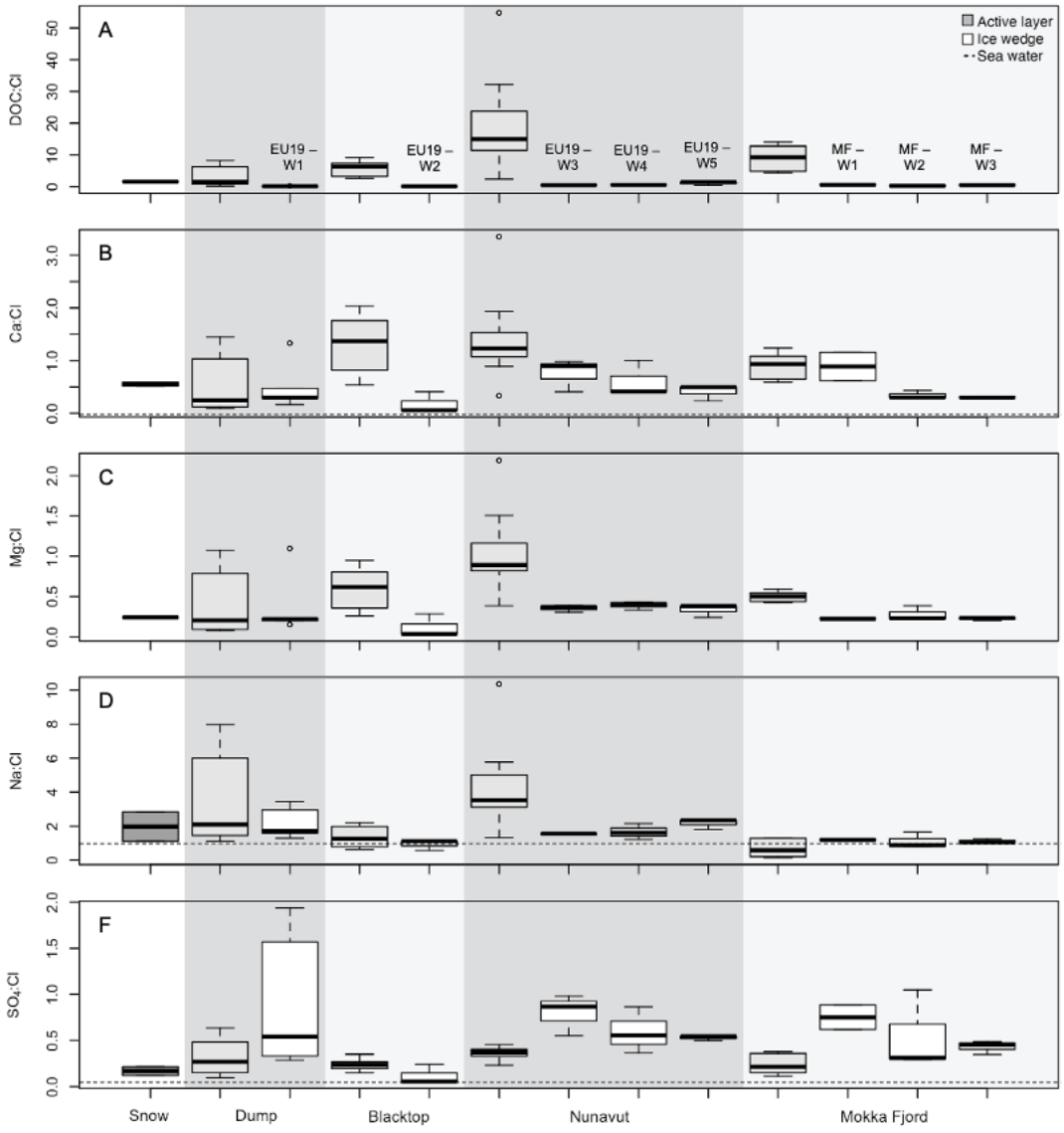

Figure 5.2. Box and whisker plots of molar ratios for snow (dark grey; left), active layer (light grey) and vertical ice core samples (white). Individual slumps (vertical shading) are organized by elevation. Plots are labelled as follows: (A) DOC/Cl; (B) Ca/Cl; (C) Mg/Cl; (D) Na/Cl and; (E) SO_4/Cl.

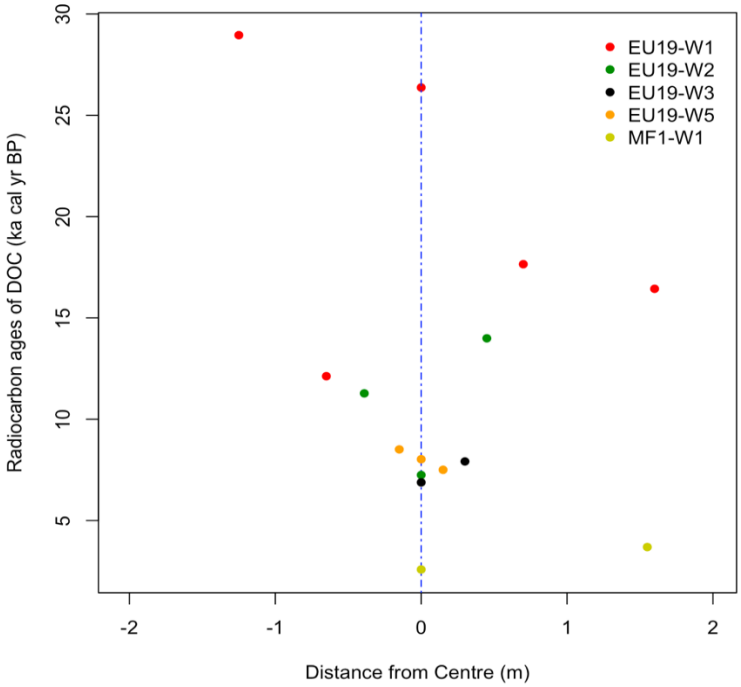

Figure 5.3. Radiocarbon ages of dissolved organic carbon (DOC) obtained from five ice wedges in the Eureka Sound Lowlands. Ice wedges were sampled from Dump Slump (EU19-W1), Blacktop Slump (EU19-W2), Nunavut Slump (EU19-W3 & EU19-W5) and Mokka Fjord Slump (MF-W1) July 2019.

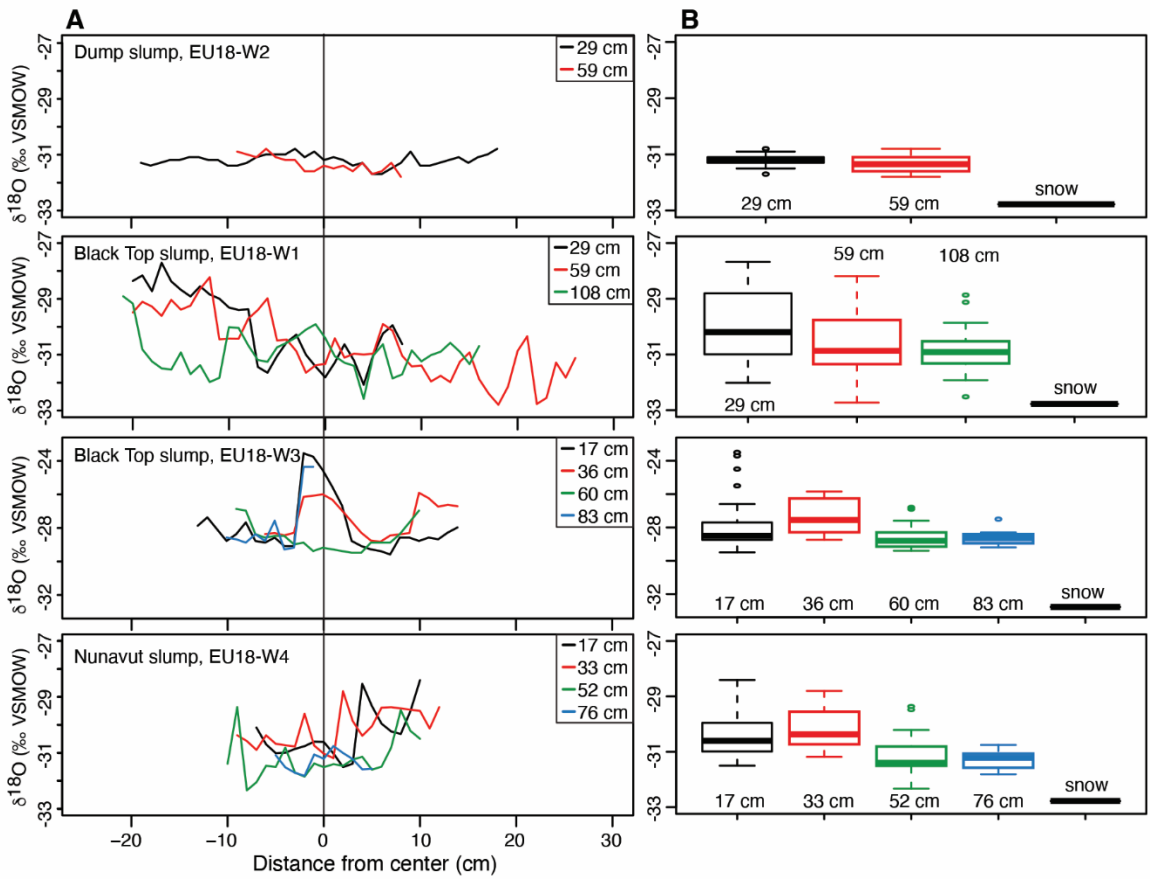

Figure 5.4. $\delta^{18}O$ values in horizontal cores obtained at four sites in the Eureka Sound Lowlands. (A) $\delta^{18}O$ variations at different depths across the ice wedge. (B) Box and whisker plots showing $\delta^{18}O$ variation at depth. Centre bar represents the median, the box represents the first and third quartiles, the whiskers represent the minimum and maximum extents of the data and outliers are represented by a dot.

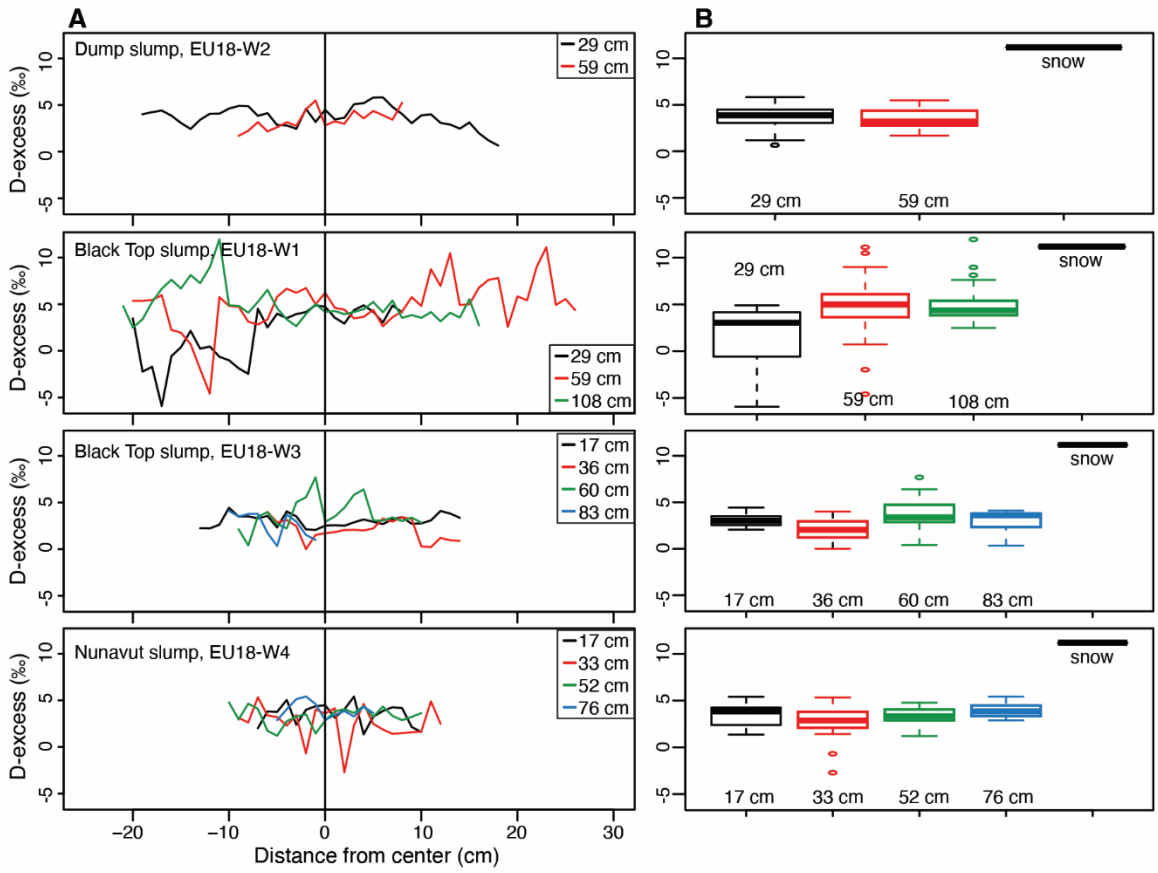

Figure 5.5. D-excess values in horizontal cores obtained at four sites in the Eureka Sound Lowlands. (A) D-excess variations at different depths across the ice wedge. (B) Box and whisker plots showing D-excess variation at depth. Centre bar represents the median, the box represents first and third quartiles, the whiskers represent the minimum and maximum extents of the data and outliers are represented by a dot.

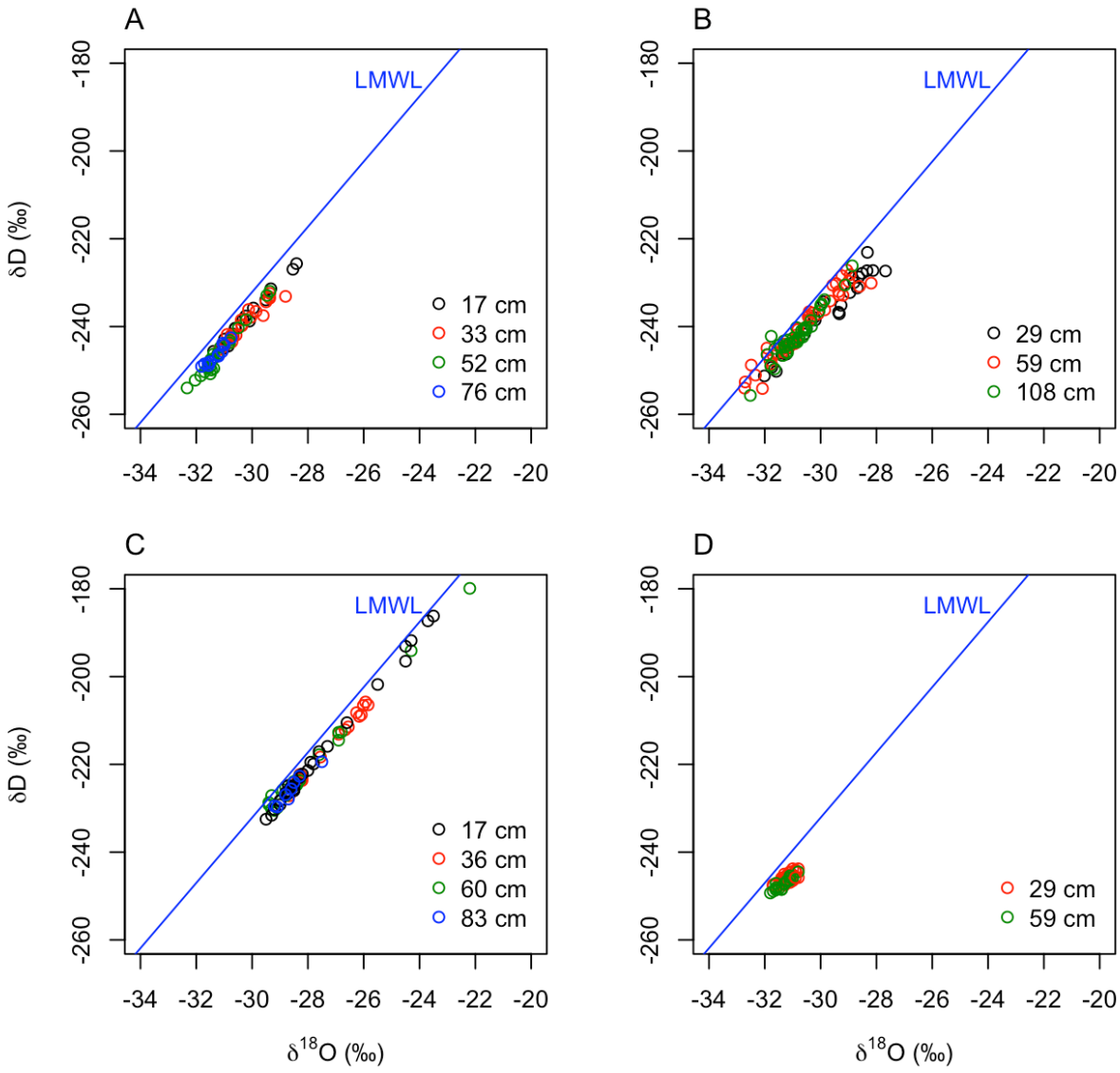

Figure 5.6. δD-δ^{18}O scatterplots of ice wedges sampled from four sites in the Eureka Sound Lowlands. (A) Nunavut Slump (EU18-W4); (B) Blacktop Slump (EU18-W1); (C) Blacktop Slump (EU18-W3); (D) Dump Slump (EU18-W2). The local meteoric water line (LMWL) for Eureka, Nunavut (GNIP, 2005) is shown for comparison.

Table 5.1. Dissolved organic carbon (DOC), carbon-13 isotope ($\delta^{13}C_{DOC}$) and radiocarbon date ($^{14}C_{DOC}$) results of ice wedges sampled at four sites in Eureka Sound Lowlands.

Wedge #	Lab-ID	Distance from centre (m)	DOC (ppm)	$\delta^{13}C_{DOC}$ (‰)	^{14}C yr BP	(±2σ)	$F^{14}C$	(±2σ)	median cal BP
Dump Slump									
EU19-W1	UOC-11064	0	0.96	-24.5	22146	163	0.0635	0.0013	26370
	UOC-11065	1.6	1.26	-25.3	13636	69	0.1832	0.0016	16437
	UOC-11066	-1.25	2.92	-26.5	24872	367	0.0452	0.0021	28954
	UOC-11067	0.7	1.48	-24.8	14480	109	0.1649	0.0022	17651
	UOC-11068	-0.65	0.88	-27.2	10308	75	0.2772	0.0026	12125
Blacktop Slump									
EU19-W2	UOC-12524	-0.39	4.67	-24.4	9883	45	0.2922	0.0017	11278
	UOC-12525	0	3.13	-24.6	6320	36	0.4553	0.002	7250
	UOC-12526	0.45	8.68	-24.5	12127	61	0.221	0.0017	13994
Nunavut Slump									
EU19-W3	UOC-11070	0	1.88	-25.4	6038	41	0.4716	0.0024	6885
	UOC-12527	0.3	2.71	-24.9	7088	39	0.4138	0.002	7919
EU19-W4	UOC-12528	-2.04	2.30	-25.7	7288	39	0.4036	0.002	8100
	UOC-11071	1.68	3.94	-24.8	6251	42	0.4593	0.0024	7190
EU19-W5	UOC-12529	0.15	2.06	-25.7	6614	36	0.439	0.002	7506
	UOC-12530	-0.15	5.61	-24.4	7739	35	0.3816	0.0016	8514
	UOC-11072	0	4.59	-24.8	7222	37	0.407	0.0019	8028
Mokka Fjord Slump									
MF1-W1	UOC-12531	0	2.56	-26.1	2503	33	0.7323	0.003	2587
	UOC-11073	1.55	2.78	-26.6	3438	35	0.6518	0.0028	3694
	UOC-12532	-1	48.66	-24.9	6061	48	0.4703	0.0028	6917
MF1-W2	UOC-12533	0	3.25	-25.4	4347	44	0.5821	0.0032	4921
MF1-W3	UOC-12534	1.5	3.20	-26.2	5941	36	0.4773	0.0022	6765
	UOC-12535	-1.5	3.86	-25.7	7077	58	0.4144	0.003	7900

Table 5.2. Comparison of the average $\delta^{18}O$ and D-excess composition around the center of ice wedges sampled at four sites in the Eureka Sound Lowlands. Results from a two-tailed t-test with unequal variance, values are in bold where the mean values for the right and left sides are significantly different from each other ($p<0.05$). L and R represent left and right section around the center of the wedge.

	$\delta^{18}O$ (‰) L	**$\delta^{18}O$ (‰) R**	**T-test ($\delta^{18}O$)**	**D-excess (‰) L**	**D-excess (‰) R**	**T-test (D-excess)**
Dump slump, EU18-W2						
Core 2 – 29 cm	-31.3±0.2	-31.1±0.1	0.109	3.6±1.4	3.8±0.8	0.585
Core 3 – 59 cm	-31.5±0.2	-31.2±0.2	**0.004**	3.9±0.7	3.1±1.2	0.119
Blacktop slump, EU18-W1						
Core 1 – 29 cm	-29.5±1.2	-30.8±0.6	**0.001**	0.9±2.9	4.0±0.7	**<0.001**
Core 2 – 59 cm	-29.8±0.9	-31.3±0.8	**<0.001**	3.8±2.9	5.7±2.2	**0.020**
Core 3 – 108 cm	-30.7±0.8	-31.1±0.5	0.060	5.6±2.3	4.1±0.7	**0.009**
Blacktop slump, EU18-W3						
Core 1 – 17 cm	-27.6±1.8	-28.3±1.1	0.222	3.0±0.8	3.1±0.5	0.841
Core 2 – 36 cm	-27.8±0.9	-27.4±1.0	0.764	2.3±1.5	1.9±1.1	0.519
Core 3 – 60 cm	-28.3±0.8	-28.7±0.8	0.298	3.7±2.1	3.9±1.3	0.806
Core 4 – 83 cm	-28.6±0.5	-	-	3.0±1.3	-	-
Nunavut slump, EU18-W4						
Core 1 – 17 cm	-30.7±0.3	-30.0±1.1	0.084	3.6±1.1	3.3±1.3	0.607
Core 2 – 33 cm	-30.5±0.4	-29.2±1.6	**0.015**	3.0±1.6	0.7±4.3	0.112
Core 3 – 52 cm	-31.4±0.8	-30.9±0.7	0.199	3.0±1.3	3.7±0.5	0.180
Core 4 – 76 cm	-31.4±0.3	-31.2±0.3	0.381	4.4±1.0	3.7±0.4	0.203

Table 5.3. Summary statistics of $\delta^{18}O$ and D-excess for EU18-W2, Dump Slump. ANOVA and Tukey's HSD statistical difference test results are included and compare data between ice cores, no significant difference found.

	Parameter	$\delta^{18}O$ (‰)	D-excess (‰)
29 cm (Core 2)	n	38	
	Mean	-31.2	3.7
	Median	-31.2	3.9
	SD	0.2	1.1
59 cm (Core 3)	n	18	
	Mean	-31.3	3.4
	Median	-31.4	3.2
	SD	0.3	1.1
ANOVA	F	3.735	0.687
	p	0.059	0.411
	MS	0.20959	0.8511
Tukey's HSD	1 vs 2	0.059	0.411

Table 5.4. Summary statistics of $\delta^{18}O$ and D-excess for EU18-W1, Black Slump. ANOVA and Tukey's HSD statistical difference test results are included and compare data between ice cores, significant difference is in bold.

	Parameter	$\delta^{18}O$ (‰)	D-excess (‰)
29 cm (Core 1)	n	29	
	Mean	-29.9	1.9
	Median	-30.2	3.0
	SD	1.3	2.9
59 cm (Core 2)	n	47	
	Mean	-30.7	4.9
	Median	-30.9	5.0
	SD	1.1	2.7
108 cm (Core 3)	n	38	
	Mean	-30.9	5.0
	Median	-30.9	4.4
	SD	0.7	1.9
ANOVA	F	6.903	15.72
	p	**0.001**	**<0.001**
	MS	7.718	100.42
Tukey's HSD	1 vs 2	**0.012**	**<0.001**
	1 vs 3	**0.001**	**<0.001**
	2 vs 3	0.640	0.995

Table 5.5. Summary statistics of $\delta^{18}O$ and D-excess for EU18-W3, Blacktop Slump. ANOVA and Tukey's HSD statistical difference test results are included and compare data between ice cores, significant difference is in bold.

	Parameter	$\delta^{18}O$ (‰)	D-excess (‰)
17 cm (Core 1)	n	28	
	Mean	-27.9	3.0
	Median	-28.5	3.0
	SD	1.6	0.6
36 cm (Core 2)	n	21	
	Mean	-27.3	2.0
	Median	-27.6	2.1
	SD	1.1	1.1
60 cm (Core 3)	n	20	
	Mean	-28.5	3.8
	Median	-28.8	3.4
	SD	0.8	1.7
83 cm (Core 4)	n	10	
	Mean	-27.7	2.6
	Median	-28.6	3.2
	SD	1.9	1.4
ANOVA	F	2.477	7.588
	p	0.068	**<0.001**
	MS	4.595	10.759
Tukey's HSD	1 vs 2	0.559	**0.019**
	1 vs 3	0.390	0.185
	2 vs 3	**0.042**	**<0.001**
	1 vs 4	0.994	0.797
	2 vs 4	0.883	0.519
	3 vs 4	0.473	0.084

Table 5.6. Summary statistics of $\delta^{18}O$ and D-excess for EU18-W4, Nunavut Slump. ANOVA and Tukey's HSD statistical difference test results are included and compare data between ice cores, significant difference is in bold.

	Parameter	$\delta^{18}O$ (‰)	D-excess (‰)
17 cm (Core 1)	n	18	
	Mean	-30.3	3.5
	Median	-30.6	3.8
	SD	0.9	1.2
33 cm (Core 2)	n	20	
	Mean	-30.2	2.7
	Median	-30.4	2.9
	SD	0.7	1.9
52 cm (Core 3)	n	21	
	Mean	-31.2	3.3
	Median	-31.4	3.3
	SD	0.8	1.0
76 cm (Core 4)	n	11	
	Mean	-31.3	4.0
	Median	-31.2	3.9
	SD	0.3	0.9
ANOVA	F	10.66	2.522
	p	**<0.001**	0.065
	MS	5.546	4.421
Tukey's HSD	1 vs 2	0.941	0.226
	1 vs 3	**0.003**	0.973
	2 vs 3	**<0.001**	0.407
	1 vs 4	**0.003**	0.811
	2 vs 4	**<0.001**	0.058
	3 vs 4	0.949	0.576

Chapter 6: Discussion

6.1. Ice Wedge Biogeochemistry, Age and Activity

6.1.1. Source of Dissolved Organic Carbon and Solutes in the Ice wedges

The approach behind ice wedge dating ($^{14}C_{DOC}$) assumes that the age of the snow meltwater is "modern" at the time it infiltrates the crack. The source of dissolved organic carbon (DOC) in the ice wedges must therefore be assessed before the $^{14}C_{DOC}$ measurements can be used with confidence to infer ice wedge (IW) activity in the Eureka Sound Lowlands (ESL). Once a crack forms in winter, ice wedges can be infilled by one or more of three possible sources: (1) snow, (2) hoarfrost accretion and (3) snow meltwater (Boereboom, Samyn, Meyer, & Tison, 2013; H. M. French & Guglielmin, 2000; Lauriol et al., 1995; Mackay, 1992; Shumskii, 1964; M. St-Jean et al., 2011). The snow meltwater infiltrating the crack is assumed to have modern DOC at the time of infiltration, either because the DOC in the snow is modern, or because when the surface vegetation is thawing, the meltwater can leach the active surface organics thus providing DOC with $F^{14}C \sim 1$ to the meltwater. For example, Grinter et al. (2019) showed that the [DOC] of snow meltwater in central Yukon had similar values to those measured during spring freshets in the Ogilvie River and both had modern $^{14}C_{DOC}$ ages.

The [DOC] of the ice wedges sampled from the ESL averaged 5.1 ± 9.1 mgL^{-1} (0.88 to 48.7 mgL^{-1}; Fig. 5.1 A). This average DOC concentration is higher than the single snow sample (2.1 mgL^{-1}) but much lower than the average of the leached active layer samples (39.5±32.2 mgL^{-1}). The DOC concentration in the ice wedges is within the range of that measured in ice wedges in the western Arctic: ice wedges on Hershel Island (YT) had average DOC concentration of 8.0 mg L^{-1} (2.4 to 8.8 mg L^{-1}; Tanski et al., 2016), those in central YT had average DOC of 12 mg L^{-1} (8.1 to 16.3 mg L^{-1}; Grinter et al., 2019), and those in Alaska and Siberia had DOC average of 9.6 mg L^{-1} (1.6 to 28.6 mg L^{-1}; Fritz et al., 2015). The DOC/Cl can be used to assess the source of DOC to the ice wedges. The ice wedges have a DOC/Cl ratio (0.4±0.4) which is near that of the snow sample (1.5), whereas the DOC/Cl ratio in the leached active layer was significantly higher (12.2± 34.5; with the exception of EU19-W1). This suggests that the source of DOC in the ice wedges is from the snowmelt and not the leached active layer that may release older organics. The $\delta^{13}C_{DOC}$ cannot distinguish between the source of DOC in the ice wedges (-25.4±0.8‰) as it is within the range of both leached active layer samples (-24.9±0.6‰) and the snow sample (-26.8‰).

The molar ratio of major ions (Ca, Mg, Na, and SO_4) also supports the hypothesis that snow meltwater is the main source of solutes to the ice wedges. Snowpack studies on the Fosheim Peninsula and Axel Heiberg Island found that snowmelt chemistry closely resembled that of the snowpack (Thompson & Woo, 2009) and that the initial snowpack is dominated by Ca and Mg (Buttle & Fraser, 1992). The Ca/Cl, Mg/Cl, Na/Cl in the ice wedges are similar to the snow sample and lower than the active layer, and in some cases, the IWs are significantly lower. However, the ice wedges at Mokka Fjord have higher Na/Cl ratios than in the active layer. The majority of the IW samples have a Na/Cl ratio close to that at sea level (1.166; De Caritat et al., 2005). The SO_4/Cl ratio in most of the ice wedges (exception is EU19-W2) is higher than both snow and active layer samples. Overall, the molar ratios of major ions

(Ca/Cl, Mg/Cl, Na/Cl) are like the DOC/Cl more similar to snow than leached active layer, suggesting that the ice wedges are infilled mainly by snow meltwater with minor contribution from leached surface organics. This finding is congruent with Buttle and Fraser (1992) which used similar molar ratios and found that snowmelt runoff became enriched with Ca, Mg, and Na as meltwater came into contact with the soil. The difference in SO_4/Cl in the ice wedges versus the snow and active layer samples is likely due to a strong marine presence when these ice wedges were forming (I. Clark, 2015).

6.1.2. Epigenetic Ice Wedge: Width, Cracking Probability and Age

Epigenetic ice wedges, such as those sampled in the ESL, develop in pre-existing permafrost and grow progressively wider (Mackay, 1990). As a result, epigenetic ice wedges should display a positive relation between their width and length of period of growth (i.e., wider wedges show a larger age range; Fig. 6.1). Unlike glaciers where one can count the layering and validate the chronological ages such as known volcanic eruptions or ^{14}C of occluded CO_2, the same cannot be done with individual veins forming ice wedges as they do not crack annually. However, based on measurements from Garry Island (Mackenzie Delta, NWT), Mackay (1974) suggested that the cracking probability of an ice wedge is dependent on the width of an ice wedge, with a medium-size ice wedge having a higher cracking probability. Narrow (<1m) and large (>2m) ice wedges have lower cracking probabilities due to competing cracking and a reduction of thermal stress caused by the insolating effect of a thicker snow cover in wider troughs, respectively. With knowledge of the average width of ice wedges (or troughs) in a region and its standard deviation, one can develop a cracking probability curve, and then, assuming a growth increment (typically 2-3mm) the age range of an ice wedge can be established as a function of its width. Therefore, given that the cracking probability of ice wedges varies as a function of its width, the age of an ice wedge will also be dependant of its cracking probability.

In the ESL, Couture and Pollard (1998) measured more than 100 tundra polygon and the widths averaged 1.46 ± 0.56 m. Based on these measurements, a cracking probability curve was established for ice wedges in the ESL and the estimated age curve was then established using three possible growth increments (2, 2.5 and 3 mm), which are within the range of that reported by Lewkowicz (1994) from tritium measurements in reactivated ice wedges. The width and $^{14}C_{DOC}$ age range of the sampled ice wedges in the ESL show a good fit with the theoretical age distribution curve as a function of ice wedge width using the 2.5 to 3 mm growth increment (Fig. 6.1), especially considering the sensitivity of the age curve to the cracking probability (a much better fit is obtained using an average width of 1.36 m instead of 1.46 m). To test if the use of $^{14}C_{DOC}$ age range in ice wedges is applicable to other regions, the $^{14}C_{DOC}$ dataset of Holland et al. (2020) of ice wedges in the Tuktoyaktuk Coastlands was used. Measurements of ice wedge width (or trough) were not provided in that study, thus the values reported by Mackay (1974) from the nearby Garry Island (1.1 ± 0.7 m) was used to produce the cracking probability curve. Although the width and $^{14}C_{DOC}$ age range of only four ice wedges were reported by Holland et al. (2020), the fit with the theoretical age distribution curve is good using the 2 mm growth increment (Fig. 6.1). The good fit between the width of ice wedges and $^{14}C_{DOC}$ age range appears to validate the cracking probability concept of Mackay (1974) and suggests that the widening rate of ice wedges is not linear.

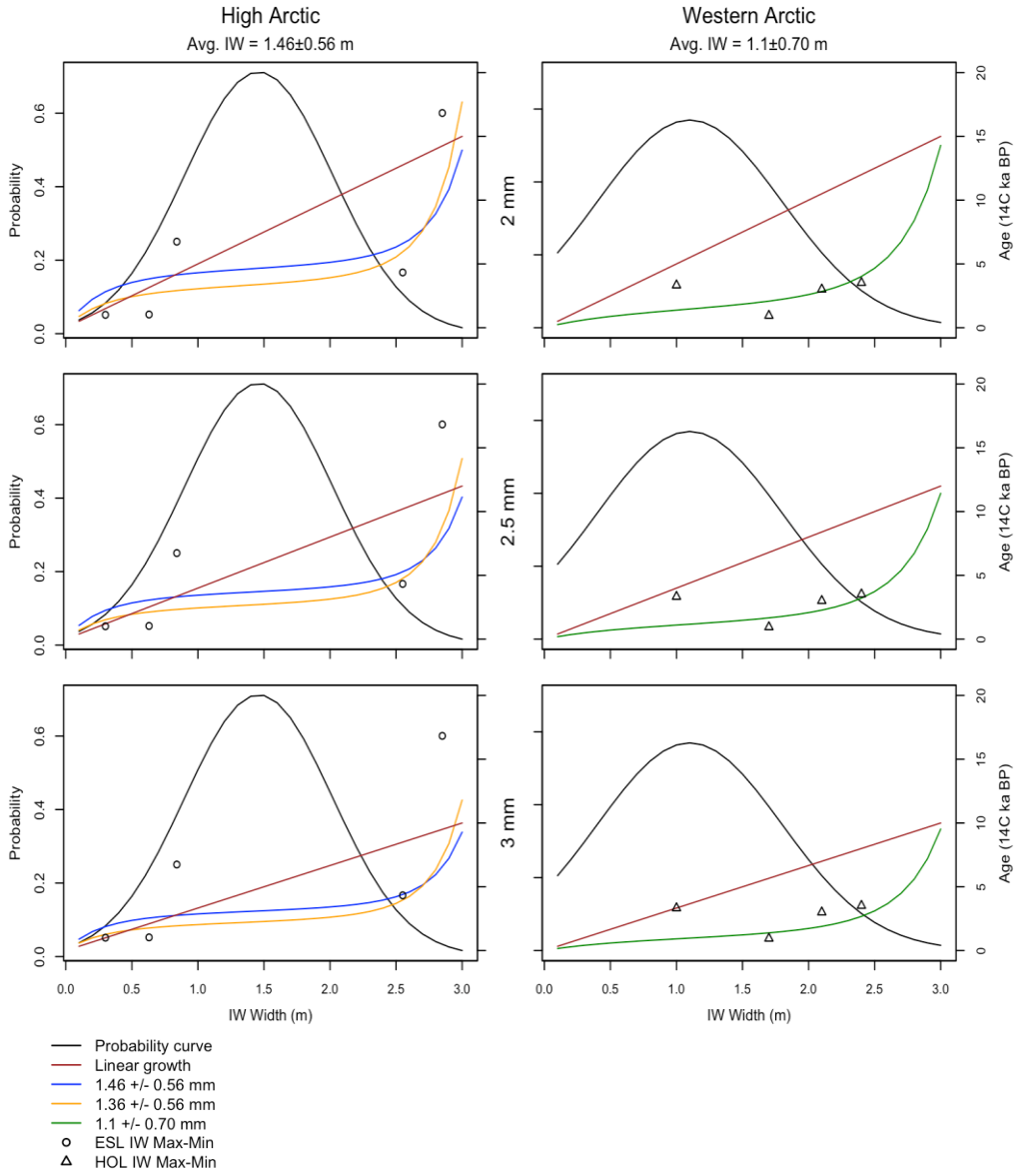

Figure 6.1. Ice wedge cracking probability (black line) based on the width of the ice wedge for the high and western Canadian Arctic. With Mackay (1974) growth curve for three average IW widths (blue – 1.46 ± 0.56 mm, orange – 1.36 ± 0.56 mm and green – 1.1 ± 0.70 mm) for three growth increments (2mm, 2.5 mm and 3mm), linear growth curve (red) shown for comparison. Ice wedge data from the Eureka Sound Lowlands appears as circles in the high Arctic and Fort McPherson IW data (Holland et al., 2020) as triangles in the western Arctic.

6.1.3. Ice Wedge Activity in the Eureka Sound Lowlands

In the previous two sections, it was demonstrated that the DOC is mostly sourced from snow meltwater infiltrating the ice wedge and the $^{14}C_{DOC}$ age fits nicely with the theoretical age distribution curve. In this section, the ice wedge activity in the ESL is established with the $^{14}C_{DOC}$ ages first being compared with marine regression curves, a proxy of initial timing of permafrost aggradation and ice wedge growth in the area, and then the $^{14}C_{DOC}$ age distribution are compared with regional Holocene paleo-climate reconstructions.

During the Pleistocene, the Fosheim Peninsula and surrounding area was glaciated by the Innuitian Ice Sheet with deglaciation occurring between 10.3 - 8.7 kyr BP (Blake Jr., 1970; A S Dyke et al., 2002; J England et al., 2006; Hodgson, 1985; Huges et al., 1977; Simon et al., 2015). Marine transgression in the ESL occurred until 8.8 – 7.8 kyr BP with the Holocene marine limit near the Eureka Weather Station reaching 146 m a.s.l. (Bell, 1996). The post-glacial isostatic rebound around Eureka was high between 10 - 8 kyr BP, and nearly complete by 2.5 kyr BP (Simon et al., 2015). After marine regression, permafrost was able to aggrade in the marine sediments, allowing ice wedges to develop. The $^{14}C_{DOC}$ ages obtained from ice wedges across a range of elevations in the ESL, including 11 additional $^{14}C_{DOC}$ data from two ice wedges at Blacktop slump, two ice wedges at Mokka Fjord, and two ice wedges at Gemini slump (120 m a.s.l.; data from Roy, 2018) are compared with the local marine emergence curves of Hodgson & Nixon (1998) and Bell & Hodgson (2000; Fig. 6.2). The majority of the $^{14}C_{DOC}$ ages of the IWs fall along or above the marine regression curves, that is the case for all ice wedges sampled at Gemini, Nunavut, and Mokka Fjord slumps and one ice wedge sampled at Blacktop slump. This suggests that, at these sites, conditions became suitable for the aggradation of permafrost and subsequent ice wedge development in the marine sediments occurred immediately or shortly after marine regression. This in analogous to contemporary studies that observed the development of ice wedges in recently drained lake beds, for example at Illisarvik drained-lake basin in the Mackenzie Delta that was artificially drained in 1978 (Mackay, 2000) and following the removal of coniferous vegetation in peatlands located in the eastern Canadian Subarctic (Payette et al., 1986).

The $^{14}C_{DOC}$ ages of ice wedges at Blacktop and Dump Slump, situated at 33-36 and 60-66 m a.s.l., respectively, are distributed below the marine regression curves. This was an unexpected finding. There are several possible explanations for this observation: 1) the $^{14}C_{DOC}$ ages are contaminated with old organics; however the marine sediments composing the active layer are Holocene age and thus this is not a possible explanation, even if the marine reservoir effect is considered, which makes material appear older by about 800-1200 years in Arctic Ocean (Dumond & Griffin, 2002; Dyke, 1999); 2) ice wedges were developing in an ice-free region prior to the advance of the ice sheet and were preserved beneath a cold-based ice sheet (i.e., England, 1996). However, this scenario is also not possible since the ice wedges at Dump Slump developed in massive ice $^{14}C_{DOC}$ dated to 15,170 cal yr BP (similar to the age obtained in the ice wedges; Roy, 2018), whereas those at Blacktop Slump developed in Holocene-age colluviated material (i.e., Roy, 2018); or 3) the most likely explanation is that the ice wedges formed from a mixture of late Pleistocene age glacial meltwater and snow meltwater with glacial meltwater, providing the majority of the source water. Support for this hypothesis comes from the $\delta^{18}O$ composition of these ice wedges (-33.6 – -29.1‰, Fig. 6.7),

and the concentration of their DOC and major ions (DOC – 2.70±3.0 mgL^{-1}, Ca – 19.31±5.4 mgL^{-1}, Mg – 8.09±2.3 mgL^{-1}, Na – 97.21±104.4 mgL^{-1}, Cl – 108.3±157.2 mgL^{-1}, SO4 – 75.2±28.9 mgL^{-1}; Fig. 6.9), which are all very similar to late Pleistocene glacial ice (Fisher et al., 1998). The landscape following deglaciation was vastly different from today suggesting that the sampled ice wedges at Blacktop and Dump Slump could have developed shortly after marine regression from late Pleistocene age glacial meltwater originating from the surrounding highlands during retreat of the ice sheet to the south-east (Bell, 1992).

Ice wedges and their $^{14}C_{DOC}$ age distribution, can be used as proxies for paleo-environmental conditions because their development requires: (1) the presence of icy permafrost; (2) mean annual air temperatures <-2°C and mean winter air temperatures <-12°C; (3) surface conditions that allow cracking of the icy permafrost when air temperatures rapidly decrease in winter; and (4) moisture source to fill the cracks (Washburn, 1980; Harry and Gozdzik,1988; Christiansen et al., 2016). Figure 6.3 compares the $^{14}C_{DOC}$ age distribution of IWs in the ESL to various Holocene paleoclimate reconstructions for the high Arctic (summer solstice insolation at 65°N (Laskar et al., 2004), 25-yr mean air temperature (Lecavalier et al., 2017), Agassiz Ice Cap winter temperature $d^{18}O$ record, 20-yr mean (Buizert et al., 2018) and, annual precipitation on Victoria Island (Peros & Gajewski, 2008)). The $^{14}C_{DOC}$ ages, beyond having a degree of analytical uncertainty, represent a range in ages since samples were collected across multiple ice veins such that DOC was incorporated over an unknown period of time; hence $^{14}C_{DOC}$ ages were grouped in 500-yr bins (Fig. 6.3 F). Although data from only 22 $^{14}C_{DOC}$ of Holocene ages from 16 ice wedges is presented, it provides initial insight into periods of ice wedge activity in the ESL.

The distribution of $^{14}C_{DOC}$ ages of ice wedges in the ESL for the Holocene occur immediately or shortly after marine regression (9 ka) and continue up until the late Holocene (2.5 ka; Fig. 6.3 E).The present-day mean annual air temperature is -15°C, and despite the early Holocene being warmer than present-day, temperatures in the ESL were mostly likely always favorable to the growth of ice wedges. Therefore, ice wedge activity in the ESL should reflect changes in snow cover. The presence of thick snow cover may reduce the cracking of the icy permafrost or ice wedges by buffering the strong winter air temperature variations. Mackay (1993) suggested that areas with snow depth >60 cm would greatly reduce cracking events. Alternatively, the presence of thin snow cover may be favorable to induce cracking but may not supply sufficient meltwater to infiltrate and fill the crack for ice wedge growth. A first order estimate of a snow depth threshold to supply sufficient meltwater to fill a crack can be made with knowledge on crack geometry and average width of ice vein. The volume of snow meltwater required to fill a crack in the form of a prism over a 1 m section to a depth of ~ 3 to 3.5 m (crack depth is given by the depth of ice wedge in the ESL; Bernard-Grand'Maison and Pollard, 2018) and ~ 3 mm wide vein (Lewkowicz, 1994) is 4.5 to 5 L. For the average trough width in the ESL (1.46±0.56 m), the required volume of meltwater to fill a crack can be obtained if the snow depth in the trough is c. 30 cm. For troughs that are 1m wide, a snow depth in the trough of 45-50 cm would be required. These calculations assume that the snow meltwater that infiltrate the crack is sourced directly from the trough above the crack and ignore the fact that snow meltwater may also originate from the center of polygons or from nearby hillslopes. However, it does suggest that snow depth <30 cm may not provide sufficient meltwater to fill a crack. Present-day snow depth conditions are near that threshold. Between 1980-2016, the average winter snow depth in Eureka was 14.9

± 6.3 cm and ranged between 5 to 35 cm (Fig. 3.3). Reconstructed Holocene precipitation on Victoria Island suggests that total precipitation was higher than present-day during the early and mid-Holocene, and a switch to near present-day level occurred around 5000 years. Measured peat activity for the ESL shows a majority of activity occurring between 9-2 ka (Fig. 6.3 D; Garneau, 2000). The high level of peat accumulation is attributed to the warmer and wetter climate conditions of the mid-Holocene with accumulation beginning after marine regression and ending in the late Holocene from a decline in precipitation (Garneau, 2000). Therefore, the switch to the drier climate conditions near the start of the late Holocene may correspond to the reduced ice wedge activity that is observed during the late Holocene, although ice wedge activity is occurring in recent times (i.e., Lewkowicz, 1994).

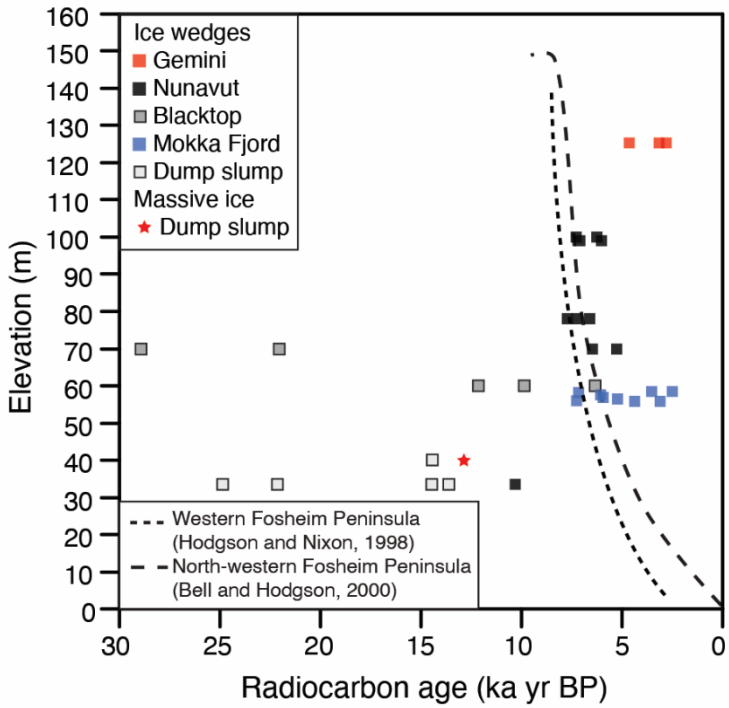

Figure 6.2. Ice wedge activity and elevation (m) compared against marine regression curves created by Hodgson and Nixon (1998) and Bell and Hodgson (2000).

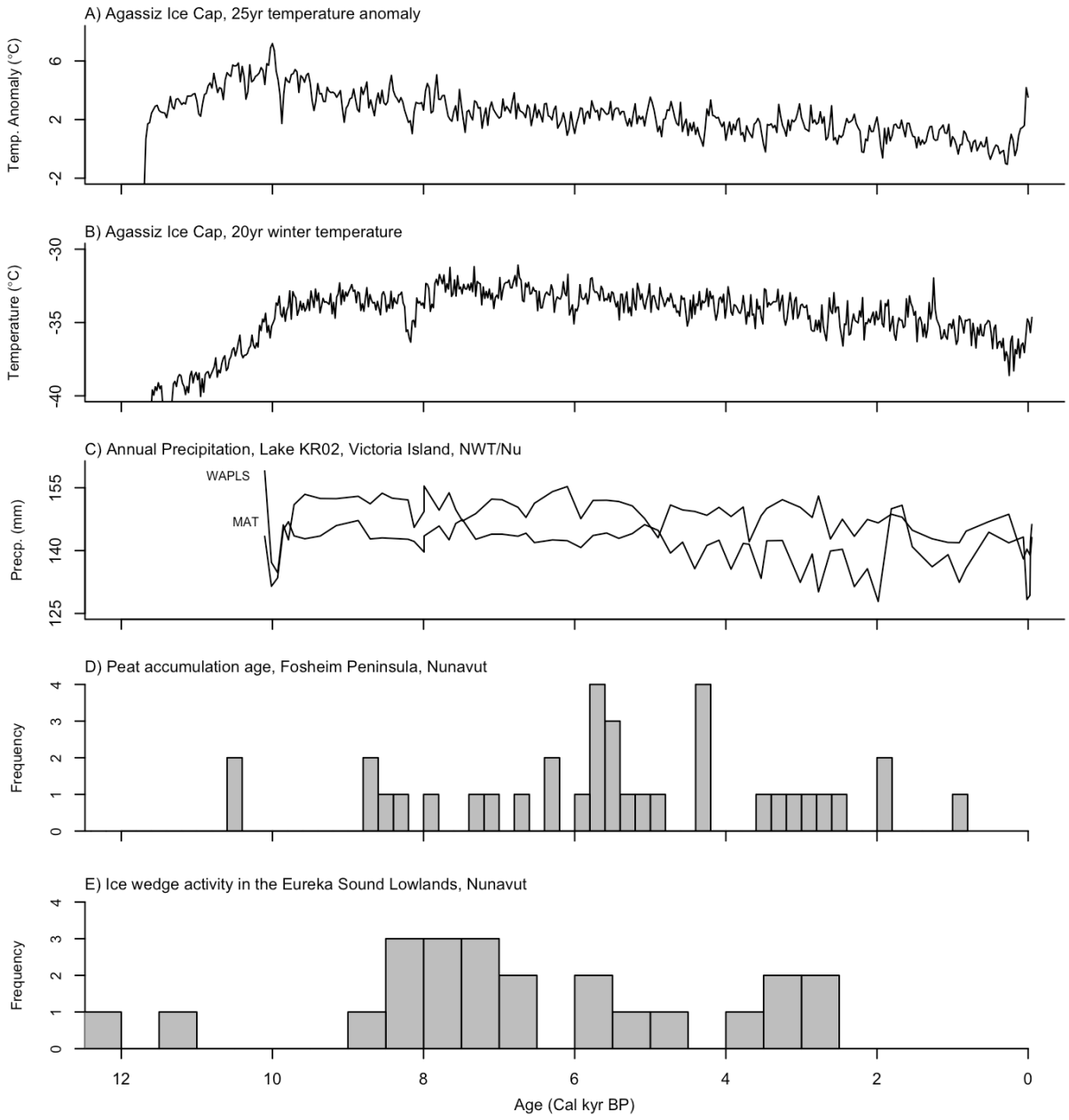

Figure 6.3. Climate and ice wedge activity for the high Arctic for the Holocene. (A) Agassiz Ice Cap temperature anomaly, 25-yr mean (Lecavalier et al., 2017) and (B) Agassiz Ice Cap winter temperature $d^{18}O$ record (Buizert et al., 2018). (C) Annual precipitation for Lake KR02, Victoria Island, NWT/Nu from Peros and Gajewski, 2008. (D) Peat accumulation in the Eureka Sound Lowlands (Garneau, 2000). (E) Eureka Sound Lowlands frequency ice wedge activity.

6.1.4. Ice Wedge Activity in Western Arctic and High Arctic Canada

The reconstruction of Late Quaternary ice wedge activity based on $^{14}C_{DOC}$ measurements is a recent development. To date, only three studies have obtained $^{14}C_{DOC}$ measurements from ice wedges: Grinter et al. (2019) from ice wedges near Two Moose Lake in central Yukon, Holland et al. (2020) for ice wedges in the Tuktoyaktuk Peninsula in NWT and this thesis from the ESL. Fig. 6.4 compares the Holocene IW activity in the western and high Canadian Arctic with solar insolation for summer solstice at 65°N and Holocene temperature reconstructions (Kaufman et al., 2016; Lecavalier et al., 2017). As shown in Figure 6.5, these two regions currently have very different mean winter temperature, and snow depth with the western Arctic being warmer and having thicker snow cover that often exceeds 60 cm, a depth that likely limits cracking to induce ice wedge development (i.e., Mackay, 1994).

The ice wedge activity between the ESL and western Arctic Canada shows a strong contrast. In the western Arctic, ice wedge growth appears to have started during the start of the mid-Holocene with a peak in activity during the late Holocene. The lack of ice wedge growth during the early Holocene was attributed to warmer and wetter climate (I. Clark et al., 2004; Kaufman et al., 2016; Viau & Gajewski, 2009) along with a shift from tundra to boreal forest which are unfavorable conditions to the growth of ice wedges (Grinter et al., 2019). In fact, the early Holocene in western Arctic Canada is a period of increased thermokarst activity. This is evidenced by the formation of thaw lakes, with peak initiation at 10,500–10,000 cal yr BP (G. M. MacDonald et al., 2006) and in increased active layer thickness in Alaska and western Arctic Canada that resulted in the partial ice-wedge degradation (ice wedges truncated at the maximum active layer depth (i.e., Burn, 1997; French and Shur, 2010; Fritz et al., 2016, 2012; Mackay, 1974)). Ice wedges began to develop in the western Arctic Canada during the mid-Holocene due to cooler and drier climates and a shift to tundra vegetation. In contrast, ice wedge growth in the ESL show a peak in activity during the latter part of the early Holocene following deglaciation and marine regression, with minor periods of activity during the mid-Holocene. Considering that temperatures were most likely always favorable to the development of ice wedges, the ice wedge activity in the ESL likely reflects changing snow cover conditions and its effect on ground temperatures and supply of snow meltwater. Overall, the IW activity in western Arctic Canada appears to be influenced by multiple climate variables, winter temperature, snow depth and vegetation; and by contrast in the high Arctic, changes in snow depth appear to be the main factor.

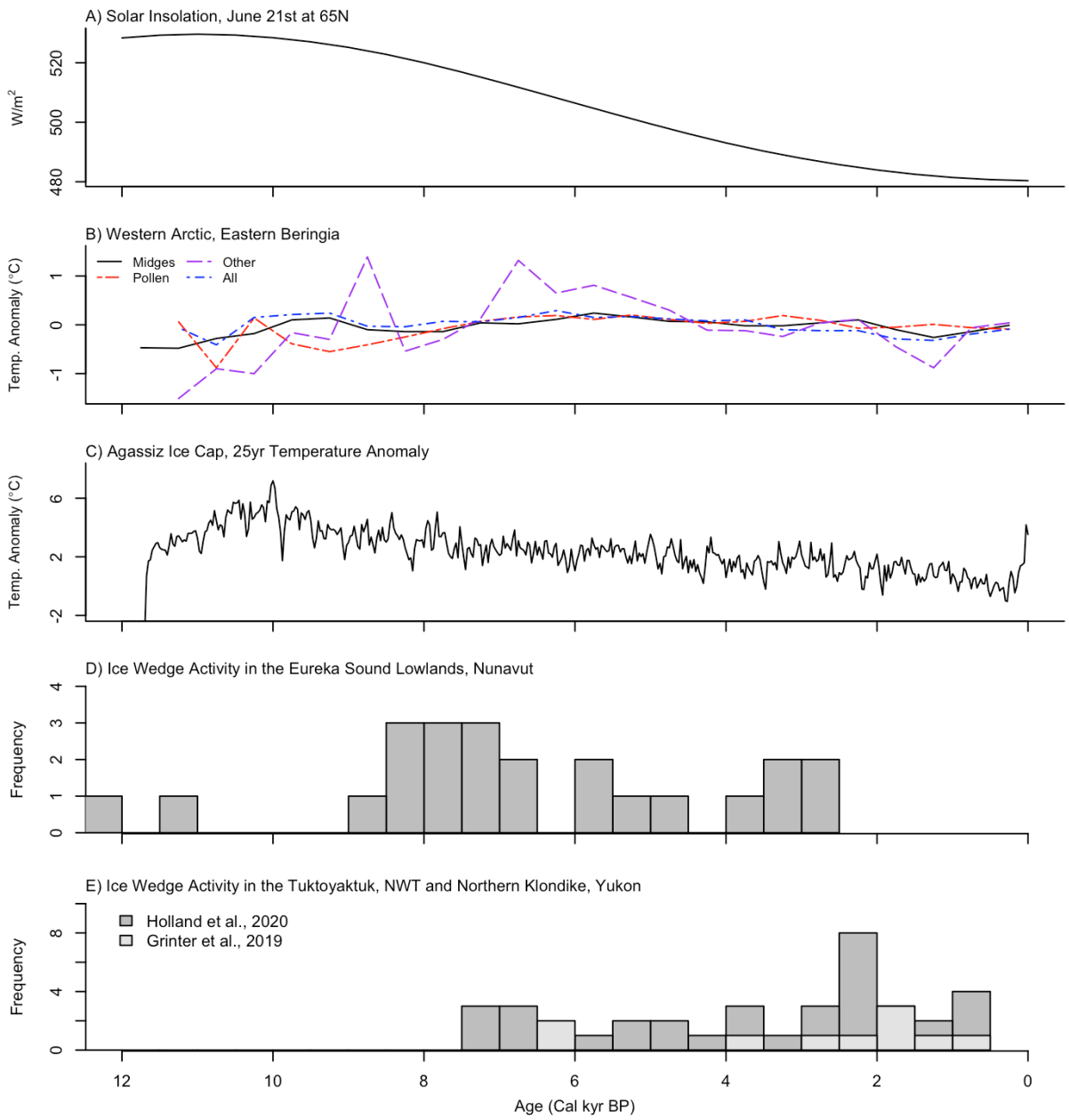

Figure 6.4. Climate and ice wedge activity for the western and high Arctic. (A) Solar insolation curve for June 21st at 65°N from Laskar et al. (2004). (B) Eastern Beringia temperature anomaly reconstruction from Kaufman et al. (2016). (C) High Arctic 25yr temperature anomaly reconstruction from Agassiz ice core from Lecavalier et al. (2017). (D) IW activity in the Eureka Sound Lowlands. (E) Ice wedge activity for Tuktoyaktuk, NWT (Holland et al., 2020) and for the Northern Klondike, Yukon (Grinter et al., 2019).

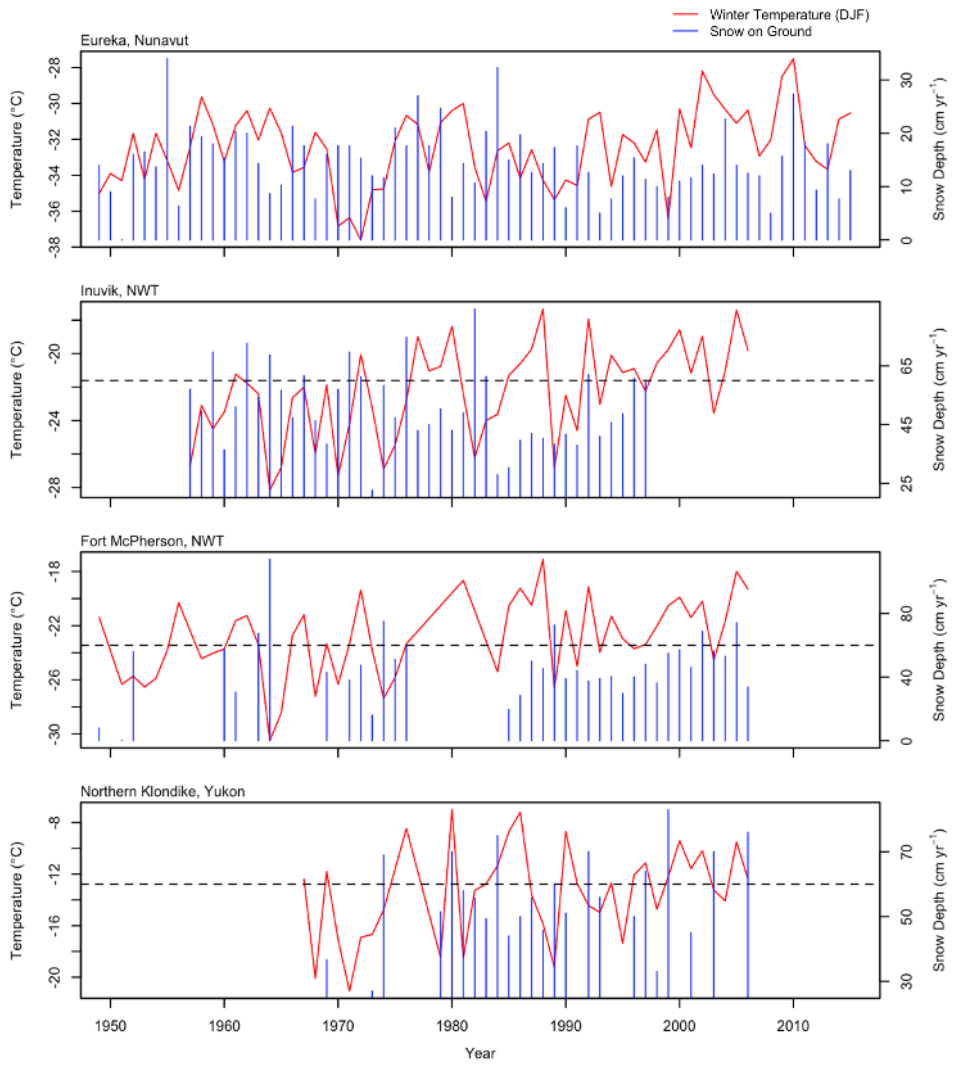

Figure 6.5. Mean winter (DJF) temperature and total snow on ground (cm yr^{-1}) for four Arctic locations (Eureka, Nu; Inuvik, NWT; Fort McPherson, NWT and; Northern Klondike, Yukon) between 1950 – 2015 (Government of Canada, 2020).

6.2. Ice Wedges as Paleo-Temperature Proxies

6.2.1. d-^{18}O Variations within Ice Wedges

The majority of ice wedges sampled in the Eureka Sound Lowlands (ESL) show $^{14}C_{DOC}$ dates that are youngest in the centre (Fig. 5.3); this is an expected result as it is widely hypothesized that ice wedges will crack near the centre of the ice wedge (IW) (Mackay, 1974). However, two IWs (EU19-W1 and EU19-W5) have centre dates that are older than one or more of the sampled edges. Grinter et al. (2019) and Holland et al. (2020) identify similar results in IWs from the western Canadian Arctic. Peripheral cracking appears to be a regular occurrence (Grinter et al., 2019; Holland et al., 2020; Opel et al., 2017). However, no studies have examined the causes behind the phenomenon. Mackay (1974; 1992) determined that IWs outside of the range of intermediate width (0.5-2m) will crack less regularly as a result of competitive cracking, polygon morphology and snow depth. For EU19-W1, the total width is 3.5 m with a variation in age of ~16.8 ka cal BP. Two possible explanations may exist for this variation: 1) the width of the ice wedge affected the location of cracking, however, if this were to occur, MF-W1 (3.3m wide) would also show an older centre sample than the edges, and this is not the case; 2) that the massive ice adjacent to the wedge was also sampled, the wedge is dated from left to right: 28 950 cal yr BP, 12 120 cal yr BP, 26 370 cal yr BP, 17 650 cal yr BP and 16 430 cal yr BP. The two samples extracted from the right side of the wedge have an age close to the massive ice sample (15 170 cal kyr BP), the D-excess for these samples is 6.1‰ and 6.48‰, respectively, similar values were found in massive ice samples obtained from Dump Slump by Roy (2018). The other three of the samples have an average D-excess of 2.93±0.6‰, notably less than the massive ice samples collected by Roy (2018). For EU19-W5, the wedge is 0.4 m wide with an age variation of ~500 years between the centre and both edges, because the samples are so close in age, this discrepancy is likely a result of a sampling error.

Three of the four ice wedges that were horizontally sampled contain a significant difference in either $\delta^{18}O$ and D-excess or both, between the left and right sides of the wedge. This difference is not consistent with depth nor is it consistent between the $\delta^{18}O$ and D-excess datasets. This inconsistently may be attributed to peripheral cracking where the thermal contraction crack occurs on one side of the wedge. Peripheral cracking may be a function of size, EU18-W1 from Blacktop Slump, had the least amount of symmetry in both $\delta^{18}O$ and D-excess, this was the largest of the wedges at 1.6 m wide. EU18-W3, sampled at Blacktop, had the highest degree of symmetry and was only 0.36 m wide. Many researchers suggest the use of smaller wedges for paleoclimate research (i.e. Meyer et al., 2002; Meyer et al., 2010; Michel, 1990; Vasil'chuk & Vasil'chuk, 2014), for this reason. However, peripheral cracking can still occur in small ice wedges. EU18-W4 was 0.36 m wide and contained a significant difference in $\delta^{18}O$ at 33 cm between the left and right sides of the wedge ($p = 0.015$; $\delta^{18}O$). Thus, the use of smaller wedges is not a guarantee that no peripheral cracking occurs.

The difference in $\delta^{18}O$ and D-excess at depth within the horizontally sampled ice wedges is not consistent among the four wedges. Three of the four wedges show a significant difference between one or more depths for the $\delta^{18}O$ and D-excess values. This difference is likely due to the occurrence of ice plugs at the surface of the wedge.

Mackay (1974) showed that the width of an ice wedge crack is relatively uniform with depth (1 cm ± 0.5 cm); and the typical V-shape of an epigenetic ice wedge is probably a result of the preferential formation of ice-plugs near the surface. EU18-W1 took on a V-shape, suggesting the regular occurrence of ice plugging near the IW surface. This, in part, may explain the $\delta^{18}O$ differences at depth in EU18-W1. In contrast, EU18-W3 and EU18-W4 were the smaller IWs sampled and found to be closer to a rectangle in shape, suggesting that little to no ice-plugging occurred during formation. The differences at depth are then likely attributed to Rayleigh-type isotopic fractionation. Where the $\delta^{18}O$ isotope becomes progressively depleted as the amount of residual water decreases, this occurs in closed bodies of water like ice wedges (Michel, 1982). In Fig. 6.6 the $\delta^{18}O$ of the ice wedges is compared against residual water. This was then compared against modelled isotope data using a fractionation factor derived by Suzuoki and Kumura (1973). The modelled data shows a 2‰ depletion in $\delta^{18}O$ with a 50% reduction of available water; the ice wedge data fits this model well. Vertically sampled IWs from Herschel Island show a similar depletion in $\delta^{18}O$ at depth (2‰; Michel, 1990).

In EU18-W2, at Dump Slump, it is assumed that the wedge formed in massive ice (Roy, 2018). The wedge does not vary significantly in $\delta^{18}O$ and D-excess across nor at depth within the wedge. Two possible explanations exist for this lack of variation: 1) this ice sample is not of a wedge but of massive ice, however, if this were the case, the D-^{18}O slope (3.7 and 4.5 for depths 29 and 59 cm) would be similar that found for the massive ice (~7.4; Roy, 2018); 2) is that isotopic fractionation occurred, the mean $\delta^{18}O$ of both depths fit the model (Fig. 6.6) well, and the low slope value (D-^{18}O) indicates that isotopic fractionation is occurred when this ice wedge was formed.

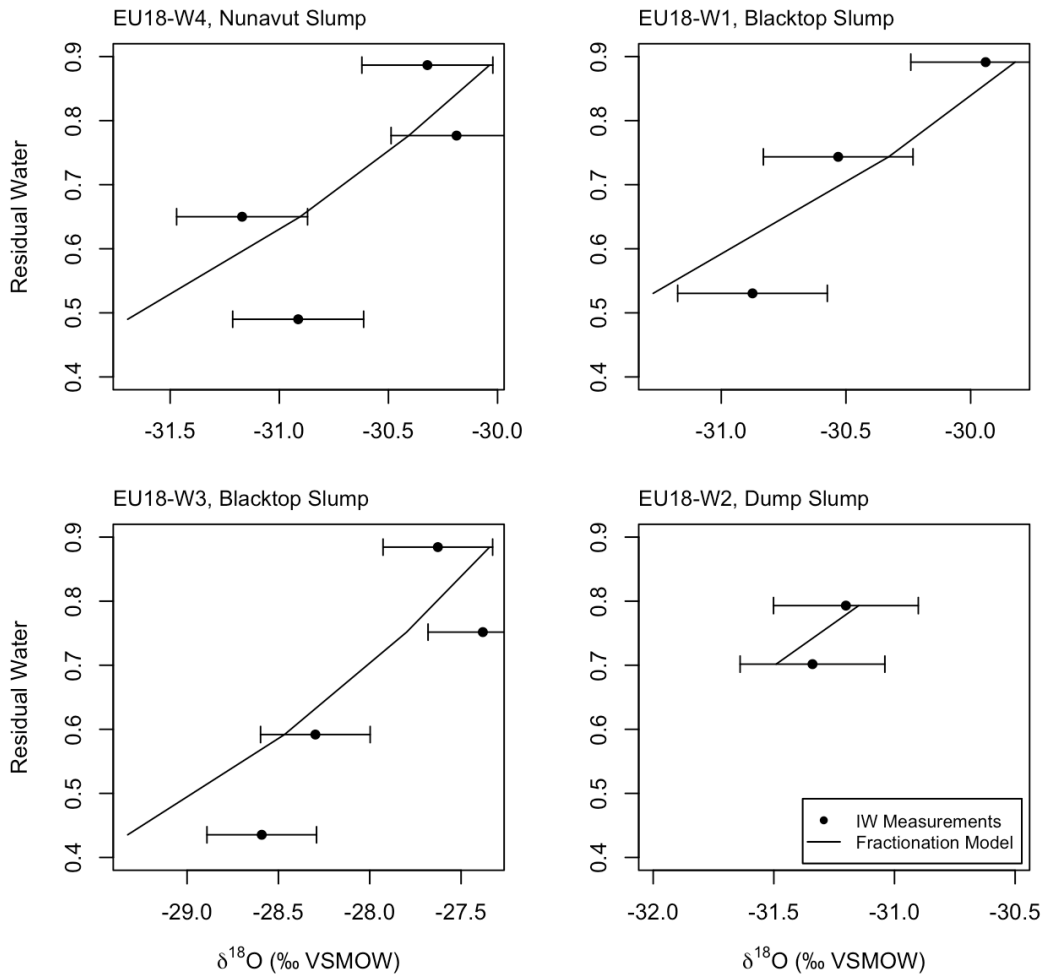

Figure 6.6. Average $\delta^{18}O$ (‰) for each depth in the horizontally sampled ice wedges with an error of ± 0.3‰ (circles), plotted against residual water (*f*), a calculation based on sample depth and total length of IW (*f* = 1 – (sample depth/total ice wedge length)). Ice wedge fractionation model (black line) shown for each wedge, model created using the Rayleigh distillation fractionation equation ($\delta i = \delta_O + \ln(\alpha_{i\text{-}w})^* 1000 * \ln f + \ln(\alpha_{i\text{-}w}) *1000$; Lacelle, 2011) with the fractionation factor ($\alpha_{i\text{-}w}$ (^{18}O) = 1.0028) by Suzuoki and Kumura (1973). Initial $\delta^{18}O$ (δ_O) for each wedge are -32.5‰ (EU18-W4), -32.3‰ (EU18-W1), -29.8‰ (EU18-W3) and -33.3‰ (EU18-W2).

6.2.2. Reconstructing Holocene Winter Temperatures from $\delta^{18}O$ in Ice Wedges

Ice wedge paleoclimate studies rely on the D-^{18}O values of the ice to infer past climate. The D-^{18}O of the IWs is compared against the study region's modern local meteoric water line (LMWL) to confirm no fractionation occurs within the ice wedge. In Fig. 5.6, each of the horizontally sampled ice wedges plots close to the LMWL for the Eureka area (7.4). The slope for each of the sample depths are below the LMWL (avg. 6.3±1.1). In the section above, it is determined that Rayleigh-type isotopic fractionation is occurring within the wedge. It is shown that the D-^{18}O values in an ice wedge can differ at depth and between the two sides of an ice wedge and so are not a reliable source for temperature reconstructions. Moreover, using the LMWL as a standard does not work because it relies on modern snow and rain isotopes, and the IWs sampled are not modern nor are they infilled by rain. Also, with land uplift for example, the isotopes of precipitation will be different (Jasechko et al., 2015; Porter & Opel, 2020).

Instead, this section presents the use of IW stable isotope values for first-order climate inferences. This is done using the $\delta^{18}O$ from the 30 cm deep ice cores. By using the surface cores, it can be inferred that little to no isotopic fractionation occurred within the wedge. In Fig. 6.7 B the stable water isotopes from the Agassiz ice cap show a 3.23‰ (0.37‰ ka^{-1}) decline for the span of the Holocene, the surface ice wedge samples show a similar shift (4.83‰, 0.56‰ ka^{-1}) for the same period. The IW data fits well with the glacial ice core data, however, the stronger shift in the IW $\delta^{18}O$ may be interpreted as a colder climate than what had actually occurred. This is another area where IWs fail as climate proxies. This shift is likely a result of post-depositional snow modification prior to infilling the thermal contraction crack. When the snowpack melts, a 1-4‰ enrichment in $\delta^{18}O$ has been identified in the snow melt (Fig. 6.8; Feng et al., 2002; Taylor et al., 2002). The leftover snowpack will typically be isotopically heavier (Lee, 2014). A difference in meteorological conditions (due to land uplift for example) will affect the isotopic signature of the fresh snowpack and the melt rate (Lee et al., 2010). Therefore, given the dynamic nature of the land-climate interaction, it is difficult to eliminate these factors from the IW $\delta^{18}O$ dataset. Thus, IW $\delta^{18}O$ should only be used as a first order inference on regional climate and not used as a direct reflection of past temperatures. For example, Holland et al. (2020) isolate a 4‰ difference over the Holocene, this is interpreted as a late-Holocene warming, occurring earlier than the industrial area (Fig. 6.7 B). IW $\delta^{18}O$ from the northern Klondike (Yukon; Grinter et al., 2019) also show a similar trend. But, $\delta^{18}O$ ice core records from the Agassiz, Penny-95, Academii Nauk show a persistent cooling trend for the Holocene; with this cooling trend also evident in ice cap stable-isotope records from the Antarctic, Huscaran, and some from Greenland (Fisher & Koerner, 2014). Hence, the results are likely not showing a direct climate signal but instead are a result of post-depositional isotopic modification. Moreover, perhaps in order to use the $\delta^{18}O$ from ice wedges for paleoclimate reconstructions a growth curve for each type of wedge must be established to get the best paleo proxy temperature results. This is comparable to tree ring studies, which require multiple trees of the same species to establish a chronology.

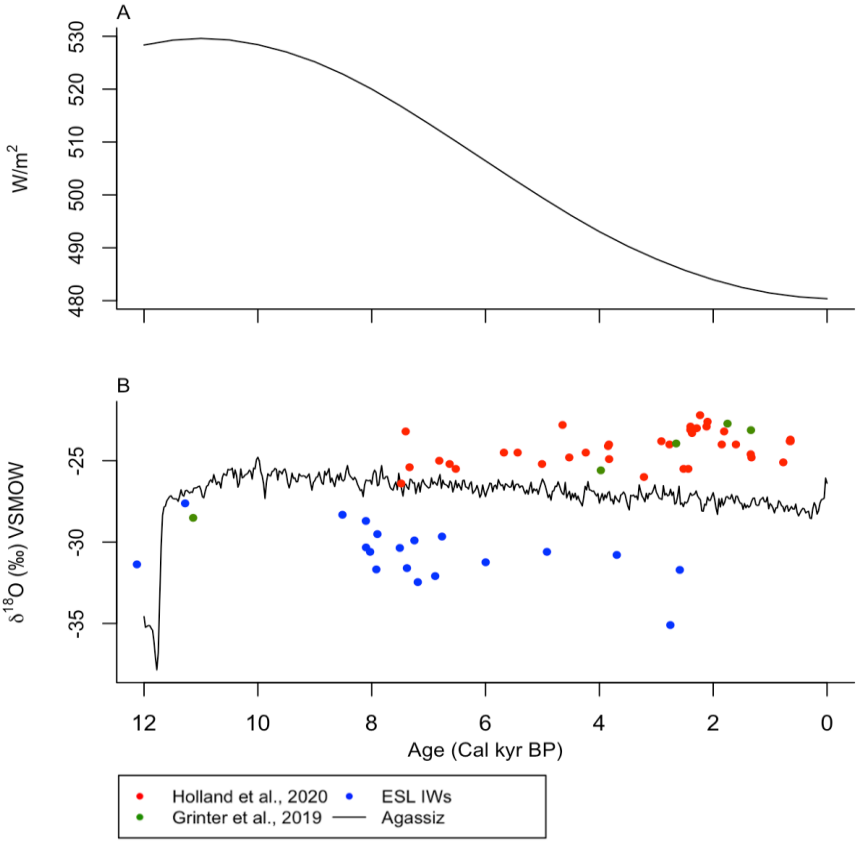

Figure 6.7. (A) Summer Solstice Solar insolation at 65°N (Laskar et al., 2004). (B) Agassiz Ice cap $\delta^{18}O$ records (Lecavalier et al., 2017) compared against ice wedge $\delta^{18}O$ from the Western Canadian Arctic (Holland et al., 2020; Grinter et al., 2019) and the Canadian High Arctic (Eureka Sound Lowlands).

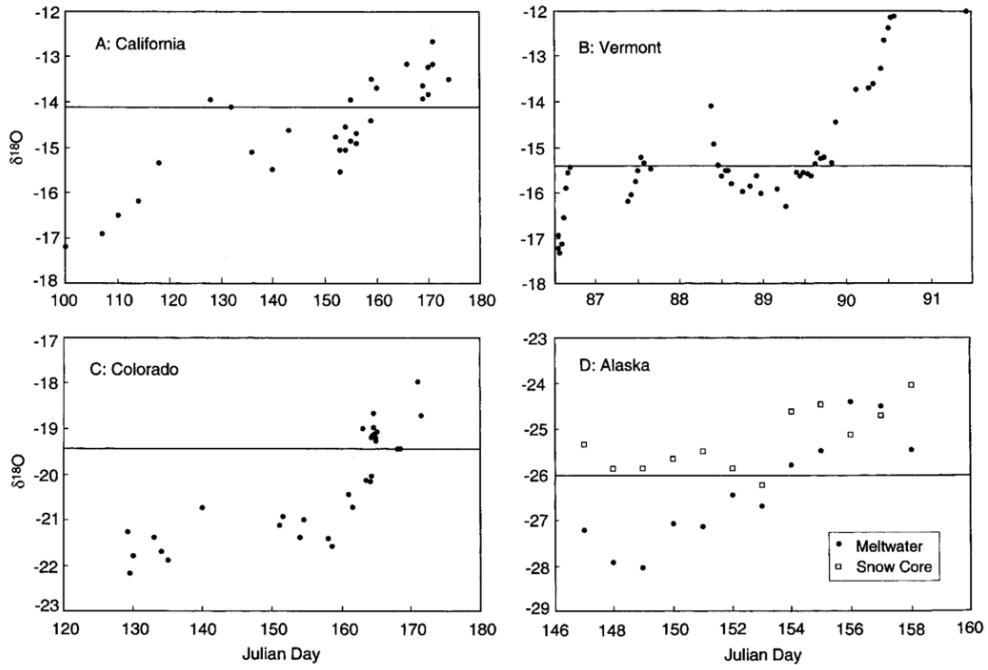

Figure 6.8. Isotopic composition of meltwater throughout a melt season for four locations: (A) Central Sierra Snow Laboratory, California; (B) Sleeper River Research Watershed, Vermont; (C) Niwot Ridge, Colorado and; (D) Imnavait Creek, Alaska. Horizonal line represents the average snowpack $\delta^{18}O$ for each site. Figure adopted from Talyor et al. (2002).

6.2.3. Biogeochemical Composition of Ice Wedges as an Alternative Paleotemperature Proxy

This section presents the use of IW biogeochemistry in respect to its age which can be used as a proxy for past climates. In Fig. 6.9, the $^{13}C_{DOC}$ isotopes within the vertically sampled IWs are compared against their respective age. These isotopes represent the type of plant grown, and more specifically the method of photosynthesis the plant uses (Clark & Fritz, 1997). The low $^{13}C_{DOC}$ values (-27.23‰ and -24.38‰) indicate that C3 plants dominated this area during the late Pleistocene and early Holocene up until 2.5ka when ice vein formation ceases. In order for IWs to crack and infill, an area must be ice free in order for ground temperatures to be suitable for cracking (Lachenbruch, 1962; Dostovalov, 1957). For the late Pleistocene dated IWs, the moisture source was primarily from glacial melt (Section 6.1.3). The $\delta^{13}C_{DOC}$ would have been originally preserved in the glacier as the environment during the early Holocene, when the meltwater was deposited in the wedge, would have not yet been colonized by plants (Gajewski, 2015). From 8-2.5 ka, the $\delta^{13}C_{DOC}$ of the sampled ice wedge becomes progressively depleted, this may be due to the later arrival (8.8 to 4.2 ka) of shrubs to the CAA and Greenland (Bennike, 1999; Gajewski, 2015). Or, it could be attributed to the variation in climate for this area as it would have an impact on the enrichment of $\delta^{13}C_{DOC}$. Wooller et al. (2007) for example found that with grasses and sedges, those that lived in dry environments would be $\delta^{13}C$ enriched (avg. 26.1 ±1.2‰). With modern and subfossil samples of grass and sedges the $\delta^{13}C$ will become more depleted with a wetter environment. In the context of the ESL, the shift in $\delta^{13}C$ during the Holocene would be attributed in part to the formation of polygonal terrain. Without accounting for the shift in $\delta^{13}C$ of shrubs (ex. *Dryas arctica*), the formation of troughs would encourage a wetter environment for grasses and sedges. And, with that, more $\delta^{13}C_{DOC}$ deposited in the wedges would be from the grass and sedge species inhabiting the IW trough, assuming that the primary contribution of snow and subsequent snowmelt originates from within in the IW trough (Section 6.1.3).

The concentration of five predominant ions change through time (Fig. 6.9). These high levels during the late Pleistocene and early Holocene are characteristic for this period and coincides with glacial ice core records (Fisher & Koerner, 2005; Fisher et al., 1998). Ionic concentration of marine-sourced ions (Na, Cl, & SO_4) declines whereas terrestrial sources (Ca & Mg) increases, which is a characteristic of the Holocene cold period (Fisher & Koerner, 2005). The opposite occurs in the mid to late Holocene (5-3 ka), where an increase in marine ions and decrease in terrestrial ions is indicative of a stronger marine presence and is similar to glacial ice core records from the Penny Ice Cap and coincides with the Mid-Holocene secondary warm period (Fisher & Koerner, 2014; Fisher et al., 1998). The concentration of sulphate in the surface IW samples follows a similar pattern to that recreated for the Holocene from the GISP2 ice core record for non-volcanic sulphate (Fisher & Koerner, 2005). This evidence suggests that the ionic composition of ice wedges can be used to infer past environmental and climate conditions for a region. Moreover, it shows that multiple ice wedges are required to establish a chronology and that the current use of one or two ice wedges as paleo-temperature proxies does not provide an accurate representation for that region.

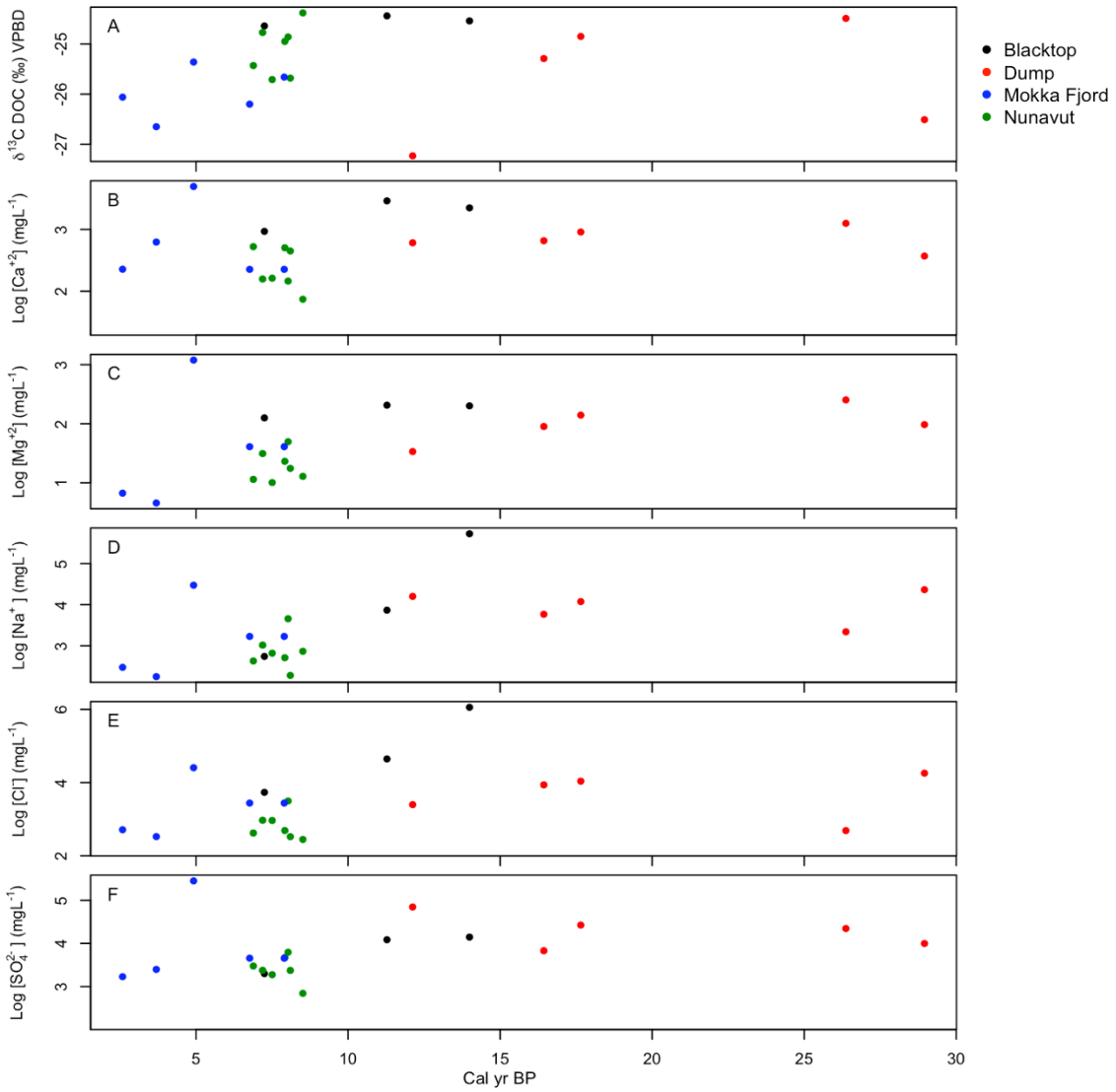

Figure 6.9. Calibrated ice wedge ages compared against contents. (A) δ $^{13}C_{DOC}$; (B) log transformed [Ca^{2+}]; (C) log transformed [Mg^{2+}]; (D) log transformed [Na^{+}]; (E) log transformed [Cl^{-}] and; (F) log transformed [SO_4^{-2}]. This data is from the vertically sampled ice wedges.

Chapter 7: Conclusions

As stated in the beginning of this report, the purpose of this study is twofold: (1) to investigate the timing ice wedge activity in the Eureka Sound Lowlands (ESL) and, (2) to test the use of ice wedges (IWs) in the Eureka region as paleotemperature proxies. As a result, the main findings of this report are as follows:

1. Dissolved organic carbon (DOC) and geochemical composition of sampled ice wedges is similar to the snow sample, indicating that the moisture source for the IWs in the ESL is snow melt. However, DOC/Cl (molar) ratio of IW samples suggests a minor contribution of leached surface organics.
2. IW cracking occurrence is influenced by IW width. Mackay (1974) developed a cracking probability curve based on a regions average IW width and standard deviation. This concept suggests that IW growth is non-linear.
3. The age ($^{14}C_{DOC}$) of IWs can be used to investigate IW activity in a region. In the ESL, ice wedges were active between 9-2.5 ka, which indicates that permafrost aggraded the sediments directly following marine regression.
4. Peak IW activity for the ESL occurs during the early-Holocene following deglaciation and marine regression. IW activity in the ESL is a direct result of changing snow cover conditions and, more specifically, its effect on ground temperature and volume of snow meltwater.
5. The majority of sampled IWs in the ESL show $^{14}C_{DOC}$ dates that are youngest in the centre and older on the edges, as expected considering typical IW growth. Two IWs do not follow this growth trend. The ice wedge EU19-W1 was formed in massive ice and thus the age variation observed is likely because the massive ice was also sampled. Whereas the variation in EU19-W5 could have been a result of sampling error. In addition, peripheral cracking was found to occur in small and large IWs, suggesting that the size of the wedge does not prevent peripheral cracking from occurring
6. Rayleigh-type isotopic fractionation was attributed to an approximate 2‰ difference in ^{18}O with depth.
7. A comparison with glacial ice core $\delta^{18}O$ shows that the stable water isotopes of an IW should be used as first-order temperature inferences as a snowpack will undergo isotopic modification during the melt season and show an isotopic enrichment of ~4‰.
8. The $\delta^{13}C_{DOC}$ of sampled IWs was used to infer when shrubs arrived in the region. The geochemical composition of IWs was used to identify the influence of marine or terrestrial moisture sources which can be used to interpret past environmental and climate conditions for a region. This data showed a similarity to the geochemical content of glacial ice cores.

One of the limitations to this study is that only nine IWs in total were studied over two summers. A more robust dataset may support this study's claims or yield different results. Next, there is a bias towards IWs formed on sloped terrain. This bias occurred because of the sampling procedure; all of the samples were chosen from the headwall of thaw slumps and thaw slumps are formed on slopes. Including IWs that formed on flat terrain may yield different results, especially regarding ice wedge symmetry and cracking location.

Future ice wedge studies may attempt to determine if there is a correlation between elevation, snow accumulation and ice wedge activity. Moreover, the correlation between cracking location and ice wedge width should also be examined further. Another study could examine the symmetry of $\delta^{18}O$ and D-excess in an IW and compare the results against the wedges' shape. Another future study may examine ion concentration at depth to better understand the evolution of snowmelt in a season and how it changes at depth within an IW. Also, the direction of freezing within an ice wedge can be modeled via isotope fractionation. Also, a future study may look to understand the relationship between ice vein width and a warming climate. Such studies may lead to a better understanding of the paleoclimate information stored in ice wedges.

References

Abolt, C. J., Young, M. H., Atchley, A. L., & Harp, D. R. (2018). Microtopographic control on the ground thermal regime in ice wedge polygons. *Cryosphere*, *12*(6), 1957–1968. https://doi.org/10.5194/tc-12-1957-2018

Allard, M., & Kasper, J. N. (1998). Temperature Conditions for Ice-Wedge Cracking: Field Measurements from Salluit, Northern Quebec. *Permafrost - Seventh International Confrence*, (55), 5–12.

Alt, B. T., & Maxwell, B. (2000). Overview of the modern arctic climate. *Bulletin of the Geological Survey of Canada*, (529), 17–36.

Atkinson, D. E., Alt, B., & Gajewski, K. (2000). A New Database of High Arctic Climate Data from the Polar Continental Shelf Project Archives. *Bulletin of the American Meteorological Society*, *81*(11), 2621–2629. https://doi.org/10.1175/1520-0477(2000)081<2621:ANDOHA>2.3.CO;2

Ballantyne, C., Williams, P. J., & Smith, M. W. (1990). The Frozen Earth: Fundamentals of Geocryology. In *Transactions of the Institute of British Geographers* (Vol. 15). https://doi.org/10.2307/622856

Becker, M. S., Davies, T. J., & Pollard, W. H. (2016). Ground ice melt in the high Arctic leads to greater ecological heterogeneity. *Journal of Ecology*, *104*(1), 114–124. https://doi.org/10.1111/1365-2745.12491

Bell, T. (1996). The last glaciation and sea level history of. *Fosheim Peninsula, Ellesmere Island, Canadian High Arctic. Canadian Journal of Earth Sciences*, *33*, 1075–1086.

Bell, T., & Hodgson, D. A. (2000). Quaternary geology and glacial history of Fosheim Peninsula, Ellesmere Island, Nanavut. In *Bulletin of the Geological Survey of Canada*. https://doi.org/10.4095/211957

Bell, T. J. (1992). *Glacial and sea level history of western Fosheim Peninsula, Ellesmere Island, Arctic Canada*.

Bennike, O. (1999). Colonisation of Greenland by plants and animals after the last ice age: a review. In *Polar Record* (Vol. 35).

Bernard-Grand'Maison, C., & Pollard, W. (2018). An Estimate of Ice Wedge Volume for a High Arctic Polar Desert Environment, Fosheim Peninsula, Ellesmere Island. *The Cryosphere Discussions*, *12*, 1–28. https://doi.org/10.5194/tc-2018-29

Blake Jr., W. (1970). Studies of glacial history in Arctic Canada. I. Pumice, radiocarbon dates, and differential postglacial uplift in the eastern Queen Elizabeth Islands. In *Canadian Journal of Earth Sciences* (Vol. 7). https://doi.org/10.1139/e70-065

Blinov, A., Alfimov, V., Beer, J., Gilichinsky, D., Schirrmeister, L., Kholodov, A., … Wetterich, S. (2009). Ratio of 36Cl/Cl in ground ice of east Siberia and its application for chronometry. *Geochemistry, Geophysics, Geosystems*, *10*(11). https://doi.org/10.1029/2009GC002548

Boereboom, T., Samyn, D., Meyer, H., & Tison, J.-L. (2013). Stable isotope and gas properties of two climatically contrasting (Pleistocene and Holocene) ice wedges from Cape Mamontov Klyk, Laptev Sea, northern Siberia. *The Cryosphere*, *7*, 31–46. https://doi.org/10.5194/tc-7-31-2013

Bronk Ramsey, C. (2009). Bayesian Analysis of Radiocarbon Dates. *Radiocarbon*, *51*(1), 337–360. https://doi.org/10.2458/azu_js_rc.v51i1.3494

Buizert, C., Keisling, B. A., Box, J. E., He, F., Carlson, A. E., Sinclair, G., & DeConto, R. M. (2018). Greenland-Wide Seasonal Temperatures During the Last Deglaciation. *Geophysical Research Letters*.

https://doi.org/10.1002/2017GL075601

Burn, C. R. (1997). Cryostratigraphy, paleogeography, and climate change during the early Holocene warm interval, western Arctic coast, Canada. In *Canadian Journal of Earth Sciences* (Vol. 34). https://doi.org/10.1139/e17-076

Buttle, J. M., & Fraser, K. E. (1992). Hydrochemical fluxes in a high arctic wetland basin during spring snowmelt. *Arctic & Alpine Research*, *24*(2), 153–164. https://doi.org/10.2307/1551535

Christiansen, H. H., Etzelmüller, B., Isaksen, K., Juliussen, H., Farbrot, H., Humlum, O., … Ødegård, R. S. (2010). The thermal state of permafrost in the nordic area during the international polar year 2007-2009. *Permafrost and Periglacial Processes*, *21*(2), 156–181. https://doi.org/10.1002/ppp.687

Clark, I. (2015). Groundwater geochemistry and isotopes. In *Groundwater Geochemistry and Isotopes*. https://doi.org/10.1201/b18347

Clark, I. D., & Fritz, P. (1997a). Age Dating Old Groundwaters. In *Environmental Isotopes in Hydrogeology* (p. 48).

Clark, I. D., & Fritz, P. (1997b). Identifying and Dating Modern Groundwaters. In *Environmental Isotopes in Hydrogeology* (p. 26).

Clark, I., Lauriol, B., Marschner, M., Sabourin, N., Chauret, Y., & Desrochers, A. (2004). Endostromatolites from permafrost karst, Yukon, Canada: Paleoclimatic proxies for the Holocene hypsithermal. *Canadian Journal of Earth Sciences*, *41*(4), 387–399. https://doi.org/10.1139/e04-014

Conklin Jr, A. R. (2005). *Introduction to Soil Chemistry: analysis and instrumentation*. https://doi.org/10.1002/0471728225

Couture, N. J., & Pollard, W. H. (1998). An assessment of ground ice volume near eureka, northwest territories. *In Permafrost - Seventh International Converence*, *55*, 195–200.

Crann, C. A., Murseli, S., St-Jean, G., Zhao, X., Clark, I. D., & Kieser, W. E. (2017). First Status Report on Radiocarbon Sample Preparation Techniques at the A.E. Lalonde AMS Laboratory (Ottawa, Canada). *Radiocarbon*, *59*(3), 695–704. https://doi.org/10.1017/RDC.2016.55

Crate, S., Ulrich, M., Habeck, J. O., Desyatkin, A. R., Desyatkin, R. V., Desyatkin, A. R., … Mészáros, C. (2017). Permafrost livelihoods: A transdisciplinary review and analysis of thermokarst-based systems of indigenous land use. *Anthropocene*, *18*, 89–104. https://doi.org/10.1016/j.ancene.2017.06.001

Dansgaard, W. (1964). Stable isotopes in precipitation. *Tellus*, *16*(4), 436–468. https://doi.org/10.3402/tellusa.v16i4.8993

De Caritat, P., Hall, G., Gìslason, S., Belsey, W., Braun, M., Goloubeva, N. I., … Vaive, J. E. (2005). Chemical composition of arctic snow: Concentration levels and regional distribution of major elements. *Science of the Total Environment*, *336*(1–3), 183–199. https://doi.org/10.1016/j.scitotenv.2004.05.031

Dereviagin, A. Y., Meyer, H., Chizhov, A. B., Hubberten, H. W., & Simonov, E. F. (2000). New data on the isotopic composition and evolution of modern ice wedges in the Laptev Sea region. *Polarforschung*, *70*(1–2), 27–35.

Drozdov, D. S., Malkova, G. V., Romanovsky, V. E., Rumyantseva, Y. V., Abramov, A. A., Konstabtinov, P. Y., … Streletskiy, D. A. (2015). Monitoring of permafrost in Russia. Russian database and the international GTN-P project. *68e Conférence Canadienne de Géotechnique et 7e Conférence Canadienne Sur Le Pergélisol, 20 Au*

23 Septembre 2015, Québec, Québec., 3–9.

Dumond, D. E., & Griffin, D. G. (2002). Measurements of the marine reservoir effect on radiocarbon ages in the eastern Bering Sea. *Arctic*, *55*(1), 77–86. https://doi.org/10.14430/arctic692

Dyke, A S, Andrews, J. T., Clark, P. U., England, J. H., Miller, G. H., Shaw, J., & Veillette, J. J. (2002). The Laurentide and Innuitian ice sheets during the Last Glacial Maximum. In *Quaternary Science Reviews* (Vol. 21).

Dyke, Arthur S. (1999). Last Glacial Maximum and deglaciation of devon island, arctic canada: support for an innuitian ice sheet. In *Quaternary Science Reviews* (Vol. 18).

Edlund, S. A., & Alt, B. T. (1989). Regional congruence of vegetation and summer climate patterns in the Queen Elizabeth Islands, Northwest Territories, Canada. *Arctic*, *42*(1), 3–23. https://doi.org/10.14430/arctic1635

Edlund, S. A., Alt, B. T., & Garneau, M. (2000). Vegetation patterns on Fosheim Penisula, Ellemere Island, Nunavut. In *Bulletin of the Geological Survey of Canada*.

Edlund, S. A., & Garneau, M. (2000). Overview of vegetation zonation in the Arctic. In *Bulletin of the Geological Survey of Canada*. https://doi.org/10.4095/211952

Embry, A., & Beauchamp, B. (2008). Chapter 13 Sverdrup Basin. *Sedimentary Basins of the World*, *5*(C), 451–471. https://doi.org/10.1016/S1874-5997(08)00013-0

England, J., Sharp, M., Lemmen, D. S., & Bednarski, J. (1991). On the extent and thickness of the Innuitian Ice Sheet: a postglacial-adjustment approach: Discussion. *Canadian Journal of Earth Sciences*, *28*(10), 1689–1695. https://doi.org/10.1139/e91-152

England, J, Atkinson, N., Bednarski, J., Dyke, A. S., Hodgson, D. A., & Ó Cofaigh, C. (2006). The Innuitian Ice Sheet: configuration, dynamics and chronology. *Quaternary Science Reviews*, *25*(7–8), 689–703. https://doi.org/10.1016/j.quascirev.2005.08.007

England, John. (1996). Glacier dynamics and paleoclimatic change during the last glaciation of eastern Ellesmere Island, Canada. In *Canadian Journal of Earth Sciences* (Vol. 33). https://doi.org/10.1139/e96-060

Ewing, S. A., Paces, J. B., O'Donnell, J. A., Jorgenson, M. T., Kanevskiy, M. Z., Aiken, G. R., … Striegl, R. (2015). Uranium isotopes and dissolved organic carbon in loess permafrost: Modeling the age of ancient ice. *Geochimica et Cosmochimica Acta*, *152*, 143–165. https://doi.org/10.1016/j.gca.2014.11.008

Farbrot, H., Isaksen, K., Etzelmüller, B., & Gisnås, K. (2013). *Ground Thermal Regime and Permafrost Distribution under a Changing Climate in Northern Norway*. https://doi.org/10.1002/ppp.1763

Feng, X., Taylor, S., Renshaw, C. E., & Kirchner, J. W. (2002). Isotopic evolution of snowmelt 1. A physically based one-dimensional model. *Water Resources Research*, *38*(10), 35-1-35–38. https://doi.org/10.1029/2001wr000814

Fisher, D. A., & Koerner, R. M. (2014). Holocene ice-core climate history - A multi-variable approach. In *Global Change in the Holocene* (Vol. 9780203785, pp. 281–293). https://doi.org/10.4324/9780203785027

Fisher, D. A., Koerner, R. M., Bourgeois, J. C., Zielinski, G., Wake, C., Hammer, C. U., … Gerasimoff, M. (1998). Penny Ice Cap cores, Baffin Island, Canada, and the Wisconsinan Foxe Dome connection: Two states of Hudson Bay ice cover. *Science*, *279*(5351), 692–696. https://doi.org/10.1126/science.279.5351.692

Fortier, D., & Allard, M. (2005). Frost-cracking conditions, Bylot Island, eastern Canadian Arctic archipelago.

Permafrost and Periglacial Processes, *16*(2), 145–161. https://doi.org/10.1002/ppp.504

Fortier, D., Allard, M., & Shur, Y. (2007). Observation of rapid drainage system development by thermal erosion of ice wedges on Bylot Island, Canadian Arctic Archipelago. *Permafrost and Periglacial Processes*, *18*(3), 229–243. https://doi.org/10.1002/ppp.595

French, H. M., & Guglielmin, M. (2000). Frozen ground phenomena in the vicinity of the Terra Nova bay, Northern Victoria land, Antarctica: A preliminary report. *Geografiska Annaler, Series A: Physical Geography*, *82*(4), 513–526. https://doi.org/10.1111/j.0435-3676.2000.00138.x

French, H., & Shur, Y. (2010). The principles of cryostratigraphy. *Earth-Science Reviews*, *101*(3–4), 190–206. https://doi.org/10.1016/j.earscirev.2010.04.002

French, H M. (2007). *The Periglaical Environment, 3rd Ed. Wiley. 458p.* John Wiley & Sons.

French, Hugh M. (2018). *The Periglaical Environment*. John Wiley & Sons.

Fritz, M., Wetterich, S., Schirrmeister, L., Meyer, H., Lantuit, H., Preusser, F., & Pollard, W. H. (2012). Eastern Beringia and beyond: Late Wisconsinan and Holocene landscape dynamics along the Yukon Coastal Plain, Canada. *Palaeogeography, Palaeoclimatology, Palaeoecology*, *319–320*, 28–45. https://doi.org/10.1016/j.palaeo.2011.12.015

Fritz, M., Wolter, J., Rudaya, N., Palagushkina, O., Nazarova, L., Obu, J., … Wegener, A. (2016). Holocene ice-wedge polygon development in northern Yukon permafrost peatlands (Canada). *Quaternary Science Reviews*, *147*, 279–297. https://doi.org/10.1016/j.quascirev.2016.02.008

Gajewski, K. (2015). Impact of Holocene climate variability on Arctic vegetation. *Global and Planetary Change*, *133*, 272–287. https://doi.org/10.1016/j.gloplacha.2015.09.006

Garneau, M. (2000). Peat accumulation and climatic change in the High Arctic. In *Bulletin of the Geological Survey of Canada*. https://doi.org/10.4095/211968

Goodrich, L. E. (1982). The influence of snow cover on the ground thermal regime. *Canadian Geotechnical Journal*, *19*(4), 421–432. https://doi.org/10.1139/t82-047

Government of Canada. (2020). Historical Data: Eureka Climate. Retrieved February 2, 2020, from http://climate.weather.gc.ca/climate_data/daily_data_e.html?StationID=50737

Grinter, M., Lacelle, D., Baranova, N., Murseli, S., & Clark, I. D. (2019). Late Pleistocene and Holocene ice-wedge activity on the Blackstone Plateau, central Yukon, Canada. *Quaternary Research*, *91*(1), 179–193. https://doi.org/10.1017/qua.2018.65

Heiri, O., Lotter, A. F., & Lemeke, G. (2001). Loss on ignition as a method for estimating organic and carbonate content in sediments: reproducibility and comparability of results. *Journal of Paleolimnology*, *25*, 101–110. https://doi.org/10.1016/0009-2541(93)90140-E

Hjort, J., Karjalainen, O., Aalto, J., Westermann, S., Romanovsky, V. E., Nelson, F. E., … Luoto, M. (2018). Degrading permafrost puts Arctic infrastructure at risk by mid-century. *Nature Communications*, *9*(1). https://doi.org/10.1038/s41467-018-07557-4

Hobbie, J. E., Shaver, G. R., Rastetter, E. B., Cherry, J. E., Goetz, S. J., Guay, K. C., … Kling, G. W. (2017). Ecosystem responses to climate change at a Low Arctic and a High Arctic long-term research site. *Ambio*, *46*,

160–173. https://doi.org/10.1007/s13280-016-0870-x

Hodgson, D. A. (1985). The last glaciation of west-central Ellesmere Island, Arctic Archipelago, Canada. In *Can. I. Earth Sci* (Vol. 22).

Hodgson, D. A., & Nixon, F. M. (1998). Ground ice volumes determined from shallow cores from western fosheim peninsula ellesmere island, northwest territories. In *Bulletin of the Geological Survey of Canada*. Ottawa: Government of Canada.

Holland, K. M., Porter, T. J., Froese, D. G., Kokelj, S. V., & Buchanan, C. A. (2020). Ice-Wedge Evidence of Holocene Winter Warming in the Canadian Arctic. *Geophysical Research Letters*, *47*(12). https://doi.org/10.1029/2020gl087942

Huges, T., Denton, G. H., & Grosswald, M. G. (1977). Was there a late-Würm Arctic Ice sheet. *Nature*, *266*(5603), 596–602.

Iizuka, Y., Miyamoto, C., Matoba, S., Iwahana, G., Horiuchi, K., Takahashi, Y., … Ohno, H. (2019). Ion concentrations in ice wedges: An innovative approach to reconstruct past climate variability. *Earth and Planetary Science Letters*, *515*, 58–66. https://doi.org/10.1016/j.epsl.2019.03.013

Jasechko, S., Lechler, A., Pausata, F. S. R., Fawcett, P. J., Gleeson, T., Cendon, D. I., … Yoshimura, K. (2015). Late-glacial to late-Holocene shifts in global precipitation δ18O. *Climate of the Past*, *11*(10), 1375–1393. https://doi.org/10.5194/cp-11-1375-2015

Kaufman, D. S., Axford, Y. L., Henderson, A. C. G., McKay, N. P., Oswald, W. W., Saenger, C., … Yu, Z. (2016). Holocene climate changes in eastern Beringia (NW North America) – A systematic review of multi-proxy evidence. *Quaternary Science Reviews*, *147*, 312–339. https://doi.org/10.1016/j.quascirev.2015.10.021

Kieser, W. E., Zhao, X. L., Clark, I. D., Cornett, R. J., Litherland, A. E., Klein, M., … Alary, J. F. (2015). The André E. Lalonde AMS Laboratory - The new accelerator mass spectrometry facility at the University of Ottawa. *Nuclear Instruments and Methods in Physics Research, Section B: Beam Interactions with Materials and Atoms*, *361*, 110–114. https://doi.org/10.1016/j.nimb.2015.03.014

Koch, J. C., Jorgenson, M. T., Wickland, K. P., Kanevskiy, M., & Striegl, R. (2018). Ice Wedge Degradation and Stabilization Impact Water Budgets and Nutrient Cycling in Arctic Trough Ponds. *Journal of Geophysical Research: Biogeosciences*, *123*(8), 2604–2616. https://doi.org/10.1029/2018JG004528

Kokelj, S. V., Pisaric, M. F. J., & Burn, C. R. (2007). Cessation of ice-wedge development during the 20th century in spruce forests of eastern Mackenzie Delta, Northwest Territories, Canada. *Canadian Journal of Earth Sciences*, *44*(11), 1503–1515. https://doi.org/10.1139/E07-035

Lacelle, D. (2011). On the δ18O, δD and D-excess relations in meteoric precipitation and during equilibrium freezing: Theoretical approach and field examples. *Permafrost and Periglacial Processes*, *22*(1), 13–25. https://doi.org/10.1002/ppp.712

Lachenbruch, A. H. (1962). Mechanics of Thermal Contraction Cracks and Ice-Wedge Polygons in Permafrost. In A. H. Lachenbruch (Ed.), *Mechanics of Thermal Contraction Cracks and Ice-Wedge Polygons in Permafrost* (Vol. 70, p. 0). https://doi.org/10.1130/SPE70-p1

Lachniet, M. S., Lawson, D. E., & Sloat, A. R. (2012). Revised14C dating of ice wedge growth in interior Alaska

(USA) to MIS 2 reveals cold paleoclimate and carbon recycling in ancient permafrost terrain. *Quaternary Research (United States)*, *78*(2), 217–225. https://doi.org/10.1016/j.yqres.2012.05.007

Lachniet, M. S., Lawson, D. E., Stephen, H., Sloat, A. R., & Patterson, W. P. (2016). Isoscapes of δ18O and δ2H reveal climatic forcings on Alaska and Yukon precipitation. *Water Resources Research*, *52*(8), 6575–6586. https://doi.org/10.1002/2016WR019436

Laskar, J., Robutel, P., Joutel, F., Gastineau, M., Correia, A. C. M., & Levrard, B. (2004). A long-term numerical solution for the insolation quantities of the Earth. *Astronomy and Astrophysics*, *428*(1), 261–285. https://doi.org/10.1051/0004-6361:20041335

Lauriol, B., Duchesne, C., & Clark, I. D. (1995). Systematique du Remplissage en Eau des Fentes de Gel: Les Resultats d'une etude Oxygene-18 et Deuterium. *Permafrost and Periglacial Processes*, *6*(1), 47–55. https://doi.org/10.1002/ppp.3430060106

Lecavalier, B. S., Fisher, D. A., Milne, G. A., Vinther, B. M., Tarasov, L., Huybrechts, P., … Dyke, A. S. (2017). High Arctic Holocene temperature record from the Agassiz ice cap and Greenland ice sheet evolution. *Proceedings of the National Academy of Sciences of the United States of America*, *114*(23), 5952–5957. https://doi.org/10.1073/pnas.1616287114

Lee, J. (2014). A numerical study of isotopic evolution of a seasonal snowpack and its meltwater by melting rates. *Geosciences Journal*, *18*(4), 503–510. https://doi.org/10.1007/s12303-014-0019-5

Lee, J., Feng, X., Faiia, A. M., Posmentier, E. S., Kirchner, J. W., Osterhuber, R., & Taylor, S. (2010). Isotopic evolution of a seasonal snowcover and its melt by isotopic exchange between liquid water and ice. *Chemical Geology*, *270*(1–4), 126–134. https://doi.org/10.1016/j.chemgeo.2009.11.011

Leffingwell, E. de K. (1915). Ground-Ice Wedges: The Dominant Form of Ground-Ice on the North Coast of Alaska. *The Journal of Geology*, *23*(7), 635–654. https://doi.org/10.1086/622281

Lewkowicz, A. G. (1994). Ice-wedge rejuvenation, fosheim peninsula, ellesmere Island, Canada. *Permafrost and Periglacial Processes*, *5*(4), 251–268. https://doi.org/10.1002/ppp.3430050405

Liljedahl, A. K., Boike, J., Daanen, R. P., Fedorov, A. N., Frost, G. V., Grosse, G., … Zona, D. (2016). Pan-Arctic ice-wedge degradation in warming permafrost and its influence on tundra hydrology. *Nature Geoscience*, *9*(4), 312–318. https://doi.org/10.1038/ngeo2674

MacDonald, G. M., Beilman, D. W., Kremenetski, K. V., Sheng, Y., Smith, L. C., & Velichko, A. A. (2006). Rapid early development of circumarctic peatlands and atmospheric CH 4 and CO2 variations. *Science*, *314*(5797), 285–288. https://doi.org/10.1126/science.1131722

MacDonald, M. K., Stadnyk, T. A., Déry, S. J., Braun, M., Gustafsson, D., Isberg, K., & Arheimer, B. (2018). Impacts of 1.5 and 2.0 °C Warming on Pan-Arctic River Discharge Into the Hudson Bay Complex Through 2070. *Geophysical Research Letters*, *45*(15), 7561–7570. https://doi.org/10.1029/2018GL079147

Mackay, J. R. (1972). The World Of Underground Ice. *Annals of the Association of American Geographers*, *62*(1), 1–22. https://doi.org/10.1111/j.1467-8306.1972.tb00839.x

Mackay, J. R. (1974a). Ice-Wedge Cracks, Garry Island, Northwest Territories. *Canadian Journal of Earth Sciences*, *11*, 1366–1383.

Mackay, J. R. (1974b). Reticulate Ice Veins in Permafrost, Northern Canada: Reply. *Canadian Geotechnical Journal*, *11*(1), 230–237. https://doi.org/10.1139/t75-018

Mackay, J. R. (1975). The Closing of Ice-wedge Cracks in Permafrost, Garry Island, Northwest Territories. In *Canadian Journal of Earth Sciences* (Vol. 12). https://doi.org/10.1139/e75-146

Mackay, J. R. (1984). The direction of ice-wedge cracking in permafrost: downward or upward? *Canadian Journal of Earth Sciences*, *21*(5), 516–524. https://doi.org/10.1139/e84-056

Mackay, J. R. (1990). Some observations on the growth and deformation of epigenetic, syngenetic and anti-syngenetic ice wedges. *Permafrost and Periglacial Processes*, *1*(1), 15–29. https://doi.org/10.1002/ppp.3430010104

Mackay, J. R. (1992). The frequency of ice-wedge cracking (1967–1987) at Garry Island, western Arctic coast, Canada. *Canadian Journal of Earth Sciences*, *29*(2), 236–248. https://doi.org/10.1139/e92-022

Mackay, J. R. (1993). Air temperature, snow cover, creep of frozen ground, and the time of ice-wedge cracking, western Arctic coast. *Canadian Journal of Earth Sciences*, *30*(8), 1720–1729. https://doi.org/10.1139/e93-151

Mackay, J. R., & Burn, C. R. (2002). The first 20 years (1978-1979 to 1998-1999) of ice-wedge growth at the Illisarvik experimental drained lake site, western Arctic coast, Canada. *Canadian Journal of Earth Sciences*, *39*(1), 95–111. https://doi.org/10.1139/e01-048

Matsuoka, N., Christiansen, H. H., & Watanabe, T. (2018). Ice-wedge polygon dynamics in Svalbard: Lessons from a decade of automated multi-sensor monitoring. *Permafrost and Periglacial Processes*, *29*(3), 210–227. https://doi.org/10.1002/ppp.1985

Meyer, H, Yoshikawa, K., Schirrmeister, L., & Andreev, A. (2008). The Vault Creek Tunnel (Fairbanks Region, Alaska) A Late Quaternary Palaeoenvironmental Permafrost Record. *Ninth International Confrence on Permafrost*, 1191–1196.

Meyer, Hanno, Dereviagin, A. Y., Siegert, C., & Hubberten', H.-W. (2002). Paleoelimate Studies on Bykovsky Peninsula, North Siberia Hydrogen and Oxygen Isotopes in Ground lee. *Polarforschung*, *70*(January 2001), 37–51.

Meyer, Hanno, Schirrmeister, L., Andreev, A., Wagner, D., Hubberten, H. W., Yoshikawa, K., … Brown, J. (2010). Lateglacial and Holocene isotopic and environmental history of northern coastal Alaska - Results from a buried ice-wedge system at Barrow. *Quaternary Science Reviews*, *29*(27–28), 3720–3735. https://doi.org/10.1016/j.quascirev.2010.08.005

Meyer, Hanno, Schirrmeister, L., Yoshikawa, K., Opel, T., Wetterich, S., Hubberten, H.-W., & Brown, J. (2010). Permafrost evidence for severe winter cooling during the Younger Dryas in northern Alaska. *Geophysical Research Letters*, *37*(3), n/a-n/a. https://doi.org/10.1029/2009GL041013

Miall, A. D. (1986). Eureka Sound Group. *Bullitin of Canadian Petroleum Geology*, *34*(2), 240–270.

Michel, F. A. (1982). *Isotope investigations of permafrost waters in northern Canada*.

Michel, F. A. (1990). Isotopic composition of ice-wedge ice in northwestern Canada. *Fifth Canadian Permafrost Conference*, 5–9.

Murseli, S., Middlestead, P., St-Jean, G., Zhao, X., Jean, C., Crann, C. A., … Clark, I. D. (2019). The Preparation of Water (DIC, DOC) and Gas (CO 2 , CH 4) Samples for Radiocarbon Analysis at AEL-AMS, Ottawa, Canada.

Radiocarbon, *61*(5), 1563–1571. https://doi.org/10.1017/RDC.2019.14

Nitzbon, J., Langer, M., Westermann, S., Martin, L., Aas, K. S., & Boike, J. (2019). Pathways of ice-wedge degradation in polygonal tundra under different hydrological conditions. *The Cryosphere*, *13*, 1089–1123. https://doi.org/10.5194/tc-13-1089-2019

Opel, T., Dereviagin, A. Y., Meyer, H., Schirrmeister, L., & Wetterich, S. (2011). Palaeoclimatic information from stable water isotopes of Holocene ice wedges on the Dmitrii Laptev Strait, northeast Siberia, Russia. *Permafrost and Periglacial Processes*, *22*(1), 84–100. https://doi.org/10.1002/ppp.667

Opel, T., Laepple, T., Meyer, H., Dereviagin, A. Y., & Wetterich, S. (2017). Northeast Siberian ice wedges confirm Arctic winter warming over the past two millennia. *Holocene*, *27*(11), 1789–1796. https://doi.org/10.1177/0959683617702229

Opel, T., Meyer, H., Wetterich, S., Laepple, T., Dereviagin, A., & Murton, J. (2018). Ice wedges as archives of winter paleoclimate: A review. *Permafrost and Periglacial Processes*, *29*(3), 199–209. https://doi.org/10.1002/ppp.1980

Payette, S., Gauthier, L., & Grenier, I. (1986). Dating ice-wedge growth in subarctic peatlands following deforestation. *Nature*, *322*(6081), 724–727. https://doi.org/10.1038/322724a0

Peros, M. C., & Gajewski, K. (2008). Holocene climate and vegetation change on Victoria Island, western Canadian Arctic. *Quaternary Science Reviews*, *27*(3–4), 235–249. https://doi.org/10.1016/j.quascirev.2007.09.002

Pollard, W. H., & French, H. M. (1980). A first approximation of the volume of ground ice, Richards Island, Pleistocene Mackenzie delta, Northwest Territories, Canada. In *Canadian Geotechnical Journal* (Vol. 17). https://doi.org/10.1139/t80-059

Pollard, W., Ward, M., & Becker, M. (2015). The Eureka Sound lowlands : an ice-rich permafrost landscape in transition. *68e Conférence Canadienne de Géotechnique et 7e Conférence Canadienne Sur Le Pergélisol, 20 Au 23 Septembre 2015, Québec, Québec.*, (Figure 1).

Porter, T. J., Froese, D. G., Feakins, S. J., Bindeman, I. N., Mahony, M. E., Pautler, B. G., … Weijers, J. W. H. (2016). Multiple water isotope proxy reconstruction of extremely low last glacial temperatures in Eastern Beringia (Western Arctic). *Quaternary Science Reviews*, *137*, 113–125. https://doi.org/10.1016/j.quascirev.2016.02.006

Porter, T. J., & Opel, T. (2020). Recent advances in paleoclimatological studies of Arctic wedge- and pore-ice stable-water isotope records. *Permafrost and Periglacial Processes*, (February), 1–13. https://doi.org/10.1002/ppp.2052

Rae, R. W. (1951). Joint Arctic Weather Project. In *Arctic* (Vol. 4). https://doi.org/10.14430/arctic3932

Reimer, P. J., Bard, E., Bayliss, A., Beck, J. W., Blackwell, P. G., Ramsey, C. B., … van der Plicht, J. (2013). IntCal13 and Marine13 Radiocarbon Age Calibration Curves 0–50,000 Years cal BP. *Radiocarbon*, *55*(04), 1869–1887. https://doi.org/10.2458/azu_js_rc.55.16947

Romanovsky, V. E., Smith, S. L., Isaksen, K., Shiklomanov, N. I., Streletskiy, D. A., Kholodov, A. L., … Marchenko, S. S. (2018). Terrestrial Permafrost. In *State of the Climate in 2017*.

Roy, C. (2018). *Origin of massive ground ice in the Eureka Sound Lowlands, Nunavut*. Mcgill University.

Sarrazin, D., & Allard, M. (2011). Monitoring of thermal contraction cracking in ice wedge polygons. *GEOQuébec*

2015. 68th Canadian Geotechnical Conference, 7th Canadian Permafrost Conference.

Schuster, P. F., Schaefer, K. M., Aiken, G. R., Antweiler, R. C., Dewild, J. F., Gryziec, J. D., … Zhang, T. (2018). Permafrost Stores a Globally Significant Amount of Mercury. *Geophysical Research Letters*, *45*(3), 1463–1471. https://doi.org/10.1002/2017GL075571

Schuur, E. A. G., McGuire, A. D., Schädel, C., Grosse, G., Harden, J. W., Hayes, D. J., … Vonk, J. E. (2015). Climate change and the permafrost carbon feedback. *Nature*, Vol. 520, pp. 171–179. https://doi.org/10.1038/nature14338

Screen, J. A., & Francis, J. A. (2016). Contribution of sea-ice loss to Arctic amplification is regulated by Pacific Ocean decadal variability. *Nature Climate Change*, *6*(9), 856–860. https://doi.org/10.1038/nclimate3011

Shumskii, P. A. (1964). *Principles of Structural Glaciology. Translation D. Kraus*.

Shur, Y., Hinkel, K. M., & Nelson, F. E. (2005). The Transient Layer: Implications for Geocryology and Climate-Change Science. *Process*, *16*, 5–17. https://doi.org/10.1002/ppp.518

Simon, K. M., James, T. S., & Dyke, A. S. (2015). A new glacial isostatic adjustment model of the Innuitian Ice Sheet, Arctic Canada. *Quaternary Science Reviews*. https://doi.org/10.1016/j.quascirev.2015.04.007

Smith, M. W., & Riseborough, D. W. (2002). Climate and the limits of permafrost: A zonal analysis. *Permafrost and Periglacial Processes*, *13*(1), 1–15. https://doi.org/10.1002/ppp.410

Smith, S. L., Romanovsky, V. E., Lewkowicz, A. G., Burn, C. R., Allard, M., Clow, G. D., … Throop, J. (2010). Thermal state of permafrost in North America: A contribution to the international polar year. *Permafrost and Periglacial Processes*, *21*(2), 117–135. https://doi.org/10.1002/ppp.690

Smith, S L, Chartrand, J., Duchesne, C., & Ednie, M. (2016). *Report on 2015 field activities and collection of ground thermal and active layer data in the Mackenzie Corridor, Northwest Territories*. https://doi.org/10.4095/299296

Smith, Sharon L, Lewkowicz, A. G., & Duchesne, C. (2015). Variability and Change in Permafrost Thermal State in Northern Canada. *68e Conférence Canadienne de Géotechnique et 7e Conférence Canadienne Sur Le Pergélisol, 20 Au 23 Septembre 2015, Québec, Québec.*, (Figure 1), 1–6.

St-Jean, G. (2003). Automated quantitative and isotopic (13C) analysis of dissolved inorganic carbon and dissolved organic carbon in continuous-flow using a total organic carbon analyser. *Rapid Communications in Mass Spectrometry*, *17*(5), 419–428. https://doi.org/10.1002/rcm.926

St-Jean, M., Lauriol, B., Clark, I. D., Lacelle, D., & Zdanowicz, C. (2011). Investigation of ice-wedge infilling processes using stable oxygen and hydrogen isotopes, crystallography and occluded gases (O2, N2, Ar). *Permafrost and Periglacial Processes*, *22*(1), 49–64. https://doi.org/10.1002/ppp.680

Steedman, A. E., Lantz, T. C., & Kokelj, S. V. (2017). Spatio-Temporal Variation in High-Centre Polygons and Ice-Wedge Melt Ponds, Tuktoyaktuk Coastlands, Northwest Territories. *Permafrost and Periglacial Processes*, *28*(1), 66–78. https://doi.org/10.1002/ppp.1880

Streletskaya, I., Vasiliev, A., & Meyer, H. (2011). Isotopic composition of syngenetic ice wedges and palaeoclimatic reconstruction, western Taymyr, Russian Arctic. *Permafrost and Periglacial Processes*, *22*(1), 101–106. https://doi.org/10.1002/ppp.707

Stuiver, M., & Polach, H. A. (1977). Reporting of 14C data. *Radiocarbon*, *19*(3), 355–363.

https://doi.org/10.1016/j.forsciint.2010.11.013

Sutherland, P. D. (2000). Preliminary results of archeological research on Fosheim Peninsula and in adjacent areas of western Ellesmere and eastern Axel Heiberg islands, Nunavut. *Bulletin of the Geological Survey of Canada*, (529), 319–324. https://doi.org/10.4095/211970

Suzuoki, T., & Kumura, T. (1973). D/H and 18O/16O fractionation in ice-water systems. *Mass Spectroscopy*, *21*, 229–223.

Tanski, G., Couture, N., Lantuit, H., Eulenburg, A., & Fritz, M. (2016). Eroding permafrost coasts release low amounts of dissolved organic carbon (DOC) from ground ice into the nearshore zone of the Arctic Ocean. *Global Biogeochemical Cycles*. https://doi.org/10.1002/2015GB005337

Taylor, S., Feng, X., Williams, M., & McNamara, J. (2002). How isotopic fractionation of snowmelt affects hydrograph separation. *Hydrological Processes*, *16*(18), 3683–3690. https://doi.org/10.1002/hyp.1232

Thompson, D. K., & Woo, M. K. (2009). Seasonal hydrochemistry of a high Arctic wetland complex. *Hydrological Processes*, *23*(10), 1397–1407. https://doi.org/10.1002/hyp.7271

Vasil'chuk, Y. K. (1992). *Oxygen isotope composition of ground ice: Application to paleogeocryological reconstructions* (Vol. 58).

Vasil'chuk, Y. K., Budantseva, N. A., Christiansen, H. H., Chizhova, J. N., Vasil'chuk, A. C., & Zemskova, A. M. (2015). Oxygen stable isotope variation in late holocene ice wedges in yamal peninsula and svalbard. *Geography, Environment, Sustainability*, *8*(3), 36–53. https://doi.org/10.24057/2071-9388-2015-8-3-36-54

Vasil'chuk, Y. K., Kim, J. C., & Vasil'chuk, A. C. (2004). AMS14C dating and stable isotope plots of Late Pleistocene ice-wedge ice. *Nuclear Instruments and Methods in Physics Research, Section B: Beam Interactions with Materials and Atoms*, *223–224*(SPEC. ISS.), 650–654. https://doi.org/10.1016/j.nimb.2004.04.120

Vasil'chuk, Y. K., Van Der Plicht, J., Jungner, H., Sonninen, E., & Vasil'chuk, A. C. (2000). First direct dating of Late Pleistocene ice-wedges by AMS. In *Earth and Planetary Science Letters* (Vol. 179). https://doi.org/10.1016/S0012-821X(00)00122-9

Vasil'chuk, Y. K., & Vasil'chuk, A. C. (2014). Spatial distribution of mean winter air temperatures in Siberian permafrost at 20-18 ka BP using oxygen isotope data. *Boreas*, *43*(3), 678–687. https://doi.org/10.1111/bor.12033

Vasil'chuk, Y. K., & Vasil'chuk, A. C. (2017). Validity of radiocarbon ages of Siberian yedoma. *GeoResJ*, *13*, 83–95. https://doi.org/10.1016/j.grj.2017.02.004

Vasil'chuk, Y. K., & Vasil'chuk, A. C. (2018). The Oxygen Isotope Composition of Ice Wedges of Ayon Island and Paleotemperature Reconstructions of the Late Pleistocene and Holocene of the Northern Chukotka. *Moscow University Geology Bulletin*, *73*(1), 87–99. https://doi.org/10.3103/S0145875218010131

Vasil'chuk, Y. K., Zaitsev, V. N., & Vasil'chuk, A. C. (2006). A 14C-dating and oxygen-isotope diagram of a Holocene-reformed ice wedge on the Chara River (Transbaikal region). *Doklady Earth Sciences*, *407*(1), 265–270. https://doi.org/10.1134/s1028334x06020267

Veillette, A., Fortier, D., & Godin, E. (2015). Contrasting patterns of thermo-erosion gullies formed in syngenetic ice wedge polygonal terrains on Bylot Island , eastern Canadian Arctic: case studies from three different

sedimentary environments. In *68th Canadian Geotechnical Conference and 7th Canadian Conference on Permafrost, 20-23 september 2015, Québec, Québec.*

Viau, A. E., & Gajewski, K. (2009). Reconstructing millennial-scale, regional paleoclimates of boreal Canada during the holocene. *Journal of Climate*, *22*(2), 316–330. https://doi.org/10.1175/2008JCLI2342.1

Ward Jones, M. K., Pollard, W. H., & Amyot, F. (2020). Impacts of Degrading Ice-Wedges on Ground Temperatures in a High Arctic Polar Desert System. *Journal of Geophysical Research: Earth Surface*, *125*(3). https://doi.org/10.1029/2019JF005173

Wooller, M. J., Zazula, G. D., Edwards, M., Froese, D. G., Boone, R. D., Parker, C., & Bennett, B. (2007). Stable carbon isotope compositions of Eastern Beringian grasses and sedges: Investigating their potential as paleoenvironmental indicators. *Arctic, Antarctic, and Alpine Research*, *39*(2), 318–331. https://doi.org/10.1657/1523-0430(2007)39[318:SCICOE]2.0.CO;2

Young, K. L., & Woo, M. K. (2000). Hydrological environment of the Hot Weather Creek basin, Ellesmere Island, Nunavut. *Bulletin of the Geological Survey of Canada*, (529), 347–360. https://doi.org/10.4095/211973

Zhang, Y., Chen, W., & Riseborough, D. W. (2008). Transient projections of permafrost distribution in Canada during the 21st century under scenarios of climate change. *Global and Planetary Change*, *60*(3–4), 443–456. https://doi.org/10.1016/j.gloplacha.2007.05.003

Appendices

Appendix A – R Code for ANOVA and Tukey's HSD analysis:
#Note: before conducting this code, ensure you have set your working directory.

W1<-file.choose() #choose a file

W<-read.csv(W1) %>% select(-Sample.name) %>% mutate(core=factor(Sample, ordered = TRUE)) #This line reads the file then removes unnecessary columns from the dataset then will order the data by whichever factor you choose. In this case, we wanted to order the data by core number.

levels(W$core) #shows you the different levels you have established.
attach(W)

W %>% group_by(core) %>% summarise(
count_core = n(),
mean_ = mean(CHOSEN COLUMN),
median_ = median(CHOSEN COLUMN),
sd_ = sd(CHOSEN COLUMN)) #Retrieve descriptive statistics

anova_one_way <- aov(CHOSEN COLUMN~core, data = W) #compute one-way ANOVA on chosen column, sort by chosen level, assign data location

summary(anova_one_way) #this function will recall the results of the one-way ANOVA test

TukeyHSD(anova_one_way, conf.level=0.95) #compute Tukey's HSD on ANOVA results

Appendix B – Data from C. Roy and D. Lacelle, July 2017

Lab ID	Sample ID	Location in IW	14C yr BP	+/-	F14C	+/-	median (cal yr BP)
UOC-6082	BT-IW1-centre	centre	5251	30	0.5201	0.002	5998
UOC-6088	BT-IW1-edge	edge	6480	38	0.4463	0.0021	7381
UOC-6084	BT-IW2-edge	edge	22043	117	0.0643	0.0009	26249
UOC-6080	BT-IW2-Centre	centre	28948	269	0.0272	0.0009	33131
UOC-6087	DS-IW2		14641	64	0.1616	0.0013	17823
UOC-6081	Gem-IW1-edge	edge	2624	28	0.7213	0.0025	2753
UOC-6090	Gem-IW2-centre	centre	2980	29	0.69	0.0025	3153
UOC-6086	Gem-IW2-edge	edge	4619	29	0.5627	0.002	5412
UOC-6083	MF-IW1-centre	centre	7296	47	0.4032	0.0024	8102
UOC-6085	MF-IW2-centre	centre	3047	29	0.6843	0.0025	3256
UOC-6089	MF-IW2-edge	edge	5237	34	0.521	0.0022	5981
UOC-6091	DS-1-95-134		12729	52	0.205	0.0013	15168

Appendix C – Results from Water Samples

		DOC		DIC		D/18O (δ, ‰)				
Sample Name	**Water Body**	**[DOC] (ppm)**	**δ DOC (‰)**	**[DIC] (ppm)**	**δ DIC (‰)**	**δ2H (‰)**	**δ2H(‰) StDev**	**δ18O(‰)**	**δ18O (‰) StDev**	**D-excess (‰)**
EU18-WS	pond	14.72	-27.14	35.60	-6.50	-177.76	0.56	-19.95	0.12	-18.12
EU18-WS	pond	8.59	-26.06	24.20	-5.20	-161.29	0.52	-16.44	0.12	-29.76
EU18-WS	pond	16.44	-29.23	44.00	-4.50	-170.49	0.19	-18.81	0.13	-20.01
EU18-WS	creek	1.84	-28.16	19.00	-0.50	-190.08	0.63	-23.90	0.12	1.15
EU18-WS	creek	2.21	-28.64	21.00	-0.10	-200.95	0.47	-25.35	0.11	1.88
EU18-WS	fjord	2.35	-27.61	9.80	-1.80	-103.96	0.64	-13.03	0.05	0.31
EU18-SB	snowbank	2.04	-26.83	5.40	-17.20	-251.02	1.45	-32.78	0.13	11.18
EU19-WS	fjord	1.96	-26.28			-71.70	1.37	-9.15	0.08	1.54

	Anions (ppm)			Cations (ppm)					
Sample Name	**Cl**	**SO4**	**NO3**	**Ca**	**Fe**	**K**	**Mg**	**Na**	**Sr**
EU18-WS	345.02	254.60	0.81	157.63	0.05	6.12	47.01	85.39	0.56
EU18-WS	225.46	144.32	0.56	98.73	0.04	5.24	27.14	57.18	0.36
EU18-WS	27.38	11.99	0.67	44.72	0.20	4.08	16.20	13.32	0.21
EU18-WS	17.41	107.86	1.07	33.33	0.04	1.66	13.62	13.44	0.11
EU18-WS	11.02	120.12	0.48	37.62	0.02	2.11	11.76	18.00	0.13
EU18-WS	1968.67	413.10	5.24	79.92	0.06	48.75	105.32	1284.56	0.74
EU18-SB	3.89	2.26	0.44	2.58	0.05	0.90	0.64	2.80	0.01
EU19-WS	4357.43	627.46	-0.06	109.64	0.00	120.95	287.06	2364.04	1.73

Appendix D – Results from Active layer samples

				Depth (cm)			Dissolved Organic Carbon		Soluble Anions (mg/L)		
Year Sampled	**Sample Name**	**Wedge Number**	**Sample number**	**Start**	**End**	**(measured) Gravimetric water content**	**[DOC] (ppm)**	**δ 13DOC (‰)**	**Cl**	**SO4**	**NO3**
2018	EU18-1-#1	1	1	57	60	8.33	14.16	-25.97	4.59	3.25	0.19
	EU18-1-#2		2	52	55	17.78	17.38	-25.01	7.47	6.81	2.37
	EU18-1-#3		3	47	50	17.52	19.02	-25.09	7.36	6.97	0.09
	EU18-1-#4		4	43	45	6.31	12.19	-25.40	4.43	3.01	0.46
	EU18-1-#5		5	37	40	11.60	19.56	-25.00	8.52	5.81	0.44
	EU18-1-#6		6	33	35	12.10	20.54	-24.93	8.52	6.33	0.20
	EU18-1-#7		7	27	30	16.96	22.13	-25.09	11.31	6.63	0.11
	EU18-1-#8		8	23	25	18.98	18.51	-23.98	20.98	10.17	0.32
	EU18-1-#9		9	17	20	18.14	20.17	-24.22	21.55	9.00	0.16
	EU18-1-#10		10	13	15	17.69	24.40	-24.06	23.90	9.56	0.28
	EU18-1-#11		11	7	10	14.68	26.44	-24.25	23.41	13.19	0.35
	EU18-1-#12		12	3	5	8.91	29.06	-24.86	24.92	15.09	1.27
2018	EU18-2-#1	2	1	69	70	17.39	15.07	-25.22	5.45	9.02	0.29
	EU18-2-#2		2	64	65	15.80	13.47	-24.88	0.14	0.24	0.02
	EU18-2-#3		3	59	60	17.73	15.11	-24.73	5.94	10.22	0.42
	EU18-2-#4		4	54	55	18.10	16.68	-25.11	7.26	9.52	0.69
	EU18-2-#5		5	49	50	17.46	16.12	-24.71	7.51	11.59	0.30
	EU18-2-#6		6	44	45	17.65	17.74	-24.78	11.10	11.59	0.04
	EU18-2-#7		7	39	40	17.64	20.10	-25.05	15.53	10.24	0.30
	EU18-2-#8		8	34	35	17.61	17.50	-24.68	46.43	15.17	1.23
	EU18-2-#9		9	29	30	15.96	16.39	-25.16	77.48	20.13	2.94
	EU18-2-#10		10	24	25	14.32	16.19	-25.25	67.85	23.21	4.40
	EU18-2-#11		11	19	20	16.07	18.72	-24.78	105.75	42.61	5.88
	EU18-2-#12		12	14	15	13.91	21.50	-25.08	77.53	40.30	0.32
	EU18-2-#13		13	9	10	10.49	29.63	-24.82	46.25	31.85	0.09
	EU18-2-#14		14	4	5	7.01	24.80	-24.65	91.96	70.58	1.88
	EU18-2-#15		15	0	0	7.15	29.77	-24.63	778.65	777.08	43.08

Continued…

	Soluble Cations (mg/L)						LOI				
Sample Name	**Ca**	**Fe**	**K**	**Mg**	**Na**	**Sr**	**Bulk Water %**	**Gravimetric Water %**	**Organics %**	**Carbonates %**	**Initial Mass**
EU18-1-#1	8.54	4.91	4.71	2.98	6.56	0.05	0.28	0.28	3.30	0.49	4.05
EU18-1-#2	15.89	1.47	6.28	4.13	10.33	0.07	0.28	0.28	7.54	1.72	4.01
EU18-1-#3	16.93	0.26	5.79	4.05	9.56	0.07	0.30	0.30	6.47	1.49	4.00
EU18-1-#4	10.18	2.65	4.20	2.76	5.67	0.05	0.24	0.24	2.81	0.56	4.09
EU18-1-#5	13.83	2.99	5.42	3.94	8.65	0.07	0.35	0.36	5.61	1.11	4.00
EU18-1-#6	15.38	0.90	5.00	3.86	8.12	0.07	0.42	0.43	6.94	1.35	4.01
EU18-1-#7	16.63	0.98	5.16	4.44	7.78	0.07	0.35	0.35	7.07	1.34	3.99
EU18-1-#8	20.71	0.18	5.60	5.44	9.96	0.09	0.45	0.45	7.74	1.61	4.08
EU18-1-#9	21.38	0.03	5.59	5.74	8.78	0.09	0.40	0.40	7.68	1.42	4.08
EU18-1-#10	20.45	-0.35	5.59	5.45	10.29	0.08	0.40	0.40	7.26	1.26	4.01
EU18-1-#11	16.05	1.21	6.03	4.76	12.41	0.07	0.48	0.48	6.93	1.13	3.99
EU18-1-#12	15.18	0.77	7.53	4.40	17.06	0.07	0.45	0.45	6.59	1.03	4.05
EU18-2-#1	8.93	7.71	7.78	4.02	28.18	0.06	0.50	0.50	5.90	1.90	4.08
EU18-2-#2	9.13	9.12	8.33	4.33	27.43	0.07	0.47	0.47	5.62	1.79	4.02
EU18-2-#3	8.87	5.61	7.60	3.46	28.51	0.06	0.46	0.46	5.87	1.96	4.06
EU18-2-#4	8.48	4.16	8.21	3.07	29.93	0.05	0.49	0.49	5.96	1.99	4.03
EU18-2-#5	9.83	7.18	8.41	4.29	29.22	0.07	0.47	0.47	5.63	1.94	3.97
EU18-2-#6	11.99	9.89	9.74	5.99	33.15	0.09	0.48	0.48	6.37	2.36	4.06
EU18-2-#7	11.51	11.77	10.24	5.97	33.42	0.09	0.83	0.84	6.06	2.20	4.02
EU18-2-#8	13.17	4.84	9.48	5.19	44.53	0.08	0.90	0.91	6.01	2.03	4.09
EU18-2-#9	13.64	2.34	8.82	5.20	59.13	0.07	0.80	0.81	5.38	1.55	4.02
EU18-2-#10	9.10	4.56	8.72	4.25	61.09	0.06	0.69	0.70	5.12	1.27	4.00
EU18-2-#11	11.56	8.22	9.88	6.18	98.96	0.08	0.78	0.78	5.66	1.45	4.02
EU18-2-#12	8.16	9.74	9.41	5.19	84.88	0.06	0.73	0.73	5.27	1.29	4.01
EU18-2-#13	9.57	19.72	10.89	7.65	73.90	0.10	0.76	0.77	5.38	1.28	4.04
EU18-2-#14	12.35	5.75	10.50	4.74	103.35	0.09	0.72	0.73	4.80	1.29	4.01
EU18-2-#15	212.03	-0.41	23.01	48.20	563.35	1.16	0.85	0.85	8.16	1.89	4.02

				Depth (cm)			Dissolved Organic Carbon		Soluble Anions (mg/L)		
Year Sampled	**Sample Name**	**Wedge Number**	**Sample number**	**Start**	**End**	**(measured) Gravimetric water content**	**[DOC] (ppm)**	**δ 13DOC (‰)**	**Cl**	**SO4**	**NO3**
2018	EU18-3-1	3	1	57	60	17.71	20.39	-24.52	11.23	11.82	0.21
	EU18-3-2		2	52	55	17.37	18.38	-24.64	12.89	11.56	0.00
	EU18-3-3		3	47	50	17.58	17.47	-24.65	8.57	6.86	0.29
	EU18-3-4		4	42	45	17.55	17.66	-24.57	9.38	6.89	0.00
	EU18-3-5		5	37	40	16.83	16.18	-24.68	17.93	8.42	0.35
	EU18-3-6		6	32	35	17.24	16.37	-24.56	8.90	5.47	0.00
	EU18-3-7		7	27	30	17.32	17.91	-24.70	9.29	5.52	0.25
	EU18-3-8		8	22	25	17.37	18.75	-24.61	9.26	5.48	0.32
	EU18-3-9		9	17	20	17.98	20.29	-24.63	14.14	6.58	0.28
	EU18-3-10		10	12	15	16.06	25.39	-24.72	13.83	7.33	0.41
	EU18-3-11		11	7	10	12.79	23.39	-25.29	21.88	15.18	0.15
	EU18-3-12		12	2	5	6.88	21.02	-25.51	36.74	18.70	1.63
	EU18-3-13		12	0	0	4.18	19.43	-26.27	301.70	122.91	0.17
2018	EU18-4-1	4	1	61	60	23.64	23.78	-24.89	29.47	31.18	0.28
	EU18-4-2		2	56	55	13.88	17.01	-25.18	7.22	8.86	0.05
	EU18-4-3		3	51	50	11.85	17.88	-25.56	4.88	4.72	0.26
	EU18-4-4		4	46	45	14.13	19.15	-25.48	4.95	4.20	0.14
	EU18-4-5		5	41	40	11.85	16.55	-25.41	3.78	3.37	0.88
	EU18-4-6		6	36	35	12.37	18.13	-25.44	3.62	2.25	0.21
	EU18-4-7		7	31	30	12.38	21.22	-26.13	2.43	2.49	0.54
	EU18-4-8		8	26	25	13.46	22.24	-24.64	4.40	4.80	0.09
	EU18-4-9		9	21	20	12.89	22.71	-25.21	2.82	3.29	0.57
	EU18-4-10		10	16	15	9.99	18.41	-24.82	3.14	3.12	0.37
	EU18-4-11		11	11	10	10.19	22.01	-24.50	2.93	2.53	0.16
	EU18-4-12		12	6	5	8.87	28.55	-26.11	1.54	1.55	0.35
	EU18-4-13		13	1	0	4.00	38.41	-26.12	3.52	3.85	0.10

Continued…

	Soluble Cations (mg/L)						LOI				
Sample Name	**Ca**	**Fe**	**K**	**Mg**	**Na**	**Sr**	**Bulk Water %**	**Gravimetric Water %**	**Organics %**	**Carbonates %**	**Initial Mass**
EU18-3-1	12.84	20.62	9.91	7.07	26.02	0.11	12.84	0.97	0.98	6.71	1.46
EU18-3-2	11.41	11.62	8.38	5.41	22.27	0.09	11.41	1.12	1.14	6.96	1.47
EU18-3-3	12.91	3.97	6.93	4.47	16.10	0.08	12.91	0.93	0.94	6.61	1.60
EU18-3-4	14.49	4.92	7.47	5.04	14.26	0.09	14.49	0.89	0.90	6.23	1.56
EU18-3-5	16.28	2.76	6.55	5.12	12.65	0.09	16.28	0.94	0.95	5.74	1.42
EU18-3-6	17.13	7.52	6.89	5.63	9.63	0.10	17.13	0.77	0.77	5.79	1.53
EU18-3-7	15.10	2.14	5.95	4.07	8.74	0.08	15.10	0.81	0.82	5.83	1.57
EU18-3-8	14.59	3.54	5.94	4.03	8.40	0.08	14.59	0.94	0.94	6.32	1.49
EU18-3-9	15.82	1.12	5.76	4.08	8.88	0.08	15.82	0.94	0.95	6.26	1.46
EU18-3-10	17.41	0.56	6.07	4.12	10.40	0.08	17.41	0.92	0.92	5.97	1.44
EU18-3-11	20.65	0.52	5.97	4.78	12.18	0.10	20.65	0.84	0.85	5.27	1.32
EU18-3-12	22.56	-0.25	7.01	5.38	17.91	0.10	22.56	0.86	0.86	5.26	1.21
EU18-3-13	84.80	-0.42	16.07	26.48	110.25	0.43	84.80	0.89	0.90	5.62	1.16
EU18-4-1	11.11	3.65	7.89	7.78	25.42	0.07	11.11	0.77	0.78	4.84	0.94
EU18-4-2	10.03	2.23	5.05	4.40	11.36	0.05	10.03	0.41	0.41	2.49	0.59
EU18-4-3	5.79	1.25	4.07	2.47	9.18	0.03	5.79	0.38	0.38	2.01	0.62
EU18-4-4	4.97	0.91	4.04	2.12	9.99	0.03	4.97	0.48	0.48	2.94	0.63
EU18-4-5	5.00	2.26	4.15	2.12	8.64	0.03	5.00	0.37	0.37	2.40	0.56
EU18-4-6	4.71	2.28	4.16	2.06	8.12	0.03	4.71	0.43	0.43	2.37	0.54
EU18-4-7	4.07	0.74	3.61	1.52	8.09	0.02	4.07	0.45	0.45	2.65	0.52
EU18-4-8	5.34	1.91	4.18	2.61	9.88	0.03	5.34	0.57	0.57	3.70	0.65
EU18-4-9	4.90	3.02	4.04	2.41	9.19	0.03	4.90	0.37	0.37	3.42	0.73
EU18-4-10	4.80	3.18	3.73	2.40	8.54	0.03	4.80	0.36	0.36	3.37	0.72
EU18-4-11	5.73	5.14	4.11	3.03	9.44	0.04	5.73	0.37	0.37	3.19	0.90
EU18-4-12	5.83	1.64	4.00	2.31	10.32	0.03	5.83	0.40	0.40	4.10	0.75
EU18-4-13	7.69	2.53	6.99	2.80	13.16	0.04	7.69	0.47	0.47	4.76	0.74

			Depth (cm)			Dissolved Organic Carbon		Soluble Anions (mg/L)		
Year Sampled	**Sample Name**	**Wedge Number**	**Start**	**End**	**(measured) Gravimetric water content**	**[DOC] (ppm)**	**δ 13DOC (‰)**	**Cl**	**SO4**	**NO3**
2019	MF1-W3- AL	3	0	5	10.51	53.36	-24.55			
	MF1-W3- AL		5	10	18.91	68.91	-23.97			
	MF1-W3- AL		10	15	20.43	64.66	-24.44	16.08	15.63	0.02
	MF1-W3- AL		15	20	21.15	61.72	-24.52	12.98	13.41	0.05
	MF1-W3- AL		20	25	20.83	60.16	-24.04			
	MF1-W3- AL		25	30	21.02	71.93	-23.99	16.65	12.05	0.02
	MF1-W3- AL		30	35	20.81	60.92	-24.28			
	MF1-W3- AL		35	40	34.33	115.80	-25.66	51.53	22.22	0.04
	MF1-W3- AL		40	45	39.19	117.50	-25.46	80.47	24.34	0.12
	MF1-W3- AL		45	50	34.19	67.38	-24.87	41.27	16.65	0.07
2019	MF1-W2-AL	2	0	5	8.58	59.33	-24.81			
	MF1-W2-AL		5	10	20.28	85.17	-24.79	81.28	59.30	0.05
	MF1-W2-AL		10	15	23.49	84.74	-24.59			
	MF1-W2-AL		15	20	25.06	87.50	-25.06	10.16	12.64	0.03
	MF1-W2-AL		20	25	25.80	84.49	-24.79			
	MF1-W2-AL		25	30	27.75	103.90	-25.38			
	MF1-W2-AL		30	35	27.96	116.10	-26.09			
	MF1-W2-AL		35	40	41.17	141.60	-25.78			
	MF1-W2-AL		40	45	41.03	120.50	-26.38			
2019	EU19-W5-AL	5	0	5	13.19	120.70	-25.17			
	EU19-W5-AL		5	10	23.17	106.80	-24.47			
	EU19-W5-AL		10	15	29.83	119.00	-24.81	70.50	81.99	0.13
	EU19-W5-AL		15	20	32.28	94.90	-24.50			
	EU19-W5-AL		20	25	28.40	78.59	-24.87	45.89	49.50	0.13
	EU19-W5-AL		25	30	22.31	49.65	-24.44	28.51	30.80	0.11
	EU19-W5-AL		30	35	20.38	30.92	-24.86	22.24	21.51	0.00
	EU19-W5-AL		35	40	21.86	26.40	-23.94			
	EU19-W5-AL		40	45	22.93	45.15	-24.21	14.28	15.02	0.07
	EU19-W5-AL		45	50	22.60	38.16	-24.71	13.43	16.24	0.01
	EU19-W5-AL		50	55	23.65	36.25	-24.04			
	EU19-W5-AL		55	60	24.41	37.65	-23.65			

Continued…

	Soluble Cations (mg/L)						LOI				
Sample Name	**Ca**	**Fe**	**K**	**Mg**	**Na**	**Sr**	**Bulk Water %**	**Gravimetric Water %**	**Organics %**	**Carbonates %**	**Initial Mass**
MF1-W3- AL							0.50	0.51	8.14	0.91	5.06
MF1-W3- AL							0.58	0.59	8.45	0.93	4.99
MF1-W3- AL	19.72	2.61	2.65	5.64	13.51	0.12	0.68	0.69	8.44	0.96	5.00
MF1-W3- AL	18.22	1.76	2.06	5.26	11.00	0.10	0.69	0.69	8.61	0.98	5.05
MF1-W3- AL							0.69	0.70	8.52	0.97	4.97
MF1-W3- AL	20.17	2.98	2.43	6.23	9.56	0.11	0.85	0.86	8.70	0.90	4.98
MF1-W3- AL							0.82	0.82	8.84	0.92	5.08
MF1-W3- AL	46.23	0.31	2.19	17.28	9.07	0.23	0.53	0.54	18.10	1.52	5.03
MF1-W3- AL	53.62	0.11	2.73	23.34	7.38	0.29	0.76	0.76	15.60	1.28	5.00
MF1-W3- AL	30.22	0.08	2.61	12.37	5.36	0.16	1.44	1.46	11.14	1.02	5.02
MF1-W2-AL							0.69	0.69	9.39	1.04	5.00
MF1-W2-AL	35.43	0.45	3.36	11.77	50.70	0.20	0.97	0.98	10.31	0.91	5.02
MF1-W2-AL							1.18	1.20	10.53	0.97	5.08
MF1-W2-AL	18.14	1.48	1.79	5.94	12.76	0.09	0.68	0.69	10.48	0.98	4.98
MF1-W2-AL							0.54	0.54	10.60	0.98	5.05
MF1-W2-AL							0.77	0.78	11.71	1.06	5.02
MF1-W2-AL							0.99	1.00	11.98	1.04	5.02
MF1-W2-AL							1.43	1.45	16.05	1.30	5.04
MF1-W2-AL							1.18	1.19	14.56	1.13	5.07
EU19-W5-AL							0.47	0.47	10.74	0.76	5.01
EU19-W5-AL							0.57	0.58	11.60	0.78	5.01
EU19-W5-AL	10.35	3.98	9.18	7.33	142.72	0.07	0.59	0.59	16.04	0.85	4.99
EU19-W5-AL							0.41	0.41	17.14	0.92	5.01
EU19-W5-AL	8.52	5.13	7.25	6.94	89.61	0.07	0.47	0.48	13.93	0.85	5.02
EU19-W5-AL	6.89	7.13	6.40	6.19	52.00	0.06	0.50	0.51	8.72	0.80	4.98
EU19-W5-AL	5.97	4.12	6.29	5.52	34.18	0.05	0.83	0.83	6.55	0.96	5.00
EU19-W5-AL							0.46	0.46	7.30	0.86	4.96
EU19-W5-AL	7.18	5.09	7.58	6.52	30.51	0.06	0.58	0.58	9.63	0.82	5.01
EU19-W5-AL	6.89	3.42	7.13	6.10	28.36	0.05	0.63	0.63	8.88	0.79	5.06
EU19-W5-AL							0.45	0.46	8.81	0.77	4.97
EU19-W5-AL							0.44	0.44	9.84	0.78	4.99

Appendix E – Results from Horizontal Ice Wedges

WEDGE 1:

Sample Name	δ2H (‰)	δ2H (‰) StDev	δ18O (‰)	δ 18O (‰) StDev	D-excess	IW position (Top - 1; Middle - 2; Bottom -3)	Distance from centre (cm)	Permafrost (Y/N)
EU18-W1-1	-204.2	0.4	-25.4	0.1	-1.0	1	-33	Y
EU18-W1-2	-195.7	0.2	-24.2	0.1	-2.5	1	-32	Y
EU18-W1-3	-188.3	0.9	-23.2	0.1	-3.0	1	-31	Y
EU18-W1-4	-183.2	0.1	-22.6	0.2	-2.7	1	-30	Y
EU18-W1-5	-181.3	0.7	-22.2	0.2	-3.9	1	-29	Y
EU18-W1-6	-179.7	0.1	-21.9	0.0	-4.7	1	-28	Y
EU18-W1-7	-180.7	0.2	-22.3	0.1	-2.5	1	-27	Y
EU18-W1-8	-178.9	0.6	-21.6	0.2	-6.1	1	-26	Y
EU18-W1-9	-179.5	0.2	-22.2	0.1	-2.2	1	-25	Y
EU18-W1-10	-179.9	0.9	-22.4	0.2	-0.9	1	-24	Y
EU18-W1-11	-179.3	0.4	-22.0	0.1	-3.5	1	-23	Y
EU18-W1-12	-178.0	0.4	-21.8	0.1	-3.9	1	-22	Y
EU18-W1-13	-174.6	0.2	-20.6	0.1	-9.4	1	-21	Y
EU18-W1-14	-223.1	0.5	-28.3	0.1	3.5	1	-20	N
EU18-W1-15	-227.2	0.2	-28.1	0.2	-2.2	1	-19	N
EU18-W1-16	-231.2	0.5	-28.7	0.1	-1.7	1	-18	N
EU18-W1-17	-227.3	0.3	-27.7	0.1	-5.9	1	-17	N
EU18-W1-18	-227.3	0.5	-28.3	0.1	-0.6	1	-16	N
EU18-W1-19	-228.7	0.3	-28.6	0.1	0.4	1	-15	N
EU18-W1-20	-228.9	0.4	-28.9	0.0	2.1	1	-14	N
EU18-W1-21	-227.9	0.6	-28.5	0.1	0.2	1	-13	N
EU18-W1-22	-230.0	0.2	-28.8	0.1	0.5	1	-12	N
EU18-W1-23	-232.3	0.3	-29.0	0.2	-0.6	1	-11	N
EU18-W1-24	-235.2	0.3	-29.3	0.1	-1.0	1	-10	N
EU18-W1-25	-236.7	0.4	-29.4	0.1	-1.9	1	-9	N
EU18-W1-26	-237.1	0.2	-29.3	0.1	-2.5	1	-8	N
EU18-W1-27	-246.6	0.2	-31.4	0.1	4.5	1	-7	N
EU18-W1-28	-250.2	0.3	-31.6	0.0	2.5	1	-6	N
EU18-W1-29	-244.0	0.2	-31.0	0.1	4.0	1	-5	N

Sample Name	δ2H (‰)	δ2H (‰) StDev	δ18O (‰)	δ 18O (‰) StDev	D-excess	IW position (Top - 1; Middle - 2; Bottom -3)	Distance from centre (cm)	Permafrost (Y/N)
EU18-W1-30	-240.5	0.4	-30.5	0.2	3.5	1	-4	N
EU18-W1-31	-237.9	0.3	-30.2	0.2	3.9	1	-3	N
EU18-W1-32	-243.4	0.6	-30.9	0.1	4.2	1	-2	N
EU18-W1-33	-246.1	0.3	-31.4	0.0	4.9	1	-1	N
EU18-W1-34	-249.3	0.6	-31.8	0.1	4.7	1	0	N
EU18-W1-35	-246.3	0.3	-31.2	0.1	3.6	1	1	N
EU18-W1-36	-241.7	0.2	-30.6	0.1	2.9	1	2	N
EU18-W1-37	-244.9	0.5	-31.2	0.2	4.4	1	3	N
EU18-W1-38	-251.2	0.1	-32.0	0.1	4.9	1	4	N
EU18-W1-39	-243.4	0.4	-31.0	0.2	4.2	1	5	N
EU18-W1-40	-238.5	0.3	-30.2	0.2	3.0	1	6	N
EU18-W1-41	-234.3	0.2	-29.9	0.1	4.9	1	7	N
EU18-W1-42	-240.4	0.4	-30.6	0.1	4.1	1	8	N
EU18-W1-43	-211.9	0.1	-26.3	0.2	-1.6	2	-34	Y
EU18-W1-44	-202.2	0.7	-24.9	0.1	-2.9	2	-33	Y
EU18-W1-45	-192.2	0.5	-23.4	0.1	-5.2	2	-32	Y
EU18-W1-46	-190.8	0.3	-23.7	0.1	-1.4	2	-31	Y
EU18-W1-47	-190.3	0.6	-23.5	0.1	-2.2	2	-30	Y
EU18-W1-48	-189.4	0.1	-23.7	0.2	0.0	2	-29	Y
EU18-W1-49	-188.7	0.6	-23.5	0.2	-1.0	2	-28	Y
EU18-W1-50	-188.2	0.5	-23.3	0.2	-1.5	2	-27	Y
EU18-W1-51	-188.3	0.3	-23.8	0.1	2.2	2	-26	Y
EU18-W1-52	-187.1	0.4	-23.6	0.2	1.5	2	-25	Y
EU18-W1-53	-187.0	0.4	-23.3	0.1	-0.2	2	-24	Y
EU18-W1-54	-185.8	0.4	-23.2	0.1	0.1	2	-23	Y
EU18-W1-55	-198.5	0.5	-25.0	0.1	1.7	2	-22	Y
EU18-W1-56	-208.0	0.6	-26.4	0.1	3.2	2	-21	Y
EU18-W1-57	-230.2	0.3	-29.4	0.0	5.4	2	-20	N
EU18-W1-58	-227.1	0.2	-29.1	0.1	5.4	2	-19	N
EU18-W1-59	-228.4	0.3	-29.2	0.1	5.4	2	-18	N
EU18-W1-60	-230.6	0.4	-29.6	0.1	6.0	2	-17	N
EU18-W1-61	-229.7	0.3	-29.0	0.2	2.2	2	-16	N

Sample Name	δ2H (‰)	δ2H (‰) StDev	δ18O (‰)	δ 18O (‰) StDev	D-excess	IW position (Top - 1; Middle - 2; Bottom -3)	Distance from centre (cm)	Permafrost (Y/N)
EU18-W1-62	-232.8	0.3	-29.3	0.1	1.9	2	-15	N
EU18-W1-63	-232.9	0.2	-29.2	0.2	0.7	2	-14	N
EU18-W1-64	-230.9	0.2	-28.6	0.1	-2.0	2	-13	N
EU18-W1-65	-230.1	0.5	-28.2	0.2	-4.6	2	-12	N
EU18-W1-66	-237.4	0.6	-30.4	0.1	5.8	2	-11	N
EU18-W1-67	-238.2	0.3	-30.4	0.1	4.8	2	-10	N
EU18-W1-68	-238.3	0.4	-30.4	0.0	4.7	2	-9	N
EU18-W1-69	-234.2	0.3	-29.7	0.2	3.1	2	-8	N
EU18-W1-70	-232.0	0.4	-29.4	0.2	2.8	2	-7	N
EU18-W1-71	-228.2	0.1	-28.9	0.1	3.4	2	-6	N
EU18-W1-72	-237.8	0.3	-30.4	0.1	5.8	2	-5	N
EU18-W1-73	-236.6	0.2	-30.4	0.0	6.7	2	-4	N
EU18-W1-74	-240.3	0.1	-30.8	0.0	6.2	2	-3	N
EU18-W1-75	-246.0	0.3	-31.6	0.2	6.7	2	-2	N
EU18-W1-76	-245.6	0.6	-31.3	0.0	5.0	2	-1	N
EU18-W1-77	-244.0	0.1	-31.3	0.0	6.2	2	0	N
EU18-W1-78	-238.3	0.4	-30.4	0.1	4.6	2	1	N
EU18-W1-79	-244.0	0.2	-31.1	0.1	4.4	2	2	N
EU18-W1-80	-243.8	0.4	-30.9	0.1	3.5	2	3	N
EU18-W1-81	-243.9	0.7	-30.9	0.1	3.6	2	4	N
EU18-W1-82	-242.9	0.4	-30.9	0.1	4.4	2	5	N
EU18-W1-83	-236.2	0.2	-29.9	0.1	2.6	2	6	N
EU18-W1-84	-237.1	0.1	-30.1	0.1	3.6	2	7	N
EU18-W1-85	-243.7	0.2	-31.0	0.1	4.2	2	8	N
EU18-W1-86	-245.1	0.3	-31.4	0.1	5.8	2	9	N
EU18-W1-87	-245.8	0.4	-31.3	0.1	4.8	2	10	N
EU18-W1-88	-246.4	0.3	-31.9	0.1	8.8	2	11	N
EU18-W1-89	-246.6	0.2	-31.7	0.1	7.0	2	12	N
EU18-W1-90	-244.9	0.2	-31.9	0.2	10.5	2	13	N
EU18-W1-91	-244.7	0.5	-31.2	0.1	4.9	2	14	N
EU18-W1-92	-242.0	0.1	-30.9	0.0	5.0	2	15	N
EU18-W1-93	-247.7	0.2	-31.8	0.1	6.8	2	16	N
EU18-W1-94	-251.1	0.1	-32.3	0.1	7.6	2	17	N

Sample Name	δ2H (‰)	δ2H (‰) StDev	δ18O (‰)	δ 18O (‰) StDev	D-excess	IW position (Top - 1; Middle - 2; Bottom -3)	Distance from centre (cm)	Permafrost (Y/N)
EU18-W1-95	-254.0	0.4	-32.7	0.0	7.8	2	18	N
EU18-W1-96	-254.1	0.4	-32.1	0.1	2.6	2	19	N
EU18-W1-97	-240.7	0.2	-30.8	0.1	5.8	2	20	N
EU18-W1-98	-236.9	0.1	-30.3	0.0	5.4	2	21	N
EU18-W1-99	-252.6	0.5	-32.7	0.2	9.0	2	22	N
EU18-W1-100	-248.8	0.3	-32.5	0.2	11.1	2	23	N
EU18-W1-101	-244.9	0.1	-31.2	0.1	4.9	2	24	N
EU18-W1-102	-248.5	0.2	-31.8	0.1	5.6	2	25	N
EU18-W1-103	-244.1	0.4	-31.1	0.2	4.4	2	26	N
EU18-W1-104	-187.5	0.4	-24.2	0.1	5.8	3	-62	Y
EU18-W1-105	-185.0	0.3	-24.1	0.2	7.6	3	-61	Y
EU18-W1-106	-184.6	0.1	-23.8	0.1	5.7	3	-60	Y
EU18-W1-107	-183.9	0.3	-23.7	0.2	5.3	3	-59	Y
EU18-W1-108	-183.6	0.3	-23.6	0.1	5.2	3	-58	Y
EU18-W1-109	-183.3	0.4	-23.4	0.1	4.1	3	-57	Y
EU18-W1-110	-183.4	0.3	-23.5	0.1	5.0	3	-56	Y
EU18-W1-111	-184.1	0.1	-23.8	0.1	6.1	3	-55	Y
EU18-W1-112	-184.0	0.3	-23.8	0.1	6.1	3	-54	Y
EU18-W1-113	-184.9	0.4	-24.1	0.1	7.7	3	-53	Y
EU18-W1-114	-184.7	0.1	-24.1	0.1	8.4	3	-52	Y
EU18-W1-115	-185.2	0.3	-24.1	0.1	7.8	3	-51	Y
EU18-W1-116	-185.2	0.3	-23.8	0.1	5.0	3	-50	Y
EU18-W1-117	-184.6	0.4	-23.6	0.1	4.5	3	-49	Y
EU18-W1-118	-184.3	0.5	-23.6	0.1	4.7	3	-48	Y
EU18-W1-119	-184.7	0.3	-23.5	0.1	3.4	3	-47	Y
EU18-W1-120	-183.9	0.5	-23.4	0.3	3.6	3	-46	Y
EU18-W1-121	-184.8	0.2	-23.5	0.1	3.6	3	-45	Y
EU18-W1-122	-184.0	0.2	-23.5	0.0	3.8	3	-44	Y
EU18-W1-123	-187.2	0.3	-24.1	0.1	5.7	3	-43	Y
EU18-W1-124	-187.2	0.1	-24.2	0.1	6.0	3	-42	Y
EU18-W1-125	-186.9	0.4	-24.0	0.2	5.0	3	-41	Y
EU18-W1-126	-186.4	0.5	-23.8	0.1	3.8	3	-40	Y
EU18-W1-127	-185.5	0.2	-23.9	0.1	5.4	3	-39	Y

Sample Name	δ2H (‰)	δ2H (‰) StDev	δ18O (‰)	δ 18O (‰) StDev	D-excess	IW position (Top - 1; Middle - 2; Bottom -3)	Distance from centre (cm)	Permafrost (Y/N)
EU18-W1-128	-185.9	0.3	-23.9	0.1	5.5	3	-38	Y
EU18-W1-129	-184.9	0.2	-23.7	0.1	4.9	3	-37	Y
EU18-W1-130	-184.7	0.2	-23.7	0.2	5.0	3	-36	Y
EU18-W1-131	-184.1	0.2	-23.3	0.2	2.4	3	-35	Y
EU18-W1-132	-183.7	0.3	-23.3	0.1	2.4	3	-34	Y
EU18-W1-133	-183.8	0.3	-23.1	0.2	0.7	3	-33	Y
EU18-W1-134	-183.9	0.3	-22.6	0.1	-3.2	3	-32	Y
EU18-W1-135	-182.8	0.5	-22.4	0.1	-3.7	3	-31	Y
EU18-W1-136	-189.5	0.4	-24.2	0.1	4.3	3	-30	Y
EU18-W1-137	-189.4	0.0	-24.0	0.0	2.5	3	-29	Y
EU18-W1-138	-190.4	0.2	-24.0	0.2	1.7	3	-28	Y
EU18-W1-139	-191.2	0.3	-24.2	0.0	2.5	3	-27	Y
EU18-W1-140	-193.8	0.3	-24.6	0.1	2.7	3	-26	Y
EU18-W1-141	-196.9	0.2	-25.1	0.1	3.8	3	-25	Y
EU18-W1-142	-202.2	0.2	-25.1	0.2	-1.4	3	-24	Y
EU18-W1-143	-206.3	0.2	-25.7	0.1	-0.5	3	-23	Y
EU18-W1-144	-214.8	0.5	-27.1	0.1	1.9	3	-22	Y
EU18-W1-145	-226.2	0.6	-28.9	0.1	4.8	3	-21	N
EU18-W1-146	-230.5	0.4	-29.1	0.1	2.5	3	-20	N
EU18-W1-147	-242.7	0.3	-30.8	0.1	3.4	3	-19	N
EU18-W1-148	-244.3	0.1	-31.2	0.1	5.2	3	-18	N
EU18-W1-149	-244.8	0.2	-31.4	0.2	6.7	3	-17	N
EU18-W1-150	-244.2	0.3	-31.5	0.1	7.6	3	-16	N
EU18-W1-151	-240.2	0.4	-30.9	0.1	6.7	3	-15	N
EU18-W1-152	-245.0	0.3	-31.6	0.1	8.1	3	-14	N
EU18-W1-153	-243.3	0.2	-31.3	0.1	7.3	3	-13	N
EU18-W1-154	-246.4	0.1	-31.9	0.1	9.0	3	-12	N
EU18-W1-155	-242.2	0.4	-31.8	0.1	12.0	3	-11	N
EU18-W1-156	-234.8	0.5	-30.0	0.1	4.9	3	-10	N
EU18-W1-157	-235.1	0.2	-30.0	0.1	4.8	3	-9	N
EU18-W1-158	-240.8	0.3	-30.6	0.1	4.1	3	-8	N
EU18-W1-159	-243.8	0.3	-31.1	0.0	5.3	3	-7	N
EU18-W1-160	-243.1	0.4	-31.2	0.1	6.5	3	-6	N

Sample Name	δ2H (‰)	δ2H (‰) StDev	δ18O (‰)	δ 18O (‰) StDev	D-excess	IW position (Top - 1; Middle - 2; Bottom -3)	Distance from centre (cm)	Permafrost (Y/N)
EU18-W1-161	-240.9	0.3	-30.7	0.1	4.6	3	-5	N
EU18-W1-162	-240.8	0.1	-30.5	0.2	3.4	3	-4	N
EU18-W1-163	-240.0	0.3	-30.3	0.1	2.6	3	-3	N
EU18-W1-164	-236.5	0.3	-30.1	0.1	4.0	3	-2	N
EU18-W1-165	-233.9	0.7	-29.9	0.1	5.0	3	-1	N
EU18-W1-166	-238.6	0.5	-30.3	0.1	4.2	3	0	N
EU18-W1-167	-243.7	0.5	-31.0	0.1	4.3	3	1	N
EU18-W1-168	-245.9	0.4	-31.2	0.1	3.9	3	2	N
EU18-W1-169	-246.6	0.7	-31.3	0.0	4.2	3	3	N
EU18-W1-170	-255.7	0.1	-32.5	0.1	4.5	3	4	N
EU18-W1-171	-242.6	0.3	-31.0	0.1	5.2	3	5	N
EU18-W1-172	-240.5	0.2	-30.6	0.1	4.1	3	6	N
EU18-W1-173	-248.9	0.7	-31.8	0.2	5.4	3	7	N
EU18-W1-174	-249.7	0.6	-31.6	0.1	3.5	3	8	N
EU18-W1-175	-242.5	0.3	-30.8	0.1	3.8	3	9	N
EU18-W1-176	-245.9	0.5	-31.2	0.1	3.5	3	10	N
EU18-W1-177	-243.5	0.3	-31.0	0.2	4.2	3	11	N
EU18-W1-178	-243.6	0.5	-30.8	0.1	3.2	3	12	N
EU18-W1-179	-240.1	0.2	-30.5	0.0	4.1	3	13	N
EU18-W1-180	-243.2	0.2	-30.8	0.1	3.6	3	14	N
EU18-W1-181	-244.7	0.8	-31.3	0.1	5.5	3	15	N
EU18-W1-182	-242.4	0.5	-30.6	0.1	2.7	3	16	N
EU18-W1-183	-221.7	0.3	-27.9	0.1	1.1	3	17	Y
EU18-W1-184	-229.9	0.3	-29.0	0.1	2.2	3	18	Y
EU18-W1-185	-230.9	0.4	-29.1	0.0	1.6	3	19	Y
EU18-W1-186	-229.6	0.5	-29.2	0.1	4.3	3	20	Y
EU18-W1-187	-228.2	0.1	-29.0	0.1	4.2	3	21	Y
EU18-W1-188	-226.8	0.8	-28.6	0.1	2.4	3	22	Y
EU18-W1-189	-229.6	0.5	-29.0	0.1	2.5	3	23	Y
EU18-W1-190	-230.8	0.4	-29.2	0.2	2.7	3	24	Y
EU18-W1-191	-230.1	0.4	-28.7	0.1	-0.2	3	25	Y

WEDGE 2:

Sample Name	δ2H (‰)	δ2H (‰) StDev	δ18O (‰)	δ 18O (‰) StDev	D-excess	IW position (Top - 1; Middle - 2)	Distance from centre (cm)	Permafrost (Y/N)
EU18-W2-1	-240.4	0.6	-29.9	0.1	-1.6	2	19	Y
EU18-W2-2	-245.8	0.1	-30.8	0.1	0.7	2	18	N
EU18-W2-3	-246.5	0.5	-31.0	0.0	1.2	2	17	N
EU18-W2-4	-246.9	0.3	-31.1	0.1	2.0	2	16	N
EU18-W2-5	-247.5	0.4	-31.3	0.1	3.1	2	15	N
EU18-W2-6	-246.0	1.5	-31.1	0.2	2.5	2	14	N
EU18-W2-7	-246.8	0.5	-31.2	0.1	2.9	2	13	N
EU18-W2-8	-247.5	0.3	-31.3	0.1	3.1	2	12	N
EU18-W2-9	-247.2	0.2	-31.4	0.0	4.0	2	11	N
EU18-W2-10	-247.3	0.6	-31.4	0.2	3.9	2	10	N
EU18-W2-11	-244.4	0.3	-30.9	0.0	3.1	2	9	N
EU18-W2-12	-246.5	0.3	-31.3	0.1	4.0	2	8	N
EU18-W2-13	-247.6	0.1	-31.5	0.1	4.8	2	7	N
EU18-W2-14	-247.4	0.4	-31.7	0.1	5.8	2	6	N
EU18-W2-15	-247.7	1.0	-31.7	0.2	5.8	2	5	N
EU18-W2-16	-245.0	0.8	-31.3	0.1	5.2	2	4	N
EU18-W2-17	-246.2	0.4	-31.4	0.1	5.1	2	3	N
EU18-W2-18	-245.8	0.3	-31.2	0.1	3.6	2	2	N
EU18-W2-19	-245.2	0.2	-31.1	0.1	3.5	2	1	N
EU18-W2-20	-245.2	0.6	-31.2	0.0	4.5	2	0	N
EU18-W2-21	-244.1	0.7	-30.9	0.1	3.2	2	-1	N
EU18-W2-22	-244.5	0.4	-31.1	0.1	4.6	2	-2	N
EU18-W2-23	-243.8	0.5	-30.8	0.1	2.5	2	-3	N
EU18-W2-24	-245.3	0.1	-31.0	0.1	2.8	2	-4	N
EU18-W2-25	-245.2	0.3	-31.0	0.0	2.8	2	-5	N
EU18-W2-26	-243.8	0.5	-31.0	0.1	4.1	2	-6	N
EU18-W2-27	-244.7	0.4	-31.1	0.1	3.8	2	-7	N
EU18-W2-28	-245.8	0.4	-31.3	0.1	4.9	2	-8	N
EU18-W2-29	-245.9	0.1	-31.4	0.1	4.9	2	-9	N
EU18-W2-30	-246.3	0.4	-31.4	0.1	4.6	2	-10	N
EU18-W2-31	-245.3	0.4	-31.2	0.1	4.1	2	-11	N

Sample Name	δ2H (‰)	δ2H (‰) StDev	δ18O (‰)	δ 18O (‰) StDev	D-excess	IW position (Top - 1; Middle – 2; Bottom - 3)	Distance from centre (cm)	Permafrost (Y/N)
EU18-W2-32	-245.2	0.5	-31.2	0.1	4.1	2	-12	N
EU18-W2-33	-245.5	0.4	-31.1	0.0	3.4	2	-13	N
EU18-W2-34	-246.1	0.4	-31.1	0.2	2.4	2	-14	N
EU18-W2-35	-246.6	0.5	-31.2	0.1	3.1	2	-15	N
EU18-W2-36	-245.6	0.4	-31.2	0.1	3.9	2	-16	N
EU18-W2-37	-246.0	0.2	-31.3	0.1	4.4	2	-17	N
EU18-W2-38	-246.7	0.2	-31.4	0.0	4.2	2	-18	N
EU18-W2-39	-246.1	0.4	-31.3	0.1	4.0	2	-19	N
EU18-W2-40	-244.2	0.1	-30.7	0.0	1.5	2	-20	Y
EU18-W2-41	-245.8	0.1	-31.1	0.0	2.6	3	9	Y
EU18-W2-42	-249.3	0.1	-31.8	0.0	5.2	3	8	N
EU18-W2-43	-247.3	0.2	-31.3	0.2	3.4	3	7	N
EU18-W2-44	-248.5	0.6	-31.6	0.1	3.9	3	6	N
EU18-W2-45	-248.9	0.3	-31.7	0.1	4.4	3	5	N
EU18-W2-46	-247.1	0.4	-31.3	0.1	3.6	3	4	N
EU18-W2-47	-248.6	0.8	-31.6	0.0	4.4	3	3	N
EU18-W2-48	-248.5	0.4	-31.4	0.3	3.0	3	2	N
EU18-W2-49	-248.4	0.4	-31.5	0.1	3.2	3	1	N
EU18-W2-50	-248.5	0.6	-31.4	0.1	2.8	3	0	N
EU18-W2-51	-247.1	0.6	-31.6	0.1	5.5	3	-1	N
EU18-W2-52	-248.1	0.1	-31.6	0.1	4.5	3	-2	N
EU18-W2-54	-246.7	0.3	-31.2	0.0	2.8	3	-3	N
EU18-W2-55	-246.5	0.4	-31.2	0.1	3.2	3	-4	N
EU18-W2-56	-246.4	0.4	-31.1	0.1	2.6	3	-5	N
EU18-W2-57	-244.5	0.4	-30.8	0.1	2.2	3	-6	N
EU18-W2-58	-245.4	0.5	-31.1	0.1	3.2	3	-7	N
EU18-W2-59	-245.8	0.5	-31.0	0.1	2.2	3	-8	N
EU18-W2-60	-245.8	0.4	-30.9	0.1	1.7	3	-9	N
EU18-W2-61	-244.6	0.2	-30.5	0.0	-0.7	1		Y
EU18-W2-62	-242.5	0.6	-30.7	0.1	3.0	1		Y

WEDGE 3:

Sample Name	δ2H (‰)	δ2H (‰) StDev	δ18O (‰)	δ 18O (‰) StDev	D-excess	Location: (Top - 1; Middle-2; Middle -3; Bottom-4)	Distance from centre (cm)	Permafrost (Y/N)
EU18-W3-1	-187.8	0.5	-23.7	0.1	1.8	2	-14	Y
EU18-W3-2	-192.2	0.5	-24.3	0.1	2.2	2	-13	Y
EU18-W3-3	-189.8	0.8	-24.1	0.1	3.2	2	-12	Y
EU18-W3-4	-189.0	0.8	-24.2	0.1	4.6	2	-11	Y
EU18-W3-5	-186.3	0.2	-23.5	0.1	1.5	2	-10	Y
EU18-W3-6	-185.3	0.3	-23.5	0.1	2.4	2	-9	Y
EU18-W3-7	-185.1	0.1	-23.4	0.1	1.9	2	-8	Y
EU18-W3-8	-184.7	0.6	-23.4	0.1	2.5	2	-7	Y
EU18-W3-9	-222.3	0.7	-28.3	0.2	4.0	2	-6	N
EU18-W3-10	-223.0	0.9	-28.2	0.1	2.9	2	-5	N
EU18-W3-11	-223.8	0.2	-28.4	0.0	3.1	2	-4	N
EU18-W3-12	-223.3	0.5	-28.2	0.1	2.5	2	-3	N
EU18-W3-13	-208.7	0.4	-26.1	0.1	0.0	2	-2	N
EU18-W3-14	-206.6	0.9	-26.0	0.1	1.5	2	-1	N
EU18-W3-15	-205.8	0.5	-25.9	0.1	1.7	2	0	N
EU18-W3-16	-208.2	0.7	-26.3	0.0	1.8	2	1	N
EU18-W3-17	-213.1	0.5	-26.9	0.1	2.0	2	2	N
EU18-W3-18	-218.3	0.7	-27.6	0.2	2.1	2	3	N
EU18-W3-19	-223.7	0.3	-28.2	0.1	2.0	2	4	N
EU18-W3-20	-227.2	0.3	-28.7	0.0	2.2	2	5	N
EU18-W3-21	-226.7	0.5	-28.7	0.1	3.3	2	6	N
EU18-W3-22	-224.1	0.4	-28.4	0.0	3.0	2	7	N
EU18-W3-23	-223.0	0.2	-28.3	0.1	3.4	2	8	N
EU18-W3-24	-222.6	0.3	-28.2	0.1	3.2	2	9	N
EU18-W3-25	-206.4	0.5	-25.8	0.1	0.3	2	10	N
EU18-W3-26	-209.1	0.1	-26.2	0.1	0.2	2	11	N
EU18-W3-27	-212.1	0.4	-26.7	0.1	1.2	2	12	N
EU18-W3-28	-211.5	0.3	-26.6	0.1	0.9	2	13	N
EU18-W3-29	-212.2	0.5	-26.6	0.1	0.9	2	14	N
EU18-W3-30	-186.4	0.5	-23.1	0.1	-1.2	2	15	Y
EU18-W3-31	-186.1	0.7	-23.1	0.1	-1.2	2	16	Y

Sample Name	δ2H (‰)	δ2H (‰) StDev	δ18O (‰)	δ 18O (‰) StDev	D-excess	Location: (Top - 1; Middle-2; Middle -3; Bottom-4)	Distance from centre (cm)	Permafrost (Y/N)
EU18-W3-32	-187.8	0.5	-23.3	0.1	-1.6	2	17	Y
EU18-W3-34	-189.5	0.5	-23.4	0.1	-2.7	2	18	Y
EU18-W3-39	-189.9	0.2	-23.2	0.1	-4.5	2	19	Y
EU18-W3-40	-185.3	0.1	-22.9	0.1	-2.1	3	-14	Y
EU18-W3-41	-186.0	0.3	-23.1	0.0	-1.0	3	-13	Y
EU18-W3-42	-186.0	0.3	-23.1	0.1	-1.4	3	-12	Y
EU18-W3-43	-189.3	1.3	-23.4	0.0	-2.1	3	-11	Y
EU18-W3-44	-194.1	0.2	-24.3	0.1	-0.1	3	-10	Y
EU18-W3-45	-212.6	0.4	-26.8	0.0	2.1	3	-9	N
EU18-W3-46	-214.5	0.6	-26.9	0.1	0.4	3	-8	N
EU18-W3-47	-222.6	0.2	-28.3	0.1	3.5	3	-7	N
EU18-W3-48	-223.9	0.3	-28.5	0.1	4.0	3	-6	N
EU18-W3-49	-224.5	0.3	-28.4	0.0	2.7	3	-5	N
EU18-W3-50	-224.7	0.5	-28.4	0.1	2.2	3	-4	N
EU18-W3-51	-225.8	0.2	-28.9	0.2	5.0	3	-3	N
EU18-W3-52	-225.1	0.7	-28.8	0.2	5.6	3	-2	N
EU18-W3-53	-227.1	0.5	-29.3	0.1	7.7	3	-1	N
EU18-W3-54	-229.9	0.8	-29.1	0.1	2.9	3	0	N
EU18-W3-55	-230.5	0.5	-29.2	0.1	3.5	3	1	N
EU18-W3-56	-230.2	0.4	-29.3	0.1	4.4	3	2	N
EU18-W3-57	-229.2	0.3	-29.4	0.0	5.8	3	3	N
EU18-W3-58	-228.7	0.4	-29.4	0.1	6.4	3	4	N
EU18-W3-59	-227.1	0.3	-28.8	0.1	3.1	3	5	N
EU18-W3-60	-227.1	0.3	-28.8	0.1	3.1	3	6	N
EU18-W3-61	-227.1	0.2	-28.8	0.0	3.4	3	7	N
EU18-W3-62	-223.7	0.2	-28.3	0.1	3.0	3	8	N
EU18-W3-63	-217.8	0.7	-27.6	0.1	3.4	3	9	N
EU18-W3-64	-212.7	0.3	-26.9	0.1	2.8	3	10	Y
EU18-W3-65	-204.0	0.5	-25.8	0.1	2.3	3	11	Y
EU18-W3-66	-200.2	0.8	-25.2	0.1	1.1	3	12	Y
EU18-W3-67	-195.3	0.2	-24.5	0.1	0.9	3	13	Y
EU18-W3-68	-190.7	0.2	-24.0	0.1	1.0	3	14	Y
EU18-W3-69	-185.4	0.5	-23.3	0.1	1.0	3	15	Y

Sample Name	δ2H (‰)	δ2H (‰) StDev	δ18O (‰)	δ 18O (‰) StDev	D-excess	Location: (Top - 1; Middle-2; Middle -3; Bottom-4)	Distance from centre (cm)	Permafrost (Y/N)
EU18-W3-70	-180.3	0.5	-22.7	0.1	1.3	3	16	Y
EU18-W3-71	-177.5	0.3	-22.3	0.1	1.1	3	17	Y
EU18-W3-72	-178.1	0.2	-22.3	0.1	0.2	3	18	Y
EU18-W3-73	-176.5	0.8	-21.7	0.1	-3.2	3	19	Y
EU18-W3-74	-180.6	0.1	-22.7	0.0	0.7	3	20	Y
EU18-W3-75	-179.9	0.3	-22.2	0.1	-2.4	3	21	Y
EU18-W3-76	-175.8	0.4	-21.5	0.0	-3.9	1	-32	Y
EU18-W3-77	-183.0	0.2	-23.0	0.1	0.9	1	-31	Y
EU18-W3-78	-184.5	0.2	-23.3	0.1	1.5	1	-30	Y
EU18-W3-79	-184.6	0.2	-23.3	0.1	1.9	1	-29	Y
EU18-W3-80	-183.9	0.3	-23.2	0.1	2.0	1	-28	Y
EU18-W3-81	-184.0	0.2	-23.2	0.0	1.6	1	-27	Y
EU18-W3-82	-185.4	0.3	-23.4	0.1	1.6	1	-26	Y
EU18-W3-83	-185.6	0.4	-23.5	0.0	2.5	1	-25	Y
EU18-W3-84	-185.9	0.2	-23.4	0.1	1.6	1	-24	Y
EU18-W3-85	-185.9	0.5	-23.3	0.1	0.8	1	-23	Y
EU18-W3-86	-187.8	0.5	-23.7	0.1	1.7	1	-22	Y
EU18-W3-87	-188.5	0.2	-23.7	0.1	1.4	1	-21	Y
EU18-W3-88	-187.7	0.4	-23.6	0.1	1.4	1	-20	Y
EU18-W3-89	-188.3	0.2	-23.6	0.1	0.6	1	-19	Y
EU18-W3-90	-188.3	0.2	-23.8	0.1	1.8	1	-18	Y
EU18-W3-91	-187.7	0.2	-23.6	0.1	1.5	1	-17	Y
EU18-W3-92	-187.4	0.6	-23.4	0.1	0.2	1	-16	Y
EU18-W3-93	-191.8	0.4	-24.3	0.1	2.2	1	-15	Y
EU18-W3-94	-196.5	0.4	-24.5	0.0	-0.2	1	-14	Y
EU18-W3-95	-219.9	0.4	-27.8	0.1	2.2	1	-13	N
EU18-W3-96	-215.9	0.3	-27.3	0.1	2.2	1	-12	N
EU18-W3-97	-221.4	0.5	-28.0	0.1	2.6	1	-11	N
EU18-W3-98	-224.8	0.3	-28.7	0.1	4.4	1	-10	N
EU18-W3-99	-223.0	0.6	-28.3	0.1	3.5	1	-9	N
EU18-W3-100	-217.1	0.3	-27.6	0.1	3.5	1	-8	N
EU18-W3-101	-226.0	0.5	-28.7	0.1	3.3	1	-7	N
EU18-W3-102	-226.5	0.2	-28.8	0.1	3.6	1	-6	N

Sample Name	δ2H (‰)	δ2H (‰) StDev	δ18O (‰)	δ 18O (‰) StDev	D-excess	Location: (Top - 1; Middle-2; Middle -3; Bottom-4)	Distance from centre (cm)	Permafrost (Y/N)
EU18-W3-103	-226.0	0.4	-28.5	0.1	2.3	1	-5	N
EU18-W3-104	-228.3	0.4	-29.0	0.1	4.0	1	-4	N
EU18-W3-105	-228.3	0.3	-29.0	0.1	3.5	1	-3	N
EU18-W3-106	-186.2	0.2	-23.5	0.0	2.1	1	-2	N
EU18-W3-107	-187.3	0.6	-23.7	0.1	2.1	1	-1	N
EU18-W3-108	-193.1	0.4	-24.5	0.1	2.5	1	0	N
EU18-W3-109	-201.8	0.5	-25.5	0.1	2.6	1	1	N
EU18-W3-110	-210.5	0.6	-26.6	0.1	2.5	1	2	N
EU18-W3-111	-226.3	0.6	-28.7	0.1	2.9	1	3	N
EU18-W3-112	-229.2	0.5	-29.0	0.1	3.2	1	4	N
EU18-W3-113	-230.3	0.3	-29.2	0.1	2.9	1	5	N
EU18-W3-114	-231.6	0.1	-29.3	0.1	2.7	1	6	N
EU18-W3-115	-232.5	0.3	-29.5	0.1	3.2	1	7	N
EU18-W3-116	-224.8	0.3	-28.5	0.0	3.4	1	8	N
EU18-W3-117	-225.6	0.1	-28.5	0.1	2.7	1	9	N
EU18-W3-118	-226.6	0.4	-28.7	0.1	2.8	1	10	N
EU18-W3-119	-224.9	0.4	-28.5	0.1	3.1	1	11	N
EU18-W3-120	-225.1	0.2	-28.6	0.0	4.1	1	12	N
EU18-W3-121	-222.2	0.3	-28.2	0.1	3.8	1	13	N
EU18-W3-122	-219.5	0.2	-27.9	0.1	3.4	1	14	N
EU18-W3-123	-224.1	0.5	-28.5	0.1	4.1	4	-10	N
EU18-W3-124	-225.6	0.3	-28.6	0.1	3.5	4	-9	N
EU18-W3-125	-226.9	0.6	-28.8	0.1	3.8	4	-8	N
EU18-W3-126	-222.7	0.4	-28.3	0.0	3.8	4	-7	N
EU18-W3-127	-227.9	0.1	-28.7	0.0	1.7	4	-6	N
EU18-W3-128	-219.4	0.5	-27.5	0.1	0.3	4	-5	N
EU18-W3-129	-229.5	0.6	-29.2	0.1	3.7	4	-4	N
EU18-W3-130	-229.7	0.4	-29.1	0.1	3.0	4	-3	N
EU18-W3-131	-192.8	0.3	-24.3	0.1	1.5	4	-2	Y
EU18-W3-132	-193.8	0.6	-24.3	0.1	1.0	4	-1	Y

WEDGE 4:

Sample Name	δ2H (‰)	δ2H (‰) StDev	δ18O (‰)	δ 18O (‰) StDev	D-excess	Location: (Top - 1; Middle-2; Middle -3; Bottom-4)	Distance from centre (cm)	Permafrost (Y/N)
EU18-W4-1	-238.8	0.4	-30.1	0.1	2.0	1	-7	N
EU18-W4-2	-241.7	0.3	-30.7	0.1	3.8	1	-6	N
EU18-W4-3	-244.3	0.2	-31.0	0.1	3.8	1	-5	N
EU18-W4-4	-242.9	0.3	-31.0	0.1	5.0	1	-4	N
EU18-W4-5	-244.5	0.0	-30.9	0.1	2.4	1	-3	N
EU18-W4-6	-242.1	0.6	-30.8	0.1	4.0	1	-2	N
EU18-W4-7	-240.4	0.0	-30.6	0.2	4.4	1	-1	N
EU18-W4-8	-240.4	0.4	-30.6	0.1	4.5	1	0	N
EU18-W4-9	-245.0	0.3	-31.0	0.1	3.2	1	1	N
EU18-W4-10	-248.0	0.2	-31.5	0.1	4.0	1	2	N
EU18-W4-11	-245.6	0.4	-31.4	0.2	5.4	1	3	N
EU18-W4-12	-227.0	0.1	-28.5	0.2	1.4	1	4	N
EU18-W4-13	-231.4	0.3	-29.3	0.2	3.2	1	5	N
EU18-W4-14	-235.8	0.2	-30.0	0.1	3.9	1	6	N
EU18-W4-15	-237.6	0.3	-30.2	0.1	4.3	1	7	N
EU18-W4-16	-238.4	0.3	-30.3	0.1	4.2	1	8	N
EU18-W4-17	-233.9	0.5	-29.5	0.1	2.1	1	9	N
EU18-W4-18	-225.7	0.5	-28.4	0.2	1.6	1	10	N
EU18-W4-19	-219.4	0.3	-27.4	0.1	-0.5	1	11	Y
EU18-W4-20	-222.0	0.3	-27.7	0.2	-0.2	1	12	Y
EU18-W4-21	-216.7	0.1	-27.3	0.1	1.6	1	13	Y
EU18-W4-22	-218.7	0.4	-27.4	0.2	0.4	1	14	Y
EU18-W4-23	-219.3	0.5	-27.4	0.2	0.3	1	15	Y
EU18-W4-24	-219.0	0.4	-27.2	0.0	-1.2	1	16	Y
EU18-W4-25	-220.8	0.3	-27.8	0.1	1.4	1	17	Y
EU18-W4-26	-221.4	1.2	-27.8	0.1	0.7	1	18	Y
EU18-W4-27	-222.0	0.2	-27.9	0.2	1.3	1	19	Y
EU18-W4-28	-220.8	0.3	-27.4	0.1	-1.6	1	20	Y
EU18-W4-29	-239.8	0.2	-30.4	0.1	3.1	2	-9	N
EU18-W4-30	-242.0	0.5	-30.6	0.2	2.6	2	-8	N

Sample Name	δ2H (‰)	δ2H (‰) StDev	δ18O (‰)	δ 18O (‰) StDev	D-excess	Location: (Top - 1; Middle-2; Middle -3; Bottom-4)	Distance from centre (cm)	Permafrost (Y/N)
EU18-W4-31	-241.8	0.3	-30.9	0.1	5.3	2	-7	N
EU18-W4-32	-239.6	0.2	-30.4	0.1	3.4	2	-6	N
EU18-W4-33	-242.2	0.2	-30.7	0.2	3.2	2	-5	N
EU18-W4-34	-243.5	0.3	-30.7	0.1	2.3	2	-4	N
EU18-W4-35	-242.7	0.2	-30.8	0.2	3.4	2	-3	N
EU18-W4-36	-237.5	0.4	-29.6	0.1	-0.7	2	-2	N
EU18-W4-37	-241.9	0.3	-30.7	0.1	4.0	2	-1	N
EU18-W4-38	-244.6	0.2	-31.0	0.1	3.6	2	0	N
EU18-W4-39	-245.3	0.1	-31.2	0.1	4.2	2	1	N
EU18-W4-40	-233.1	0.2	-28.8	0.1	-2.7	2	2	N
EU18-W4-41	-236.5	0.5	-29.9	0.1	2.3	2	3	N
EU18-W4-42	-238.5	0.6	-30.4	0.1	4.6	2	4	N
EU18-W4-43	-237.9	0.1	-30.0	0.1	2.5	2	5	N
EU18-W4-44	-233.2	0.5	-29.4	0.1	1.9	2	6	N
EU18-W4-45	-233.5	0.2	-29.4	0.1	1.4	2	7	N
EU18-W4-46	-216.5	0.2	-26.1	0.1	-7.7	2	8	Y
EU18-W4-47	-214.8	0.1	-25.9	0.0	-7.3	2	9	Y
EU18-W4-48	-234.4	0.8	-29.5	0.1	1.7	2	10	N
EU18-W4-49	-236.1	0.3	-30.1	0.1	4.9	2	11	N
EU18-W4-50	-232.4	0.1	-29.4	0.2	2.5	2	12	N
EU18-W4-51	-246.3	0.4	-31.4	0.0	4.8	3	-10	N
EU18-W4-52	-232.0	0.3	-29.4	0.2	2.9	3	-9	N
EU18-W4-53	-254.0	0.6	-32.3	0.1	4.6	3	-8	N
EU18-W4-54	-252.2	0.3	-32.0	0.1	4.1	3	-7	N
EU18-W4-55	-249.9	0.4	-31.5	0.1	1.7	3	-6	N
EU18-W4-56	-250.8	0.2	-31.5	0.2	1.2	3	-5	N
EU18-W4-57	-243.7	0.5	-30.8	0.1	2.8	3	-4	N
EU18-W4-58	-250.3	0.3	-31.7	0.1	3.3	3	-3	N
EU18-W4-59	-251.2	0.5	-31.8	0.1	3.5	3	-2	N
EU18-W4-60	-249.5	0.5	-31.4	0.1	1.5	3	-1	N
EU18-W4-61	-249.2	0.1	-31.5	0.1	2.8	3	0	N
EU18-W4-62	-247.4	0.7	-31.4	0.1	3.8	3	1	N
EU18-W4-63	-247.6	0.3	-31.5	0.0	4.1	3	2	N

Sample Name	δ2H (‰)	δ2H (‰) StDev	δ18O (‰)	δ 18O (‰) StDev	D-excess	Location: (Top - 1; Middle-2; Middle -3; Bottom-4)	Distance from centre (cm)	Permafrost (Y/N)
EU18-W4-64	-246.2	0.2	-31.2	0.1	3.6	3	3	N
EU18-W4-65	-244.7	0.6	-31.1	0.1	4.4	3	4	N
EU18-W4-66	-249.5	0.1	-31.6	0.1	3.2	3	5	N
EU18-W4-67	-247.5	0.6	-31.5	0.1	4.3	3	6	N
EU18-W4-68	-243.1	0.3	-30.8	0.0	3.3	3	7	N
EU18-W4-69	-232.9	0.6	-29.5	0.1	2.9	3	8	N
EU18-W4-70	-238.5	0.2	-30.2	0.0	3.2	3	9	N
EU18-W4-71	-240.3	0.5	-30.5	0.0	3.6	3	10	N
EU18-W4-73	-215.8	1.3	-24.5	0.1	-20.0	4	-7	Y
EU18-W4-74	-225.5	0.4	-27.8	0.2	-3.0	4	-6	Y
EU18-W4-75	-245.7	0.4	-31.1	0.1	2.9	4	-5	N
EU18-W4-76	-248.0	0.3	-31.5	0.1	4.0	4	-4	N
EU18-W4-77	-248.5	0.3	-31.7	0.2	5.1	4	-3	N
EU18-W4-78	-249.1	0.5	-31.8	0.2	5.4	4	-2	N
EU18-W4-79	-243.8	0.3	-31.1	0.1	4.6	4	-1	N
EU18-W4-80	-246.7	0.6	-31.2	0.2	2.9	4	0	N
EU18-W4-81	-242.6	0.6	-30.8	0.2	3.4	4	1	N
EU18-W4-82	-244.1	0.3	-31.0	0.1	3.9	4	2	N
EU18-W4-83	-246.5	0.3	-31.2	0.2	3.3	4	3	N
EU18-W4-84	-248.3	0.5	-31.6	0.1	4.3	4	4	N
EU18-W4-85	-248.9	0.3	-31.6	0.2	3.6	4	5	N
EU18-W4-86	-226.6	0.3	-28.3	0.2	-0.2	4	6	Y
EU18-W4-87	-228.2	0.3	-28.7	0.1	1.4	4	7	Y
EU18-W4-88	-230.2	0.3	-29.0	0.1	1.5	4	8	Y
EU18-W4-89	-229.9	0.5	-29.1	0.1	2.6	4	9	Y

Appendix F – Vertical Ice Wedge Results

Location		Slump	Wedge #	Sample #	Position	Distance from centre (m)	δ 2H (‰)	δ 2H(‰) StDev	δ 18O(‰)	δ 18O (‰) StDev	D-excess
EU19		Dump	W1	1	Centre	0	-242.45	0.37	-30.61	0.07	2.40
				2	Right	1.6	-262.60	0.40	-33.64	0.07	6.48
				3	Left	-1.25	-229.60	0.90	-29.15	0.13	3.57
				4	Right of Centre	0.7	-253.54	0.54	-32.45	0.11	6.09
				5	Left of Centre	-0.65	-248.12	0.08	-31.37	0.18	2.84
		Blacktop	W2	1	Left	-0.39	-221.69	0.20	-27.62	0.11	-0.76
				2	Centre	0	-233.93	0.48	-29.90	0.12	5.29
		Blacktop	W2	3	Right	0.45	-230.96	0.60	-29.22	0.09	2.81
		Nunavut	W3	1	Left	-0.33	-228.43	0.15	-29.31	0.05	6.04
				2	Centre	0	-249.11	0.36	-32.09	0.05	7.64
				3	Right	0.3	-246.15	0.72	-31.68	0.17	7.26
			W4	1	Centre	0	-243.30	0.00	-30.54	0.00	1.03
				2	Left	-2.04	-241.73	0.62	-30.33	0.07	0.89
				3	Right	1.68	-253.24	0.63	-32.46	0.09	6.40
		Nunavut	W5	1	Right	0.15	-236.42	0.33	-30.36	0.10	6.46
				2	Left	-0.15	-228.55	0.21	-28.32	0.12	-2.02
				3	Centre	0	-239.53	0.62	-30.60	0.11	5.27
MF1		Mokka Fjord	W1	1	Centre	0	-246.83	0.15	-31.71	0.05	6.83
				2	Right	1.55	-241.25	0.03	-30.79	0.04	5.11
		Mokka Fjord	W1	3	Left	-1	-227.36	0.68	-28.90	0.04	3.83
			W2	1	Centre	0	-241.11	0.77	-30.60	0.12	3.71
				2	Right	0.67	-253.65	0.28	-31.98	0.07	2.20
				3	Left	-1.53	-242.81	0.40	-30.89	0.05	4.31
			W3	1	Right	1.5	-234.59	0.34	-29.66	0.07	2.71
				2	Centre	0	-246.77	0.07	-31.24	0.21	3.14
				3	Left	-1.5	-232.47	0.60	-29.51	0.14	3.59

			Dissolved Organic Carbon		Radiocarbon							
Wedge #	**Sample #**	**Lab-ID**	**[DOC] (ppm)**	**δ 13C DOC (‰)**	**14C yr BP**	**±**	**F14C**	**±**	**max Cal BP**	**min Cal BP**	**percent certainty**	**median Cal BP**
W1	1	UOC-11064	0.96	-24.49	22146	163	0.0635	0.0013	26877	25997	95.4	26370
	2	UOC-11065	1.26	-25.29	13636	69	0.1832	0.0016	16722	16198	95.4	16437
	3	UOC-11066	2.92	-26.51	24872	367	0.0452	0.0021	29834	28096	95.4	28954
	4	UOC-11067	1.48	-24.85	14480	109	0.1649	0.0022	17944	17357	95.4	17651
	5	UOC-11068	0.88	-27.23	10308	75	0.2772	0.0026	12412	11816	95.4	12125
W2	1	UOC-12524	4.67	-24.44	9883	45	0.2922	0.0017	11396	11208	95.4	11278
	2	UOC-12525	3.13	-24.64	6320	36	0.4553	0.002	7317	7168	95.4	7250
	3	UOC-12526	8.68	-24.54	12127	61	0.221	0.0017	14154	13785	95.4	13994
W3	1		3.60	-24.80								
	2	UOC-11070	1.88	-25.43	6038	41	0.4716	0.0024	6996	6782	95.1	6885
	3	UOC-12527	2.71	-24.95	7088	39	0.4138	0.002	7982	7840	95.4	7919
W4	1		5.90	-24.90								
	2	UOC-12528	2.30	-25.68	7288	39	0.4036	0.002	8176	8017	95.4	8100
	3	UOC-11071	3.94	-24.77	6251	42	0.4593	0.0024	7266	7150	72.7	7190
W5	1	UOC-12529	2.06	-25.71	6614	36	0.439	0.002	7568	7440	95.4	7506
	2	UOC-12530	5.61	-24.38	7739	35	0.3816	0.0016	8590	8434	95.4	8514
	3	UOC-11072	4.59	-24.86	7222	37	0.407	0.0019	8074	7965	69.4	8028
W1	1	UOC-12531	2.56	-26.06	2503	33	0.7323	0.003	2739	2485	94.6	2587
	2	UOC-11073	2.78	-26.65	3438	35	0.6518	0.0028	3828	3609	95.4	3694
	3	UOC-12532	48.66	-24.86	6061	48	0.4703	0.0028	7026	6780	90.7	6917
W2	1	UOC-12533	3.25	-25.36	4347	44	0.5821	0.0032	4987	4841	85.1	4921
	2		5.75	-26.36	CONTAMINATED							
	3		2.36	-25.87	CONTAMINATED							
W3	1	UOC-12534	3.20	-26.20	5941	36	0.4773	0.0022	6860	6672	93.8	6765
	2		3.14	-26.36	CONTAMINATED							
	3	UOC-12535	3.86	-25.66	7077	58	0.4144	0.003	8009	7789	95.4	7900

		Soluble Cations (mg/L)						Soluble Anions (mg/L)		
Wedge #	**Sample #**	**Ca**	**Fe**	**K**	**Mg**	**Na**	**Sr**	**Cl**	**SO4**	**NO3**
W1	1	22.15	0.04	5.44	11.06	28.25	0.10	14.71	77.19	19.55
	2	16.74	0.09	4.08	7.05	43.23	0.09	51.30	46.00	0.51
	3	13.05	0.58	5.59	7.28	78.69	0.12	70.61	54.51	0.26
	4	19.26	0.11	5.41	8.55	58.90	0.11	56.79	83.45	0.28
	5	16.18	0.06	1.90	4.61	66.88	0.10	29.91	126.99	0.19
W2	1	31.88	0.02	6.48	10.11	47.79	0.14	104.14	59.45	0.21
	2	19.46	0.07	2.14	8.16	15.53	0.09	41.84	27.09	0.16
	3	28.47	0.09	19.66	10.00	307.30	0.14	426.56	63.22	0.51
W3	1	25.66	0.16	8.95	14.04	53.10	0.15	55.30	82.86	0.43
	2	15.21	0.01	1.74	2.88	13.89	0.07	13.77	32.32	0.03
	3	14.94	0.01	3.38	3.91	15.04	0.06	14.74	39.21	0.09
W4	1	3.99	1.11	2.94	2.55	12.00	0.02	8.61	8.46	0.09
	2	14.17	0.07	2.39	3.47	9.78	0.06	12.46	29.18	0.12
	3	9.01	0.21	4.38	4.46	20.41	0.05	19.51	29.24	0.03
W5	1	9.127	0.0473	1.968	2.729	16.77	0.0515	19.39	26.47	0.10
	2	6.502	0.1231	3.288	3.030	17.59	0.0334	11.57	17.14	0.45
	3	8.71	0.70	3.92	5.45	38.82	0.06	33.04	44.46	0.58
W1	1	10.55	0.02	1.28	2.28	11.89	0.05	15.06	25.23	0.10
	2	16.38	0.02	1.20	1.93	9.49	0.09	12.49	29.91	0.07
	3	53.34	3.21	8.75	36.63	100.01	0.42	259.89	35.98	0.01
W2	1	40.20	0.04	5.14	21.71	87.76	0.20	82.04	232.68	-0.02
	2	12.30	0.06	2.18	5.60	21.28	0.07	37.53	29.49	0.15
	3	10.86	0.02	2.34	5.02	16.12	0.06	31.68	26.64	0.05
W3	1	5.41	0.04	1.35	2.60	10.95	0.03	15.99	21.05	0.10
	2	5.24	0.03	1.22	2.03	9.59	0.03	14.57	13.70	0.11
	3	10.53	0.25	2.52	5.01	25.24	0.08	31.21	38.76	0.05